UNIVERSITY OF THESSALY

Muscle and tendon tissues: constitutive modeling, numerical implementation and applications

by

Leonidas A. Spyrou

Submitted to the Department of Mechanical Engineering
in Partial Fulfillment of the Requirements for the Degree of

DOCTOR OF PHILOSOPHY

September 2009

To my family and beloved friends

Thesis Committee

(in alphabetical order)

Professor Nikolaos ARAVAS (adviser)

Department of Mechanical Engineering, University of Thessaly

Professor Antonios GIANNAKOPOULOS (examiner)

Department of Civil Engineering, University of Thessaly

Professor Gregory HAIDEMENOPOULOS (examiner)

Department of Mechanical Engineering, University of Thessaly

Professor Elias HOUSTIS (examiner)

Department of Computer and Communications Engineering
University of Thessaly

Professor Eleftherios KELLIS (examiner)

Department of Physical Education and Sport Sciences
Aristotle University of Thessaloniki

Professor Konstantinos MALIZOS (examiner)

Orthopaedic Department, Medical School, University of Thessaly

Professor Christopher PROVATIDIS (examiner)

School of Mechanical Engineering, National Technical University of Athens

Acknowledgments

The research reported in the thesis was carried out at the Laboratory of Mechanics & Strength of Materials under the doctoral program of the Department of Mechanical Engineering of the University of Thessaly (UTH). The thesis work was funded by fellowships from the Department of Mechanical Engineering via the Research Committee of University of Thessaly and the "Mechatronics Institute" of the "Center for Research and Development, Thessaly" (CE.RE.TE.TH.).

I would like to express my gratitude to my thesis adviser and mentor Professor Nikos Aravas for his guidance and support throughout my studies in the field of computational mechanics. I would like to thank him for the tremendous amount of knowledge that he transmitted to me all these years, as well as for his immense influence in my way of thinking.

I would also like to thank Professor Konstantinos Malizos, member of my Thesis committee, who, together with Professor Aravas, introduced me to the extraordinary field of biomechanics and gave me the incentive to follow this extremely interesting field of research.

I would like to express my gratitude to Professor Eleftherios Kellis for his special interest in my work and for accepting to participate in my thesis committee. I gratefully thank Professor Antonios Giannakopoulos, Professor Gregory Haidemenopoulos, Professor Elias Houstis, and Professor Christopher Provatidis for accepting to be members of my thesis committee. I feel extremely honored to have had a committee of such a high scientific caliber.

I would like to thank also Professor Robert McMeeking of the University of California Santa Barbara for helpful discussions and material on the subject of the thesis.

My special thanks go to Dimitra Kaptsianou, PhD Candidate of UTH, who volunteered to participate in the procedure for the acquisition of data needed to develop my lower-extremity model, as well as to Dr. Evagelos Kaffes, Director of a medical imaging center in Volos, for his unconditional help and services to the medical imaging procedure.

Also, I would like to express my deep gratitude to my close friends with whom I spent great time while not studying and who are responsible for making every moment of my life unique.

I am greatly indebted to my parents Athanasios and Ioanna who offered me unsparingly

all the appropriate supplies to live in comfort over all these years, and my sister Athena for her unconditional support, encouragement, and guidance.

Last but not least I would like to express my deepest gratitude to Aimilia for her extraordinary patience, understanding, support, and optimism.

ABSTRACT

Muscle and tendon tissues: Constitutive modeling, numerical implementation and applications

Leonidas A. Spyrou
Adviser: Professor Nikolaos Aravas

This work is concerned with the biological functioning and mechanical behavior of muscles and tendons. From the Mechanics viewpoint, muscles and tendons are "composite" materials that consist of fibers, connective tissues, and biofluids surrounding the fibers. The idea of considering these materials as "continuous media" is used and a "homogenization" process that accounts for the presence of the fibers and the other material "phases" is developed.

Thus, the main objective of this work is to propose a general and realistic constitutive model for the mechanical behavior of skeletal muscle and tendon when the materials are subjected to finite strains. The model accounts for all the essential information about the microstructure of the materials. Also, it is constructed in such a way that different material properties of different muscles can be altered easily when the behavior of a whole group of muscles is to be studied in the same time.

Furthermore, a methodology to handle numerically the resulting non-linear and anisotropic constitutive equations in the context of finite element method is developed. The constitutive model is, then, implemented in a general-purpose finite element program.

Finally, the developed model is used to study the behavior of several muscle-tendon complex cases. Firstly, the extension of a squid tentacle during the strike to catch prey is simulated in order to validate the proposed model with previous experimental and computational results. Next, the behavior of simplified parallel fibred and pennated muscles is studied. Also, the human semitendinosus muscle is simulated. The constitutive model is further applied to the muscles and tendons of the human leg and the plantar flexion of the ankle is achieved.

Contents

List of Tables

List of Figures

Chapter 1

Introduction and Literature review

The undying attempts to understand nature and biological functioning date back to ancient cultures. Over the centuries the exploration of the mechanics of living systems continued to attract people with intellectual pursuits followed though by the limitations of each era. In our days *biomechanics* is an increasingly developed science, mostly due to technological growth and the well-developed knowledge in many scientific disciplines such as physics, chemistry, mathematics, physiology and anatomy.

The development of biomechanics has improved our understanding of many aspects in different fields. In general, biomechanical research studies the:

- Movement of different body segments and factors that influence movement such as body alignment, weight distribution, equipment.
- Deformation of biological structures and factors that influence their deformity.
- Biological effects of locally acting forces on living tissue; effects such as growth and development or overload and injuries.
- Biological factors that influence the biological materials' behavior and the overall performance; factors such as age, gender, exercise, immobility, nutrition and illness.

A wide variety of professions including orthopaedic surgery, rehabilitation engineering, therapy, kinesiology, prosthetics, orthotics, automotive safety, sports equipment designers, athletic coaches, can benefit from the biomechanical research to the improvement of human's performance and the reduction or treatment of injuries.

Biomechanics is most useful in improving performance in sports or activities where technique prevails to physical structure or physiological capacity. Although technique is always relevant to human movement, in some activities the psychological, anatomical or physiological factors are more strongly related to success. However, the improvement in the design of sports equipment not only could affect the athlete's technique but also enhance the whole human performance. Biomechanical studies, also, confirm potential injury mechanisms and help the prevention of injuries by providing information on the mechanical properties of

tissues, mechanical loadings during movement and preventative or rehabilitative therapies. Research in biomechanics to prevent injuries started from sports and recently is applied in medicine (preventive medicine) and automotive safety field where human models are used for computer crash simulations. Despite the efforts to prevent injuries, many injury cases appear day by day and are confronted with great difficulties. Biomechanical research in this field is also very important as it helps to improve the design of orthotics, prosthetics or other medical devices, to gain better understanding of the loadings on the body tissues, to improve the surgery procedures and as a result to minimize the patient's suffering and improve the quality of life.

Research activities in biomechanics can be divided into experimental studies and model analysis. Experimental techniques are fundamental to the study of soft tissues. This kind of studies are done to determine the mechanical properties of biological materials, including the bone, cartilage, muscle, tendon, ligament and other soft tissues of the body structure. All the studies presenting experimental results are based on tissues of animal subjects or human cadavers. The experimental procedure is highly demanding and may be considered as a challenge as it is sensitive to many parameters and it is necessary to reproduce the *in vivo* conditions of the tissue in the laboratory. Model analysis that is based on experimental findings can be used to predict the effect of environmental and operational factors without resorting to laboratory experiments. *Computational modeling* plays a significant role in biomechanics since, in most cases, it is prohibitive to apply experimentally different case studies on human beings. Also, the various biological materials exist and function together in the joints, which allow relative movement between segments, the transfer of forces from one segment to the next and facilitate biochemical and physiological interaction between the neighboring biological materials. It is very difficult to achieve accurate findings by experimental studies for the biological materials' behavior and the complex loadings under these circumstances. Computer models could be used in an efficient way so as to overcome the barriers of numerous experiments. Of course, computational modeling of biological structures is not an easy task. It demands interdisciplinary knowledge of anatomy, physiology, mechanics and materials. It is worth mentioning that all the biomechanical models presented in the literature are based on several assumptions and present several limitations. The goal of the research in scientific fields by using computational techniques is to develop realistic models with limited assumptions. In order to achieve this goal in the field of *computational biomechanics*, a model of a biological system should include at least:

- Accurate representation of the geometry
- Realistic material properties of the biological materials
- Realistic internal or external loading conditions

1.1 Background and related work

1.1.1 Muscle modeling

The anatomical components of the human body can be divided into **active** and **passive** structures. **Active structures produce force whereas passive structures do not**. The only active structure in the human body is muscle and its capability of active contraction makes it distinct from other soft biological tissues. Because of its contractile properties, muscle is less easily associated with strictly mechanical properties than are bones or ligaments, for which force-elongation or stress-strain relations can be well-defined. So, dealing with the mechanics of muscle, the physiological and biochemical properties must always be kept in mind.

It is believed that the development of realistic constitutive models for the mechanical behavior of the muscle tissue can *enhance the understanding* of the complex muscle function. Additionally, it is the basis for realistic simulation of the human musculoskeletal system. It is well-proved that the presence of active muscle contraction to numerical models of biological structures provides a better insight to the whole structure loadings during movement and more accurate predictions of their behavior.

There are three ways one could use to model the mechanical behavior of a muscle:

- the cross-bridge model (A. F. Huxley, 1957),
- the Hill-type three-component model (Hill, 1938),
- the continuum model.

The cross-bridge model is based on the cross-bridge theory formulated by A. F. Huxley (1957). In Chapter 2 and section 2.1.1 the cross-bridge theory is presented in detail. Briefly, the theory states that the points where the force is generated are the cross-bridges which are placed on the myosin filament of a sarcomere. A sarcomere is the basic unit of a muscle's cross-striated myofibril and myofibril is found in skeletal muscle's lowest structural level. The cross-bridge model combines the biochemical and physiological characteristics of the muscle. It attempts to determine muscle force based on rates of attachment and detachment of muscle cross-bridges.

Although the cross-bridge model is an excellent predictor of steady-state muscle force and energetics, it has several limitations that should be pointed out. Structural nonuniformities on all levels of the muscle (sarcomere, fiber, fiber bundles) are not accounted for. Also, the cross-bridge is assumed to behave in a perfectly linear elastic way. The experimentally observed decrease in energy consumption for eccentric compared to the corresponding concentric contractions can not be described and the history-dependent features of muscular

force production can not be modeled. In addition, it is generally computationally prohibitive to model a whole muscle in this manner.

Another way to model the mechanics of muscle contraction is to use the Hill-type three-component model (Fig. 1.1). Hill model describes a muscle as an active contractile component with series and parallel passive elastic elements. To be more specific, there are:

- two elements arranged in series: one elastic element (C) to account for the muscle elasticity in isometric conditions, and one contractile element (B), which is freely extensible at rest, but capable of shortening when activated.
- one elastic element (A) placed in parallel with the two others to account for elasticity of the muscle at rest. A variation of the model could take into account viscous effects and consider (A) as a viscous element instead.

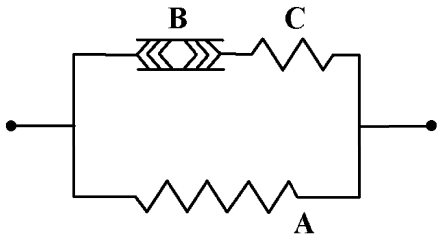

Figure 1.1: Hill-type three component model; (A). parallel elastic element (B). contractile element (C). series elastic element

While it has been recognized that the parallel element stands for the action of the intramuscular connective tissues surrounding the fibers, the series elastic element has mainly been attributed to the intrinsic elasticity of the cross-bridges.

Hill's model has been used extensively in the literature. It is attractive because of its computational simplicity and close relation to commonly measured experimental variables. It represents the global mechanical behavior of skeletal muscles in one dimension (the longitudinal direction). However, the Hill model has certain limitations likewise the cross-bridge model. The muscle is simply represented as a zero-mass line connecting two nodes along the line-of-action of the muscle. Its main weakness is its one dimensional formulation where the muscle mass, the geometrical characteristics of the muscle and the change in shape during muscle activation are not accounted for. Also, microstructure characteristics such as muscle fibers and their directions to form the muscle architecture can not be included in a Hill's model. From a strict computational modeling perspective the representation of different muscle-lines by springs and dashpots in a finite element model cause unrealistically high stress concentrations at the bone insertion points which may cause unrealistic fractures.

The third way to simulate the muscular contraction is to use a continuum three dimensional constitutive model. Almost all biological soft tissues are anisotropic, viscoelastic,

inhomogeneous, nearly incompressible and undergo large deformations *in vivo*, both under normal physiological conditions and during injury. Many of these tissues, including skeletal muscles, are reinforced by fibers, usually consisting of collagen and/or elastin. The consideration of muscle as a continuum is also a phenomenological model, like the Hill's model, but at a different architectural level. Attempts to develop this kind of models are made in the few past years, mostly because of their three dimensional formulation, the opportunity to account for microstructure characteristics of muscle, such as the muscle fibers and their orientation, and the ability of their implementation in the context of a finite element scheme. Finite element programs, such as ABAQUS which is used for our simulations, provide a general interface so that a particular constitutive model can be introduced via a "user subroutine". A powerful tool, which is widely used nowadays to derive information regarding the functionality and the architecture of muscles, is the finite element method. Finite element methods can, in theory, account for the geometric irregularities, complex boundary conditions, large deformations, solid-fluid interactions, material heterogeneities and nonlinear anisotropic material behavior inherent to the muscle.

In addition to numerous Hill-based models, several more models are proposed in the literature for the modeling of muscle and are described in the following paragraphs. Most of them use a general form of a strain energy function to simulate the nearly incompressible behavior of the muscle tissue behavior of a hyperelastic material. The most common formulation of the strain energy function is a sum of a fiber term and a term related to the embedding matrix or a separation of the dilatational and deviatoric responses of the tissue where the deviatoric part represents the non-linear and anisotropic material properties of the muscle tissue while the dilatational part accounts for the constancy of muscle volume. In this category of models is assumed that the muscle is in a "preconditioned state" in which the material behavior may be represented as hyperelastic although the behavior of muscle tissue is time- and rate-dependent. Other attempts to model muscle tissue avoid using a hyperelastic material behavior. They are oriented to alternative finite element formulations by which the rate dependence is taken into account.

In particular, the year 1981 Hatze gave an analysis based on Hill's model incorporating muscle architecture and the serial and parallel arrangement of muscle fibers elements. The parameters of the elements determined the properties of the whole muscle. In the sense of a discrete model, that was the first step toward a finite element model. In 1984, Spencer studied the continuum mechanics of fiber-reinforced composites. He developed a constitutive hyperelastic model in which the strain energy function depends on a vector representing the material preferred direction ($\mathbf{a}_0$). Given the vector field defining the preferred direction $\mathbf{a}_0$ and $\mathbf{C}$, the right Cauchy-Green deformation tensor, Spencer presented relations for the strain energy at a material point in terms of five invariants derived from the tensor and vector fields. In 1987, Humphrey and Yin used Spencer's theory to define a pseudostrain energy function

and proposed a constitutive relation for the passive behavior of cardiac muscle neglecting its active behaviour. In the same year, Otten (1987) proposed a dynamic model of the jaw system of the rat, relating muscle force with muscle length, contraction velocity and stimulation rate, based on force-length relations, calcium dynamics and velocity-force relations. Later in 1989, Zajac proposed a 1-D model of the passive and active behavior of skeletal muscles. Huyghe *et al.* (1991) introduced a model for the passive behavior of the heart muscle with a quasi-linear viscoelastic formulation. The same year, Van Leeuwen described the stress in muscle as the sum of an active and a passive stress. In 1995, Otten and Hulliger proposed a model with a discrete arrangement of elements for the study of functional architecture in skeletal muscle. In 1996, Weiss *et al.* described a three-dimensional constitutive model for biological soft tissues and developed Spencer's theory to implement incompressible hyperelasticity that could accommodate transversely isotropic material symmetry. In their work a particular form of the strain energy for biological soft tissues was motivated and a finite element implementation of this model based on a three-field variational principle (deformation, pressure and dilatation) was presented. Another formulation of a discrete finite element code similar to that of Otten and Hulliger was given by van Leeuwen and Kier (1997), who proposed a 2-D model for the tentacle of a squid. They solved the problem of conservation of volume by reducing the 2-D to a 1-D problem and introducing the pressure as a free variable. This approach is only suitable for some symmetrical geometries. In 1998, Vankan *et al.* developed a finite element model of blood-perfused biological tissue, which contains a transversely isotropic, non-linearly elastic description of deforming muscle tissue. In the same year, van der Linden developed a muscle element and built a 2-D muscle finite element model. Also in 1998, Martins *et al.* adopted a constitutive relation which was a generalization of the model proposed by Humphrey and Yin for the passive behavior of cardiac muscle. This generalization was done in such a way as to make Humphrey's model compatible with Zajac's 1-D model of the passive and active behavior of skeletal muscles. In 2000, Gielen *et al.* described a geometrically and physically nonlinear continuum model to study the mechanical behavior of passive and active skeletal muscle. The contraction is described with a Huxley type model and a "Distributed Moments" approach is used to convert the Huxley partial differential equation in a set of ordinary differential equations. In the same year, Johansson *et al.* (2000) presented a finite element model based on nonlinear continuum mechanics. Stress in the muscle is assumed to result from the superposition of a passive and an active part. The passive properties are described by a hyperelastic constitutive material law whereas the active part depends on the fiber length, shortening velocity and an activation function. In 2001, Li *et al.* adapted the general theory of linear elasticity for transversely isotropic bodies and introduced nonlinearity by means of strain dependent elastic moduli. They used this approach to model porcine aortic heart valves. In 2002, Jenkin *et al.* modeled unipennate muscle as a two-dimensional material continuum that is incom-

pressible and nonlinearly anisotropic. In the same year, Yucesoy *et al.* (2002) proposed a model in which skeletal muscle is considered in two domains: a) the intracellural domain and b) extracellural matrix domain. The two domains were represented by two separate meshes that are linked elastically. By this way of modeling an assessment of force transmission and interaction between these domains is allowed. A model similar to that of Gielen *et al.* (2002) was proposed from Oomens *et al.* in 2003. In 2004, Tsui *et al.* developed an active finite element model to predict the mechanical behavior of skeletal muscle-tendon complex during isometric, shortening and lengthening contraction. The active finite element is controlled by a motor element that is activated by a mathematical function, neglecting the existence of muscle fibers, whereas the nonlinear passive behavior was defined by a viscoelastic element. Also in 2004, Lemos *et al.* developed a detailed continuum mechanics formulation to predict the deformation of skeletal muscle at different structural levels. Their model was used to investigate force production and structural changes during isometric and dynamic contractions of the cat medial gastrocnemius. In 2005, Blemker *et al.* modeled muscle as a fiber-reinforced composite with transversely isotropic material symmetry, similar to the approach previously used to represent ligament by Weiss *et al.* (1996). The model used an uncoupled form of the strain energy to simulate the nearly incompressible behavior of muscle tissue. This uncoupled form additively separated the dilatational and deviatoric responses of the tissue. The strain energy function used separated the material's responses to stretch in the fibers, shearing along fibers and shearing transverse to the fibers. To represent the intramuscular connective tissue's resistance to along-fiber and cross-fiber shear, Blemker *et al.* used two new strain invariants as described by Criscione *et al.* (2001). In addition, they created a fiber map, based on fascicle arrangement measurements from ultrasound images, so as to determine an exact fiber direction for each element in the mesh. Yekutieli *et al.* (2005) developed a two-dimensional, coarse grained, matrix based, structural dynamics model with incompressibility, lumped masses and discrete muscles, with some success at simulating bending and reaching of an octopus arm. In 2006, Liang *et al.* developed an explicit finite element scheme for biological hydrostats such as squid tentacles, octopus arms and elephant trunks. This approach builds upon previous effort of Van Leeuwen and Kier (1997). The scheme is implemented by embedding muscle fibers in finite elements. In any given element, the fiber orientation can be assigned arbitrarily and multiple muscle directions can be simulated. The mechanical stress in each muscle fiber is the sum of an active and a passive part. The active stress is taken to be a function of activation state, muscle fiber velocity and fiber strain, while the passive stress depends only on the strain. The finite element is treated as a continuum with muscle fibers aligned in a given direction. This general explicit finite element formulation for the simulation of the movements of muscular hydrostats can be viewed as a generalization and formalization of the work of Yekutieli *et al.* (2005).

1.1.2 Human lower extremity modeling

The lower extremity is of special interest because it is the primary physical interaction between the body and the ground during locomotion. It has been pointed out by many researchers that biomechanical factors play an important role on the etiology, prevention and treatment of many lower extremity disorders. Increasingly, musculoskeletal models of the lower extremity are used as powerful tools to study various effects on biological structures behavior such as illness and injuries. However, these models frequently have limited functionality and lack of details necessary to provide meaningful insights into biomechanical behavior.

One basic issue for successful modeling of human body parts and tissues is the accurate representation of their geometrical characteristics. The significant progress in medical imaging techniques led to a revolution in that direction. The geometry of skeleton, muscles and any other body structure is obtained from 3D reconstruction of CT (Computed Tomography) or/and MRI (Magnetic Resonance Imaging) images of human subjects. In Chapter 6 section 6.4 a detailed description of the procedure that can be followed to obtain accurate volume finite element meshes of human body parts from medical images is presented. Consequently, modeling attempts of human structures dated prior to the medical imaging revolution have limited scientific value in our days.

Once accurate representation of geometry is achieved the next important issue in musculoskeletal modeling is the realistic representation of the mechanical behavior of biological materials. Although the mechanical properties of skeletal components can be well-defined through experiments, the same does not stand for the muscular parts due to their complex active and passive behavior. This is the reason why the particular mechanical behavior of muscles is missing from the majority of human models presented in the literature. However, it is scientifically stated that by including the actual biomechanical behavior of muscle tissue in a computational model of a biological structure provides a better understanding to the whole body internal loadings.

In particular, Gefen *et al.* (2000) were the first to use a three dimensional numerical model of the foot incorporating realistic geometric and material properties of both skeletal and soft tissue components of the foot except muscles. This model was used to study biomechanical loadings of the foot structure during gait and specific clinical cases, such as surgical plantar aponeurosis (fascia) release and plantar soft tissue loadings in the standing diabetic foot. Chen *et al.* (2001) also used a geometrically accurate model of the foot to quantify stress distribution of the foot during mid-stance to push-off in barefoot gait. The next year, Camacho *et al.* (2002) developed a three dimensional anatomically detailed foot model for finite element simulation and quantification of foot-bone positions. Cheung *et al.* (2004, 2005, 2006) developed a three dimensional finite element model of the foot to

study the material sensitivity of the soft tissue in the standing foot, the effect of Achilles tendon loading on plantar fascia tension in the standing foot, and the effects of plantar fascia stiffness on the biomechanical responses of the foot-ankle complex. Spyrou *et al.* (2006) also developed a geometrically accurate three dimensional finite element model of the foot during the mid-stance phase of gait for a stress-strain analysis on the whole foot structure. Finally, Wu (2007) developed a model of the foot including some tendons and muscles as independent parts, but muscles were modeled only as passive structures.

1.2 Thesis overview

In this thesis, special emphasis is given to muscle tissue and its properties. Chapter 2 includes anatomical, physiological, and material characteristics of the skeletal muscle. Muscle has the ability to produce force and that makes it distinct from other biological materials. The mechanism that results in muscle force production is described. The amount of the produced muscle force depends on several parameters such as the muscle fiber length, the muscle fiber velocity of contraction, the activation level, the muscle architecture (fiber direction with regard to tendon's long axis), the fiber type (slow or fast), and the fiber's cross sectional area. The dependence of muscle force on all these parameters is described.

In Chapter 3 anatomical and material characteristics of the rest biological materials excluding muscle are described. A thorough examination of materials such as bone, ligament, cartilage, and tendon is included. These materials do not produce force like muscle does. Knowledge of their structure and thus of their mechanical behavior is of great importance in studies of biological systems.

Chapters 4 and 5 are the core chapters in the thesis. In Chapter 4 a continuum three dimensional constitutive model for the muscle tissue is developed. The model takes into account all the parameters that affect the production of muscle force. The model is extended so that it can describe the behavior of tendon tissues as well. In Chapter 5 the numerical implementation of the proposed constitutive model is described. The implementation of the model in a finite element code (ABAQUS) involves the integration of the constitutive equations at the Gauss integration points of the elements and the calculation of the corresponding "linearization moduli" that are needed for the global equilibrium "Newton loop".

In Chapter 6 the developed constitutive model is used to study the biomechanical behavior of several muscle-tendon structures. The extension of a squid tentacle during the strike to catch prey is simulated, and the behavior of a parallel fibered and a pennated muscle is studied. Also, the model is used to study the behavior of the human semitendinosus muscle. In addition, a methodology for developing geometrically accurate three dimensional models of biological structures is described. That methodology is used to develop a model of the human lower-extremity. The constitutive model of muscle and tendon tissues is applied to

the muscles and tendons of the human leg.

Finally, Chapter 7 provides a brief summary of the contribution of this work together with some prospects for future work.

Chapter 2

Muscle Anatomy and Material Characteristics

This chapter deals with the thorough examination of the anatomical and material characteristics of muscle tissue. The purpose of this chapter is to provide insight into the mechanical aspects of construction and function of muscle.

There are three muscle types that can be found in the human muscular system: the **cardiac** muscle, which composes the heart; the **smooth** muscle, which lines the hollow internal organs such as blood vessels, the gastrointestinal tract, the bladder, or the uterus; and the **skeletal** muscle, which attaches to the skeleton via the tendons. The focus of this chapter is the anatomy and function of skeletal muscle.

The basic property of muscle is its ability to produce force; its capability of active contraction makes it distinct from other soft biological tissues. Therefore, muscles perform both dynamic and static work. Dynamic work permits locomotion and the positioning of the body segments in space whereas static work maintains body posture or position.

2.1 Anatomy

The structural unit of skeletal muscle is the muscle fiber. Each skeletal muscle fiber is a single cylindrical muscle cell. Muscle fibers range in thickness from 10 to 100 μm and in length from 1 to 30 cm. An individual skeletal muscle may be made up of hundreds or even thousands of muscle fibers bundled together and wrapped in a connective tissue covering. Each muscle is surrounded by a connective tissue sheath called the epimysium. Fascia, connective tissue outside the epimysium, surrounds and separates the muscles. Portions of the epimysium project inward to divide the muscle into compartments. Each compartment contains a bundle of muscle fibers. Each bundle of muscle fibers is called a fascicle and is surrounded by a layer of connective tissue called the perimysium. Within the fascicle, each individual muscle cell, called a muscle fiber, is surrounded by connective tissue called the endomysium (Figs 2.1 and 2.2).

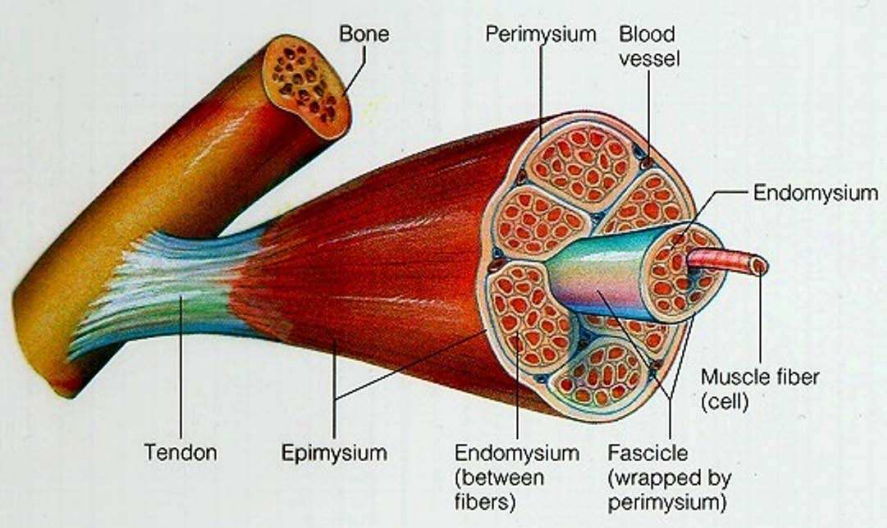

Figure 2.1: Structural hierarchy of skeletal muscle from muscle to muscle fiber.

Muscle fibers are composed of parallel bundles of myofibrils (Fig. 2.2).

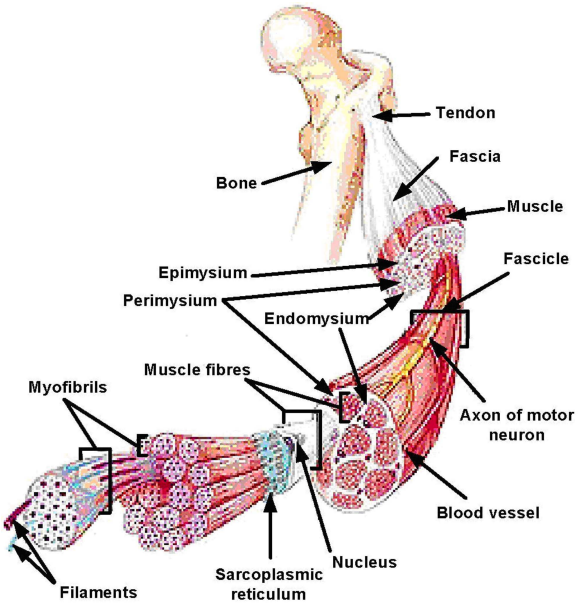

Figure 2.2: Structural hierarchy of skeletal muscle from muscle to myofilaments. (From Van Loocke *et al.*, 2004)

The myofibrils are invested by a delicate plasma membrane called the sarcolemma. The systematic arrangement of the myofibrils gives skeletal muscle its typical striated pattern. The repeat unit in this pattern is called sarcomere and it is the basic contractile unit of a muscle. Sarcomeres are bordered by the Z-lines and contain thin filaments composed of the protein actin, thick filaments composed of the protein myosin, and filaments composed of the two exceptionally large proteins titin and nebulin which have implications in the passive

elasticity of the muscle (Fig. 2.3).

Two additional proteins, troponin and tropomyosin, are important constituents of actin because they appear to regulate the making and breaking of contacts between the actin and myosin filaments during contraction (Fig. 2.3). Finally, the heads on the myosin body (bridges) attach to the thin filament to form a cross-bridge. The mechanism of cross-bridge attachment and cross-bridge movement that is believed to cause relative movements of the myofilaments is presented in detail in the section 2.1.1.

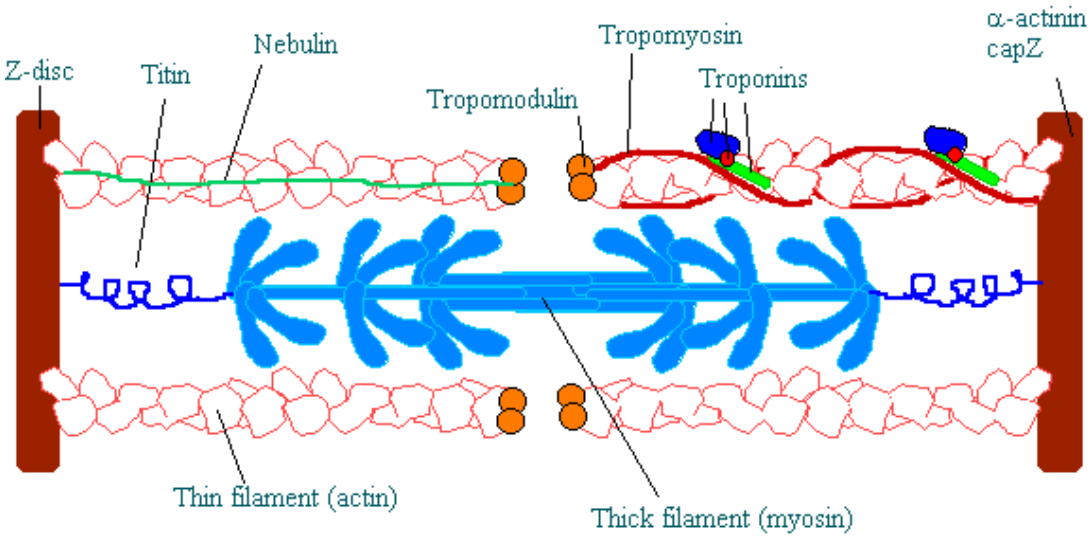

Figure 2.3: Microstructure of a sarcomere. (From http://www.bms.ed.ac.uk)

In humans, thin filament diameters and lengths appear to be about 5 nm and 1.27 μm respectively. The corresponding values for thick filament are about 15 nm and 1.6 μm, which are nearly constant among many animal species (Walker and Schrodt (1973), Kimball).

2.1.1 Cross-bridge theory

Despite centuries of research on muscle and its contractile behavior, some aspects of muscular force production have still not been resolved. For example, the precise mechanism of cross-bridge attachment and cross-bridge movement that are believed to cause relative movements of the myofilaments, and so produce force, are not clearly understood.

Some scientists (Iwazumi, 1978; Pollack, 1990) propose mechanisms of force production that do not agree with the most popular paradigm of muscular force production, the cross-bridge theory (Huxley, 1957; Huxley and Simmons, 1971). Before 1954, most theories of muscular contraction were based on the idea that shortening and force production were the result of some kind of folding or coiling of the myofilaments (particularly the thick filaments) at specialized sites. In 1954 H.E. Huxley and Hanson (1954) as well as A.F. Huxley and Niedergerke (1954) demonstrated that muscle shortening was not associated with

an appreciable amount of myofilament shortening, and, therefore, postulated that muscle shortening is probably caused by a sliding of the thin past the thick myofilaments, named the *sliding filament theory*. The mechanism whereby this myofilament sliding is produced was proposed by A.F. Huxley (1957), and is referred to as the *cross-bridge theory*. The original theory of A.F. Huxley (1957) and the theories that have followed are variations on the development or modulation of the numbers of cross-bridges attached. More recent theories (Lymn and Taylor, 1971; A.F. Huxley, 1973, 1974; Eisenberg *et al.*, 1980; Eisenberg and Hill, 1985) include multiple binding states with kinetic schemes that govern the transition rates between these states.

The *sliding filament theory* is a hypothesis used to explain the mechanism of contraction of striated muscle which proposes that the parallel, interdigitated, thick myosin and thin actin filaments slide past one another to varying degrees causing the cell as a whole to shorten and the muscle to contract. This is brought about through the sequential formation of cross-bridges between the actin and myosin molecules such that the filaments move past one another in a ratchet-like manner. The energy for these processes is provided by the hydrolysis of ATP.

The mechanism that describes how the myofilament sliding is produced, is a sequence of stages called *myosin cross-bridge cycle*. The *cycle* is presented in the following figure.

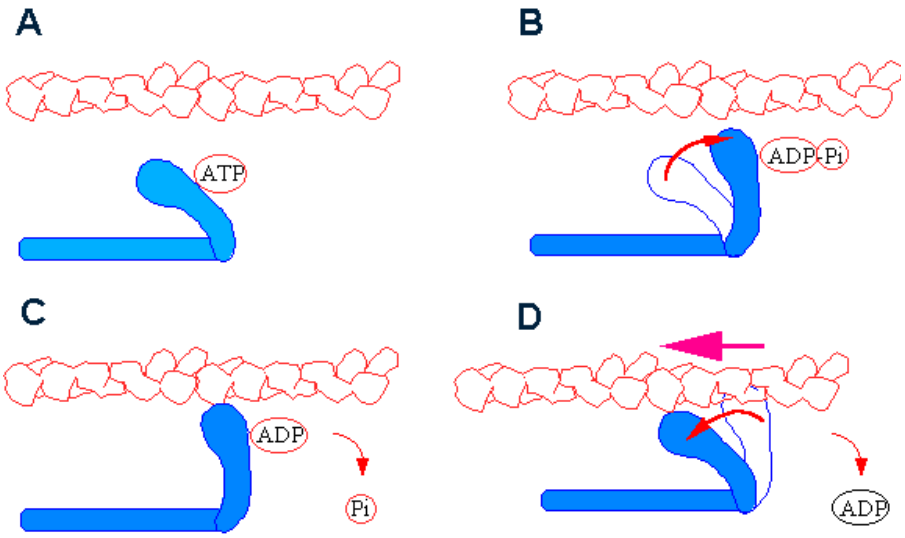

Figure 2.4: The cross-bridge cycle. (From http://www.bms.ed.ac.uk)

A. There is ATP binding at the back of the head of a cross-bridge on the myosin filament causing a conformation which cannot bind actin.

B. As the ATP is hydrolyzed, the head swings back about 5 *nm* to the "cocked" position where ADP and Pi (inorganic phosphate) remain bound.

C. When Pi leaves the myosin, the head binds the actin. The actin binding sites are uncovered by the release of Calcium (Ca^{+2}).

D. The head rotates, causing the sliding of the actin filament against the myosin filament. ADP is released to continue the cycle.

In 1957 A.F. Huxley suggested and in 1966 A.M. Gordon *et al.* showed with measurements that the existing sliding filament theory should include the further proposition that the points where the force is generated are the bridges (*cross-bridge theory*).

2.2 Physical properties

The force developed by a muscle during contraction varies with its length and its velocity. These properties are the force-length and the force-velocity relations of muscle which are repeatedly used in biomechanical experiments involving muscles or the musculoskeletal system. Force-length and force-velocity relations of skeletal muscular tissues are interrelated to the activation level of the muscle, the fiber arrangement in the muscle and the fiber type. The purpose of the following sections is to provide insight to the factors that affect the force a muscle can exert.

2.2.1 Force-Length relation

The force-length relation is defined as the relation that exists between the maximal force of a muscle (or fiber or sarcomere) and its length. Force-length relations are obtained under isometric conditions (the muscle length is kept constant) and for maximal activation of the muscle. Experimentally, isometric contractions are performed at different lengths and peak isometric force is measured at each length. These forces are then plotted against length and a relationship such as that shown in Fig. 2.5 is obtained. It has been demonstrated that at very long and very short lengths, muscle generate low force while at intermediate or "optimal" lengths, muscle generate higher force.

Blix (1894) described over a century ago that the force a muscle can exert depends on its length. Although a general description of this relationship was presented in the late 1800's, the precise structural basis for the force-length relationship in skeletal muscle was not elucidated until the sophisticated mechanical experiments of the early 1960's were performed. In 1966, Gordon *et al.* published the results of a classical study in which they showed the dependence of force production in isolated fibers of frog skeletal muscle on sarcomere length. Their results were in close agreement with theoretical predictions that were based on the cross-bridge theory; results that helped to establish the cross-bridge theory as the primary mechanism to describe muscular force production.

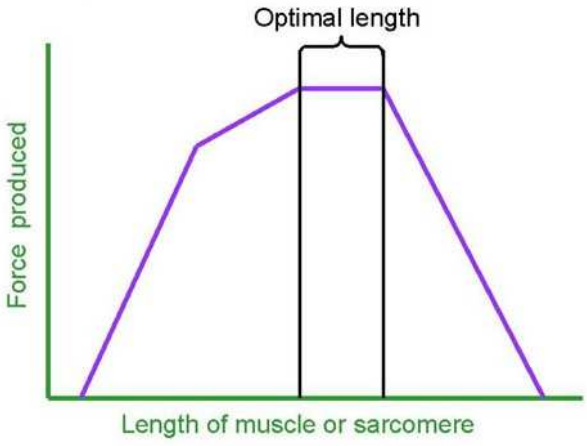

Figure 2.5: Typical force-length relation for muscle or fiber or sarcomere. At "optimal" lengths, maximum force is generated. (From http://biology.kenyon.edu)

According to the cross-bridge theory, cross-bridges extend from thick to thin filaments and cause sliding of the myofilaments past one another. Each cross-bridge is assumed to generate, on average, the same amount of force and work independently of the remaining cross-bridges. Since the cross-bridges are believed to be arranged at equal distances along the thick filament, overlap between thick and thin filaments determines the number of possible cross-bridge formations and thus the total force that may be exerted.

In its basic form, the force-length relationship illustrates that force generation in skeletal muscle is a direct function of the magnitude of overlap between the actin and myosin filaments. For frog skeletal muscle the force-length relationship is shown in Fig. 2.6 as presented by Gordon *et al.* (1966). The thick and thin filament lengths are reported to be about 1.6 μm and 0.95 μm respectively, the width of the Z-disc is about 0.1 μm and the H-zone (cross-bridge free zone in the middle of the thick filament) is 0.2 μm. At long sarcomere lengths, thick and thin filaments cease to overlap and no cross-bridges can be formed. The corresponding force must be zero. For frog skeletal muscle, zero force is reached at a sarcomere length of about 3.6 μm (thick filament length (1.6 μm) plus twice the thin filament length (1.9 μm) plus the width of the Z-disc (0.1 μm)) (Fig. 2.7).

Shortening of the sarcomeres increases the number of potential cross-bridge formations in a linear manner with sarcomere length or correspondingly, thick and thin filament overlap, until a maximal number of cross-bridge formations are possible. This optimal overlap corresponds to a sarcomere length of 2.2 μm in frog muscle (Fig. 2.7). Further sarcomere shortening to 2.0 μm increases the area of overlap between thick and thin myofilaments but does not increase the number of possible cross-bridge formations, since the middle part of the thick filament does not contain cross-bridges. Therefore, the force remains constant between 2.0 and 2.2 μm. Sarcomere shortening below 2.0 μm has been associated with a

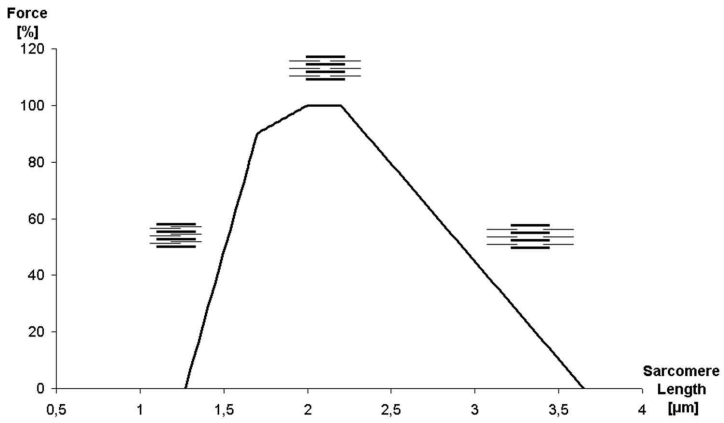

Figure 2.6: Force-length relation for frog skeletal muscle as presented by Gordon *et al.* (1966).

decrease in force caused by interference of thin myofilaments as they start to overlap. Below 1.7 μm the rate of decrease in force becomes higher than that of the region between 1.7 and 2.0 μm. This steeper decline in force for a given amount of sarcomere shortening has traditionally been associated with the force required to deform the thick filament. For frog skeletal muscle, zero force is reached at a sarcomere length of 1.27 μm.

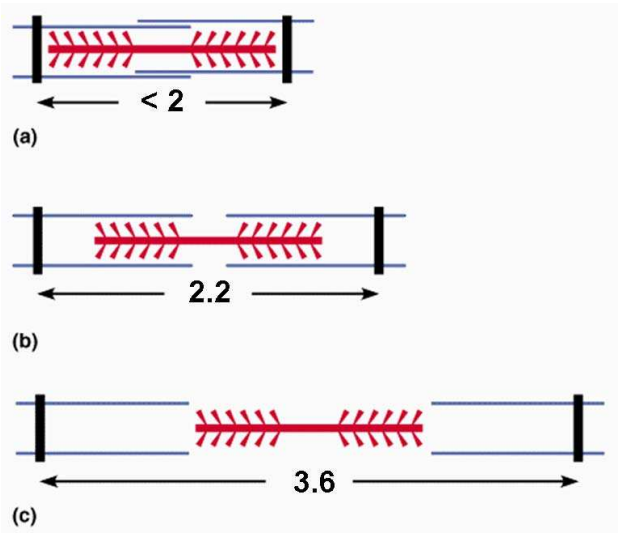

Figure 2.7: Sarcomere's thin and thick filament overlap. (a) Thin filaments start to overlap causing decrease in force generation. (b) Optimal overlap of thick and thin filaments causing the maximum force generation. (c) No overlap between thick and thin filaments causing zero force generation

Probably the most important result in support of the cross-bridge theory was the linear relation between force and length for sarcomere lengths between 2.2 and 3.6 μm. However, the strict linearity of this relation was questioned by several investigators who showed non-linear force-length behavior (e.g. ter Keurs *et al.* (1978)) (Fig. 2.8).

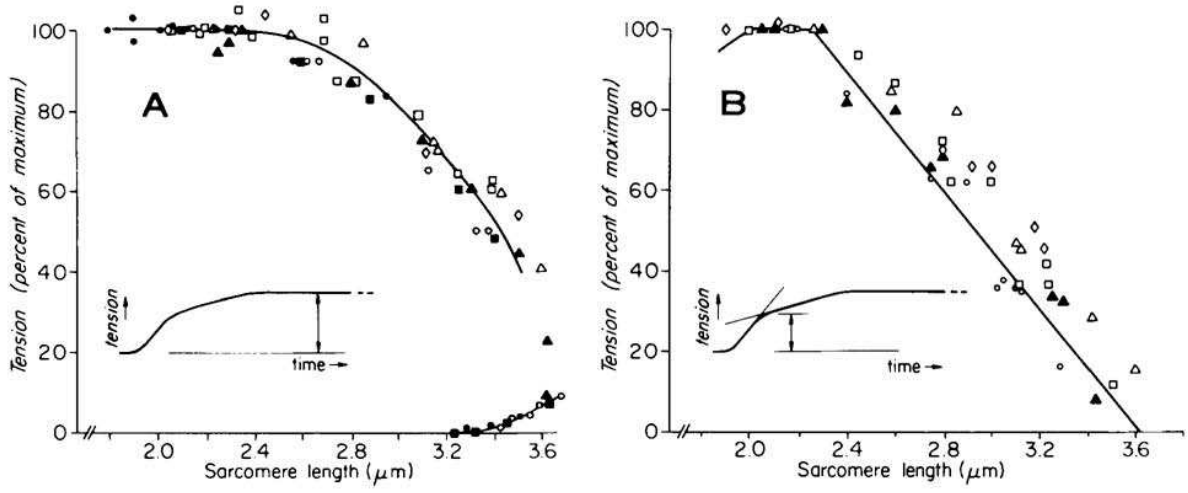

Figure 2.8: Tension-sarcomere length relation. (A) Results as presented by ter Keurs *et al.* (1978). (B) Results as presented by Gordon *et al.* (1966). (From ter Keurs *et al.* (1978))

The difference between studies showing linear and non-linear force-length behavior was in the length control of the sarcomeres. The studies showing a linear relation kept sarcomeres at a constant (controlled) length, whereas those showing a non-linear relation kept fiber length constant but allowed for non-uniform changes in sarcomere length. This latter situation appears to approach actual physiologic conditions more appropriately and thus may be more relevant in studying intact skeletal muscles.

In addition to the active force-length properties of the muscle, passive force-length properties play a role as well. Passive force is developed if a muscle is stretched to various lengths without stimulation. Near the optimal length passive force is almost zero. However, as the muscle is stretched to longer lengths, passive force increases dramatically (Fig. 2.9). These relatively long lengths can be attained physiologically and, therefore, passive tension can play a role in providing resistive force even in the absence of muscle activation. The structures responsible for passive tension are obviously outside of the cross-bridges since muscle activation is not required. The large protein titin which connects the thick myosin filaments end to end has been identified as the source of this passive tension (Horowits (1992), Linke *et al.* (1996), Granzier *et al.* (2000)).

The muscle force-length is also coupled to the level of activation. As cited in Buchanan *et al.* (2004), Huijing (1996) has shown that optimal fiber lengths increase as activation decreases (Fig. 2.10), which has also been reported by Guimaraes *et al.* (1994).

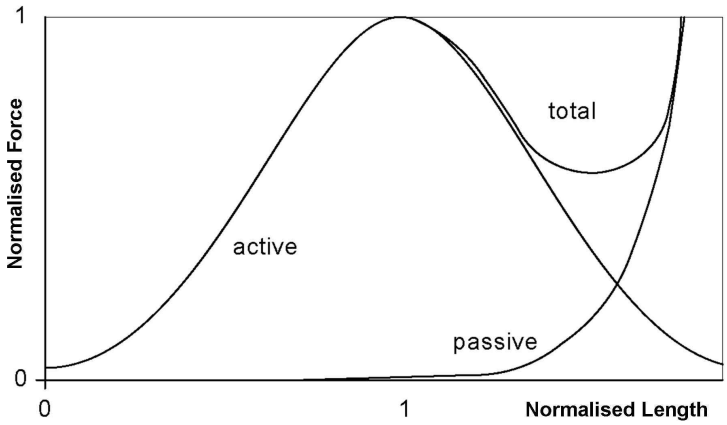

Figure 2.9: Active, passive and total normalized force-length relation.

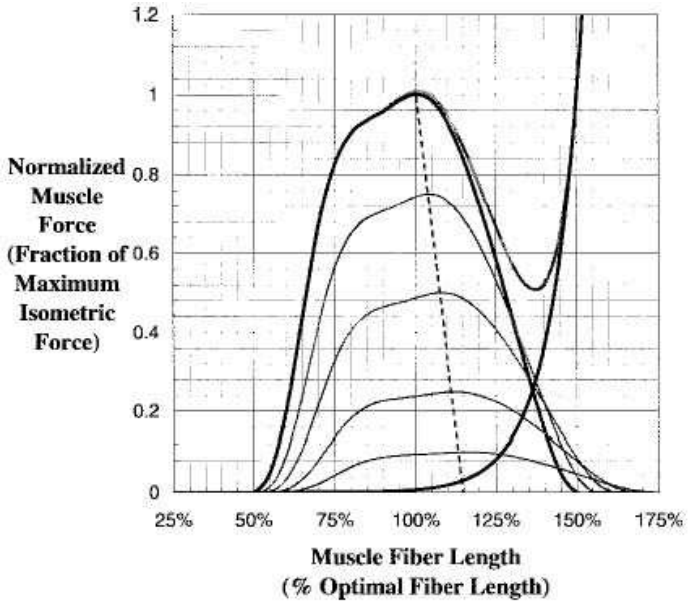

Figure 2.10: Normalized force-length relationship for muscle. Thick dark lines indicate maximum activation, whereas the light thin lines are lower levels of activation. The optimal fiber length is longer as the activation decreases. (From Buchanan *et al.*, 2004)

2.2.2 Force-Velocity relation

In contrast to the sarcomere force-length relationship, the force-velocity relationship does not have a precise, anatomically identifiable basis. Force-velocity relations illustrate the strong relation between the maximal force a muscle (or fiber) can exert and its instantaneous rate of change in length. Force-velocity properties are determined for maximal activation conditions of the muscle and are obtained at optimal length of the sarcomeres.

Fenn and Marsh (1935) were the first to perform experiments and report results on force-velocity properties of muscles. Their work was followed by the classic study of Hill (1938) who determined the effect of load on speed of shortening on isolated frog skeletal muscle. This relation is the basis of the "viscoelasticity" of skeletal muscle.

The force-velocity relationship, like the force-length relationship, is a curve that represents the results of many experiments plotted on the same graph. Experimentally, a muscle is stimulated maximally and allowed to shorten (or lengthen) against a constant load. The muscle velocity during shortening (or lengthening) is measured and then plotted against the resistive force. A general form of this relationship is shown in Fig. 2.11.

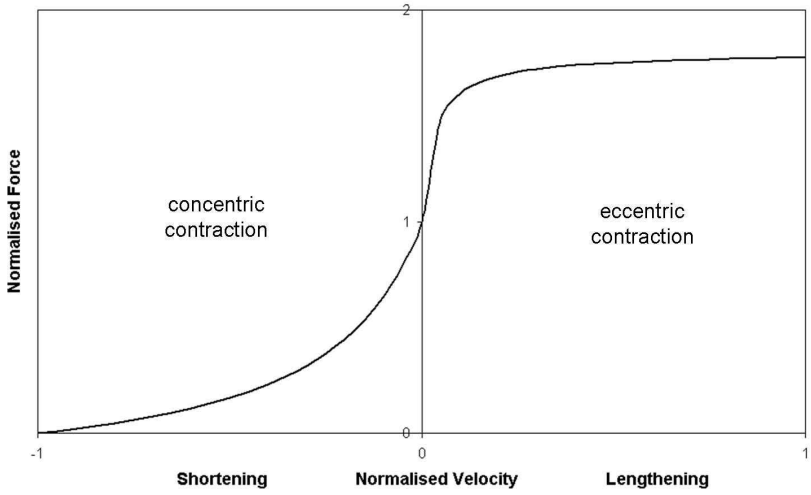

Figure 2.11: Normalized force-shortening velocity and force-lengthening velocity of muscle.

When a muscle is maximally activated and required to lift a load which is less than its maximum force capacity, the muscle begins to shorten. Contractions that permit the muscle to shorten are called concentric contractions. In concentric contractions the force generated by the muscle is always less than the muscle's maximum. As the load, the muscle is required to lift, decreases, contraction velocity increases. This occurs until the muscle finally reaches its maximum contraction velocity, at which force generation is zero.

As the load imposed on the muscle increases, it reaches a point where the external load is greater than the load which the muscle itself can generate. Thus the muscle is

activated, but it is forced to lengthen due to the high external load. Contractions that force the muscle to lengthen are called eccentric contractions. All the movement patterns where muscles function as brakes to decelerate a limb have to do with eccentric actions. There is interest in studying eccentric actions of muscle because much of a muscle's normal activity occurs while it is actively lengthening; muscle injury and pain are, in many cases, associated with eccentric contraction; and muscle strengthening is greatest using exercises that involve eccentric contractions.

The mathematical form of the force-shortening velocity relationship as proposed by Hill is:

$$(F + a)\, v = b\,(F_0 - F) \tag{2.1}$$

or

$$F = \frac{b\,F_0 - a\,v}{b + v}, \tag{2.2}$$

where F is the instantaneous force, F_0 is the maximal force at zero velocity and optimal sarcomere length, v is the shortening velocity, and a, b are constants with units of force and velocity respectively. For $v = v_{\max}$ the force is zero ($F = 0$). Therefore, from equation (2.2) the result is:

$$v_{\max} = \frac{b\,F_0}{a}. \tag{2.3}$$

If we divide both parts of the fraction on the right hand side of equation (2.2) with $v_{\max}$, then the normalized equation of Hill is derived:

$$\frac{F}{F_0} = \frac{1 - \frac{v}{v_{\max}}}{1 + \frac{1}{k}\frac{v}{v_{\max}}}, \tag{2.4}$$

where k is proved to vary with species and fiber type (fast or slow).

Force-velocity properties are typically obtained at optimal sarcomere lengths. However, it has been suggested that Hill's equation may still be applied at sarcomere lengths other than those corresponding to optimal length. The first approach was to consider the maximal isometric force as a function of sarcomere length ℓ. Therefore, instead of equation (2.2), the following equation (2.5) arises:

$$F = \frac{b\,F_0\,(\ell) - a\,v}{b + v}. \tag{2.5}$$

If we solve equation (2.5) for $v = v_{\max}$ the result is:

$$v_{\max} = \frac{b\,F_0\,(\ell)}{a}, \tag{2.6}$$

which implies that maximal muscle fiber velocity depends on muscle's length ℓ. However, according to Edman (1979), maximal muscle fiber velocity is constant for most of a muscle's

operating range. For this reason, a better approach is the entire right hand side of equation (2.2) to be multiplied by a factor c:

$$F = \left(\frac{b\,F_0 - a\,v}{b + v} \right) c, \tag{2.7}$$

where $c(\ell)$ takes a value between 0 and 1, representing the normalized force of a muscle as a function of sarcomere length. For optimal sarcomere length ($c = 1$) equation (2.7) takes the form of equation (2.2). Also the maximal muscle fiber velocity remains constant for all values of c. Equation (2.7) appears to approximate experimental observations better than the one suggested by equation (2.2).

The mathematical form of the force-lengthening velocity relationship is:

$$F = 1.8 - 0.8 \frac{v_{\max} + v}{v_{\max} - 7.56\,v} \tag{2.8}$$

as formulated by Otten (1987) based on stretch experiments of vertebrate muscles by Aubert (1956).

The normalized formulation is:

$$\frac{F}{F_0} = 1.8 - 0.8 \frac{1 + \frac{v}{v_{\max}}}{1 - \frac{7.56\,v}{k\,v_{\max}}}, \tag{2.9}$$

where k varies with species and fiber type (fast or slow). The parameter k was calculated from the measurements of Close (1964) for fast and slow fiber types where $k = 0.25$ for fast fibers and $k = 0.17$ for slow fibers.

If equation (2.8) is applied at sarcomere lengths other than those corresponding to optimal length then equation (2.10) arises:

$$F = \left(1.8 - 0.8 \frac{v_{\max} + v}{v_{\max} - 7.56\,v} \right) c, \tag{2.10}$$

where $c(\ell)$ takes a value between 0 and 1, representing the normalized force of a muscle as a function of sarcomere length. For optimal sarcomere length ($c = 1$) equation (2.10) takes the form of equation (2.8).

A typical force-velocity relation for different initial lengths (ℓ) is shown in Fig. 2.12.

In addition, Epstein and Herzog (1998) state that the preferred combined equations should be

$$F = \left(\frac{b\,F_0 - a\,v}{b + v} \right) f(\ell), \tag{2.11}$$

and

$$F = \left(1.8 - 0.8 \frac{v_{\max} + v}{v_{\max} - 7.56\,v} \right) f(\ell), \tag{2.12}$$

where $f(\ell)$ is the normalized force-length relationship.

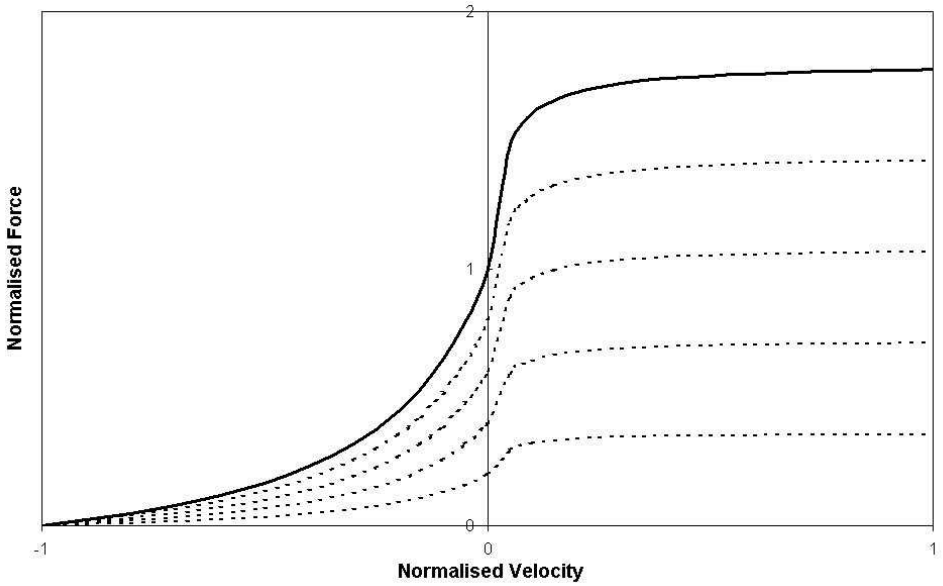

Figure 2.12: Force-velocity relation for different initial lengths ℓ. Solid line corresponds to optimal fiber length ($c = 1$). The dashed lines result for different values of the parameter $c < 1$.

2.2.3 Force-Activation relation

Another important mechanical characteristic of muscle is related to its activation profile during a movement and the dependence of force generated to the level of activation. A typical relation between force and time is shown in Fig. 2.13 in which the force exerted by the muscle is greater when the contraction time is longer.

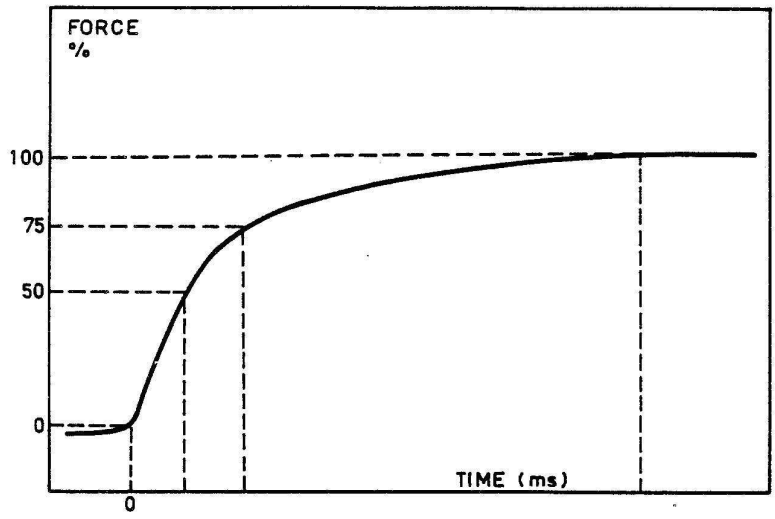

Figure 2.13: Typical force-activation relationship of muscle. (From Viitasalo and Komi, 1978)

However, the role of activation level in not only to adjust the magnitude of force. Its role is rather complex, as shown in Fig. 2.10, and this is something that must be always kept in

mind.

2.2.4 Muscle Architecture and Fiber Types

Except for the relationship of muscle force to its length, velocity, and activation there are other factors influencing force and/or rate of contraction as well, such as the fiber type and the fiber organization in a muscle structure.

As described in section 2.1.1, ATP has the primal role in the *myosin cross-bridge cycle*. The fiber types are distinguished mainly by the metabolic pathways by which they can generate ATP and the rate at which its energy is made available to the contractile system of the sarcomere, which determines the speed of contraction. There are three types of muscle fibers found in the human body:

- type I, slow-twitch (ST) oxidative (SO) fibers,
- type IIA, fast-twitch (FT) oxidative-glycolytic (FOG) fibers,
- type IIB, fast-twitch (FT) glycolytic (FG) fibers.

Type I (SO) fibers are characterized by a low activity of myosin ATPase and, therefore, a relatively slow contraction time (low $v_{\max}$). SO fibers contain many mitochondria and get most of their ATP from oxidative phosphorylation. This source supplies ATP rapidly, and thus the SO fibers are able to sustain contractions longer without fatiguing. Also SO fibers receive and use more oxygen than FG fibers. Therefore, the SO fibers are well suited for low-intensity activities where fast acceleration is not the point of interest. Muscles with higher percentages of SO fibers have a clear advantage in long-duration, endurance related events. On the other hand, type IIB (FG) fibers are characterized by a high activity of myosin ATPase and, therefore, a relatively fast contraction time (high $v_{\max}$). FG fibers contain few mitochondria and get most of their ATP from glycolysis, the breakdown of glycogen into lactic acid. This source of ATP is not as efficient as oxidative phosphorylation, and therefore FG fibers fatigue more rapidly than SO fibers. These deficiencies of FG fibers may not be a big problem because they tend to be active for only short periods in normal behavior. Thus, muscles with higher percentages of FG fibers have a clear advantage in short-duration, sprint-like activities. Type IIA (FOG) fibers are considered intermediate between type I and type IIB because their fast contraction time is combined with a well-developed capacity for both aerobic (oxidative) and anaerobic (glycolytic) activity. Although a motor unit (a group of muscle fibers activated in the same time by one single motor nerve fiber) consists of only one kind of muscle fibers, most muscles are mixtures of FG, SO and FOG fibers.

Fig. 2.14 shows the differences in the rise and decay of tension between fiber types. Although maximal force is identical for equal cross-sectional areas, the action which produces this force is much more rapid in FG fibers than in SO fibers.

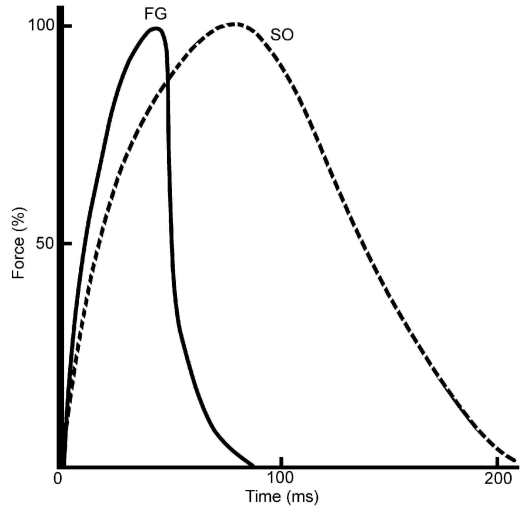

Figure 2.14: Force-activation relationship for slow SO and fast FG muscle fibers.

Fig. 2.15 shows how the potential speed of contraction is affected between slow-twitch SO fibers and fast-twitch FOG and FG fibers. For a given rate of shortening, high $v_{\max}$ muscles including FOG and FG fibers produce more force than muscles with low $v_{\max}$.

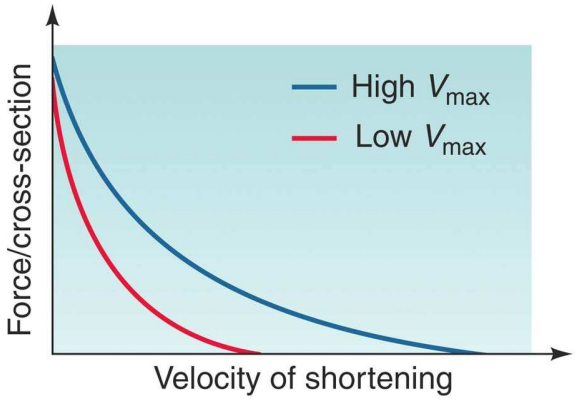

Figure 2.15: Force-shortening velocity relation for slow (low $v_{\max}$) and fast (high $v_{\max}$) muscle fibers.

Another important factor influencing force and/or rate of contraction is the muscle architecture. Muscle architecture involves fiber arrangement in a muscle and this arrangement is not the same in all muscles. Some of muscle architectures are the parallel, unipennate and bipennate which can be shown in Fig. 2.16.

A muscle is called parallel when the longitudinal direction of muscle fibers; direction in which the force is developed, is in parallel with the line of action of the whole muscle-tendon complex. In contrast, a muscle is called pennate when the longitudinal direction of muscle fibers lies at an angle (pennation angle) to the line of action of the whole muscle-tendon complex (Fig. 2.16). Therefore, the force transmission in a parallel muscle to tendon is 100%

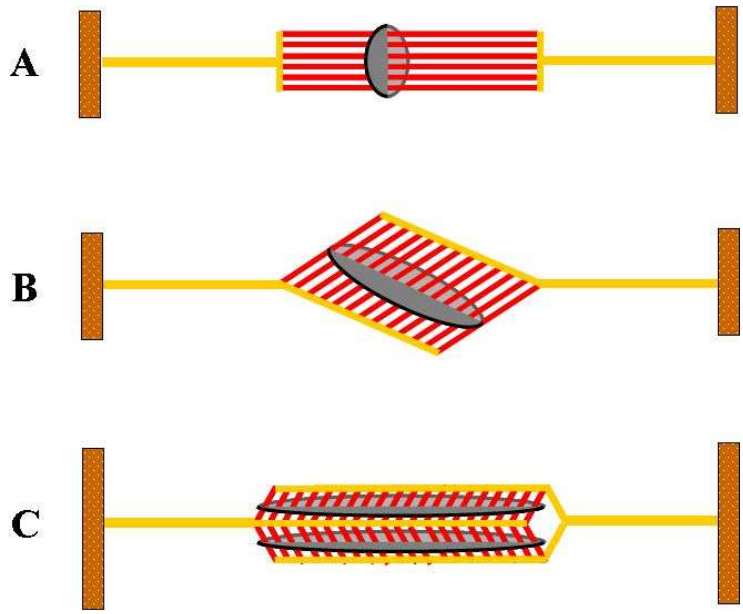

Figure 2.16: Muscle architectures and corresponding cross-sectional areas. (A) parallel muscle. (B) unipennate muscle. (C) bipennate muscle

efficient whereas in a pennate muscle the force transmission efficiency is reduced according to the corresponding angle of pennation (force multiplied by the cosine of the angle). However, the pennate muscle allows for a large number of fibers to be packed side-by-side to each other. In Fig. 2.16 is depicted that for a muscle with the same volume

- fibers in a parallel muscle are longer than those of a pennate,
- the number of fibers in a parallel muscle is smaller that that of a pennate,
- the cross-sectional area of a parallel muscle is smaller than that of a pennate.

The maximum force a muscle can generate depends on its *physiological cross-section area* (PCSA). In fact the maximum force can be calculated by multiplying the PCSA by a constant (approximately 20 to 100 N/cm^2). Therefore, a pennate muscle, due to its bigger PCSA, is stronger than a parallel-fibered muscle (Fig. 2.17). However, a parallel muscle can exert forces over a larger range of absolute muscle length than the pennate muscle (Fig. 2.17). Pennation is a non-ideal mechanism. The most efficient option is to have the line of action parallel to the muscle fibers - any angular difference means that energy is wasted producing tension in directions where it cannot be used. However the physical layout of the skeleton is such that we often need high absolute forces rather than contraction distance or/and high maximal contraction velocity and pennation is a mechanism that allows this (Fig. 2.17, Fig. 2.18).

In addition, Fig. 2.18 shows the differences in force-length and force-velocity relationships to muscles with different PCSA but same fiber length. In Fig. 2.19 the differences in force-

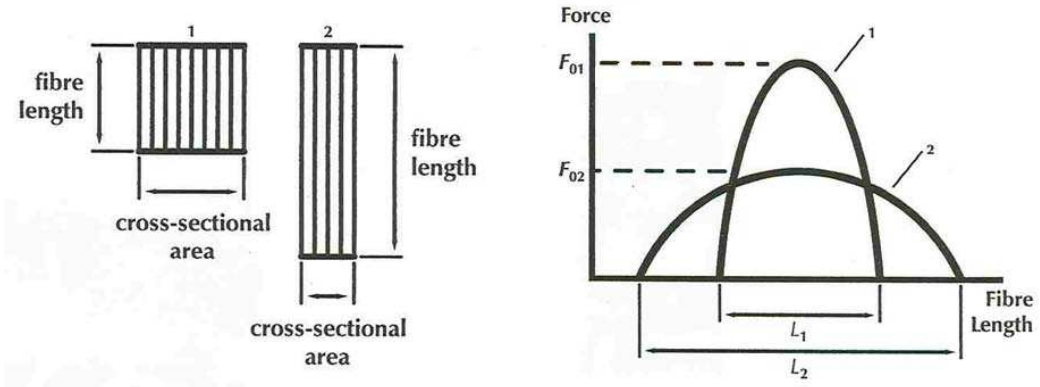

Figure 2.17: Force-length relationship of two muscles with different cross-sectional areas and fiber length, but equal volume. (From Nigg and Herzog, 1999)

length and force-velocity relationships to muscles with different both PCSA and fiber length are depicted.

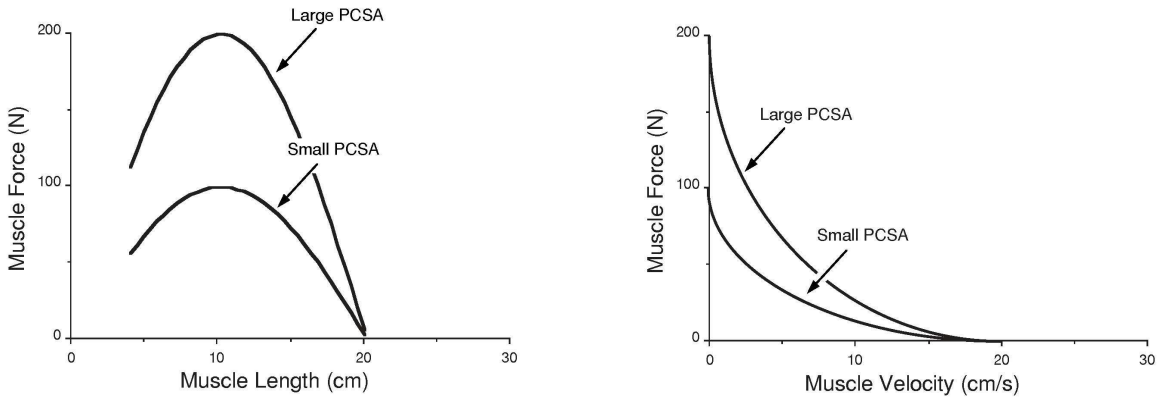

Figure 2.18: Force-length and force-velocity relationships for two muscles with different PCSA but the same fiber length. (From Nordin and Frankel, 2001)

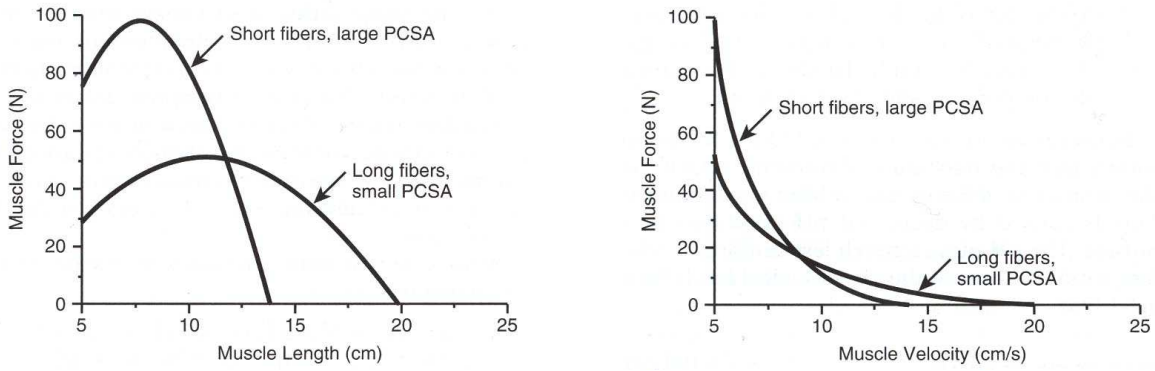

Figure 2.19: Force-length and force-velocity relationships for two muscles with different both PCSA and fiber length. (From Nordin and Frankel, 2001)

Chapter 3

Anatomy and material characteristics of biological structures

This chapter deals with the thorough examination of the anatomical and material characteristics of biological materials other than muscle tissue, such as bone, articular cartilage, ligament and tendon. Although they are passive structures (no active production of force like muscles), their presence in the human body and functionality is of great importance for the body reactions to various actions. All the human tissues, including active and passive, are interrelated when the body moves. Due to the synergetic relationship of the biological tissues during a movement, an injury that occurs to one of the tissues affects not only the function of this tissue but also the functionality of the whole body structures. The purpose of this chapter is to provide insight into the mechanical aspects of construction and function of the bone, articular cartilage, ligament, and tendon.

3.1 Bone

Bone is the hard part of the connective tissue and constitutes the majority of the skeleton of most vertebrates. It consists of an organic component (the cells and the matrix) and an inorganic or mineral component. The inorganic component of bone makes it hard and relatively rigid, whereas its organic component provides flexibility and resilience. The purpose of the skeletal system is to provide support for the body against external forces (e.g. gravity), provide rigid kinematic links and muscle-tendon attachment sites so as to transfer forces (e.g. muscular forces) and supply protection for internal organs (e.g. the brain). In addition, bone has physiological functions such as to form blood cells (hematopoiesis) and to store calcium (mineral homeostasis). Apart from the 99% of total body calcium, other minerals (phosphorus, sodium, potassium, zinc, magnesium), which are critical for a number of vital metabolic processes, are also stored in the skeleton. Bone has unique structural and mechanical properties that allow it to carry out these functions. It is one of the most dynamic and metabolically active tissues in the body and remains active throughout life. It has an

excellent capacity for self repair and can alter its shape, mechanical behavior and mechanical properties in response to changes in mechanical demand. In the following sections, emphasis is given to the anatomy, structure, and mechanical properties of bone.

3.1.1 Anatomy and structure

The composition of bone depends on a large number of factors: species, age, sex, type of bone, type of bone tissue (e.g. woven, cancellous, cortical), and the presence of a bone disease. In normal human bone, the mineral or inorganic portion of bone consists primarily of calcium and phosphate, mainly in the form of hydroxyapatite crystals with the composition $Ca_{10}\,(PO_4)_6\,(OH)_2$. These minerals account for 60 to 70% of its weight, water accounts for 5 to 8% and organic components including collagen makes up the remainder of the tissue.

At the smallest unit of structure we have the tropocollagen molecule and the associated apatite crystallites (Ap). Tropocollagen is the basic structural unit of all forms of collagen; it is a helical structure of three polypeptide chains (alpha chains) wound around each other (Fig. 3.1).

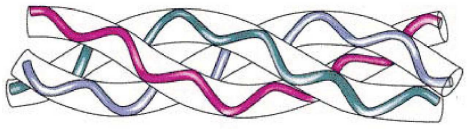

Figure 3.1: A tropocollagen molecule. (From http://resources.schoolscience.co.uk/Unilever/16-18/proteins/Protch5pg1.html)

Ap crystallites have been found to be hydroxyapatite crystals. At the next structural level, collagen and Ap are intimately associated and assembled into a microfibrilar composite, several of which are then assembled into fibers from approximately 3 to 5 μm thick. The next level is associated with the arrangement of the fibers formed previously. These fibers are either randomly arranged (woven bone) or organized into concentric lamellar groups (osteons) or linear lamellar groups (plexiform bone). Finally, we have the whole bone itself constructed of osteons (Fig. 3.2) and portions of older, partially destroyed osteons in the case of humans or of osteons and/or plexiform bone in the case of mammals.

In Fig. 3.3 the anatomy of a long bone is depicted. The *epiphysis* is found at the ends of long bones. The epiphysis articulates with other bones and is protected by a layer of hyaline cartilage referred to as articular cartilage. Between the two parts of epiphysis is the shaft of the long bone, the *diaphysis*. The diaphysis is a hollow structure, surrounding the *medullary cavity*. The medullary cavity is used as a marrow storage site and is lined by a thin, largely cellural connective tissue membrane, the *endosteum*. Surrounding and

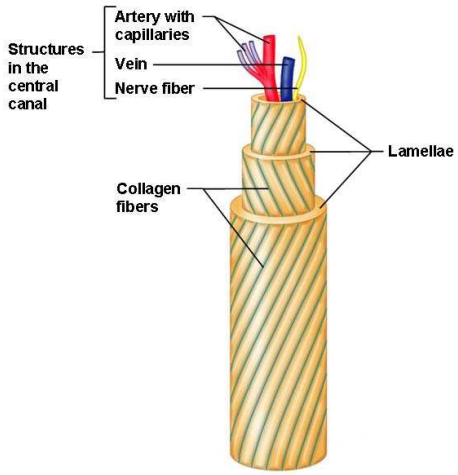

Figure 3.2: Structure of an osteon. (From Marieb and Hoehn, 2007)

attached to the diaphysis is a tough, fibrous tissue called the *periosteum*. The outer layer of the periosteum is well supplied with blood vessels and nerves, some of which enter the bone. The inner layer is bonded to the bone by collagenous bundles called *Sharpey's fibers*, which penetrate the bone.

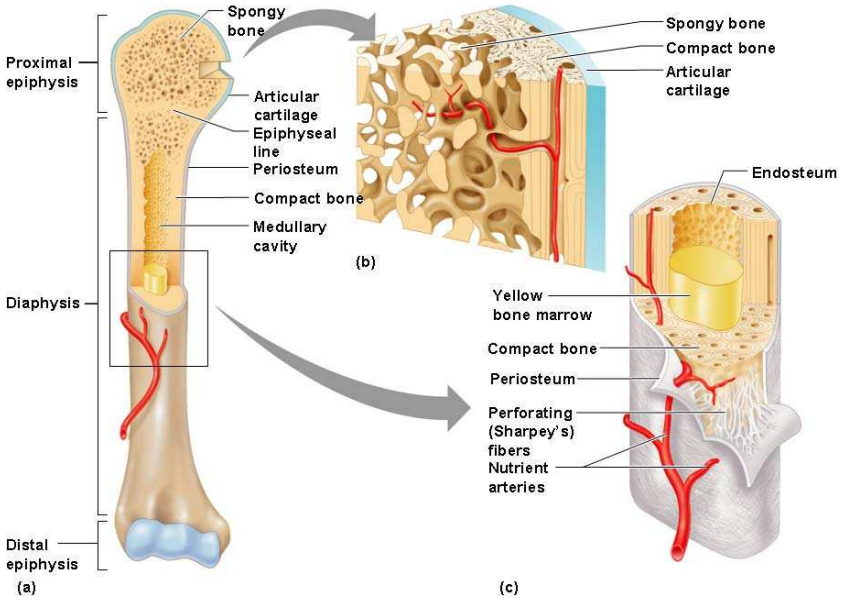

Figure 3.3: Anatomy of a long bone. (From Marieb and Hoehn, 2007)

At the gross level all bones in the adult skeleton have two basic structural components: the **cortical** (or compact) bone and the **cancellous** (or spongy) bone. *Cortical* bone is the solid, dense material comprising the walls of diaphysis and external surfaces of bones. This type of bone is strong and resistant to bending. *Cancellous* bone is formed by a thin bone

structure, called trabeculae. These trabeculae have been observed to orient themselves in the direction of the forces applied to the bone (Wolff's law).

In Fig. 3.4 the microscopic anatomy of a cortical bone is depicted. Compact bone is composed of structures called osteons (Harvesian systems). *Osteon* is a group of concentric tubes that in cross-section appear as rings (Fig. 3.2). They are made up of *lamella*. Circular lamella is called concentric and parallel lamella is called interstitial lamella. Within the lamella is a network of osteocytes embedded in *lacunae* and connected by *canaliculi* (little canals). These cells are maintained alive by nutrients and oxygen provided by blood vessels passing through the center of the osteon called the central or *harvasian canal* and the *volkman's canal* (transverse to diaphysis). Circumferential lamellae follow the circumference of the bone. The trabeculae of spongy bone is also made of lamella and osteocytes but not osteons because the trabeculae are so small.

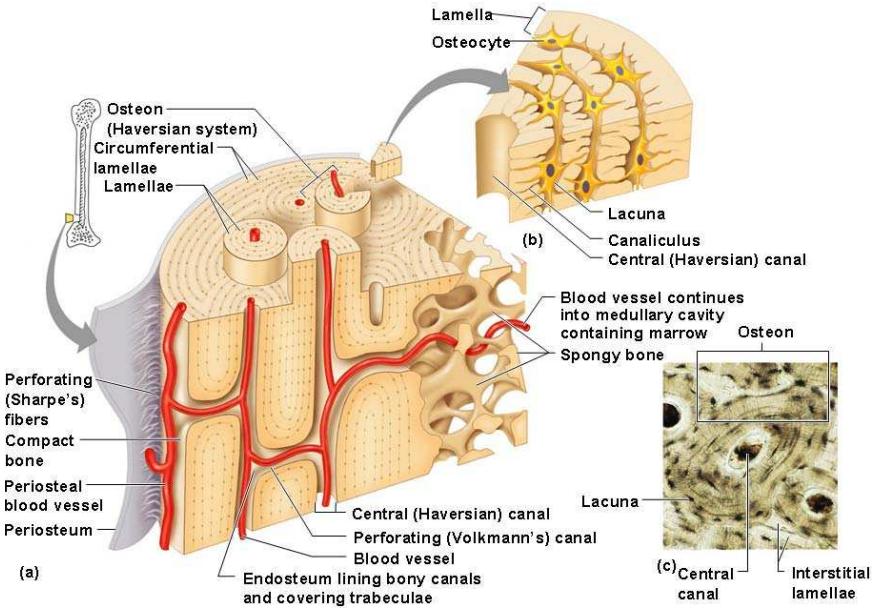

Figure 3.4: Microscopic anatomy of a cortical bone. (From Marieb and Hoehn, 2007)

3.1.2 Physical properties

Bone is a complex structural material. The complexity of bone's properties arises from the complexity in its structure. Thus, the mechanical response of bone can be observed by subjecting it to tension, compression, bending, torsion, and combined loading. Especially combined loading of bone should attract much attention since living bone is seldom loaded in one mode only. All these experiments are essential in order to provide better understanding in factors that cause bone fractures during various body movements.

Bone is a non-homogeneous and anisotropic material. Its mechanical properties change as a function of the specific location in the bone and the direction in which force is applied

(Fig. 3.5).

Loading Mode	*Ultimate Strength*
LONGITUDINAL	
Tension	133 MPa
Compression	193 MPa
Shear	68 MPa
TRANSVERSE	
Tension	51 MPa
Compression	133 MPa
ELASTIC MODULUS	
Longitudinal	17.0 GPa
Transverse	11.5 GPa
SHEAR MODULUS	3.3 GPa

Figure 3.5: Mechanical properties of bone verify its anisotropy.

Stiffness with respect to tension is maximal for axial forces and minimal for transverse forces. Stiffness for axial forces is about twice the magnitude of stiffness for transverse forces (Fig. 3.6). Also, the ultimate strain for bone loaded in the axial direction is about twice the ultimate strain for bone loaded in transverse direction (Fig. 3.6). In addition, bone possesses viscoelastic (time-dependent) material properties, i.e., the mechanical response of bone depends on the rate at which the loads are applied. Bone can resist rapidly applied loads much better than slowly applied loads. Therefore, bone is stiffer and stronger at higher strain rates (Fig. 3.6).

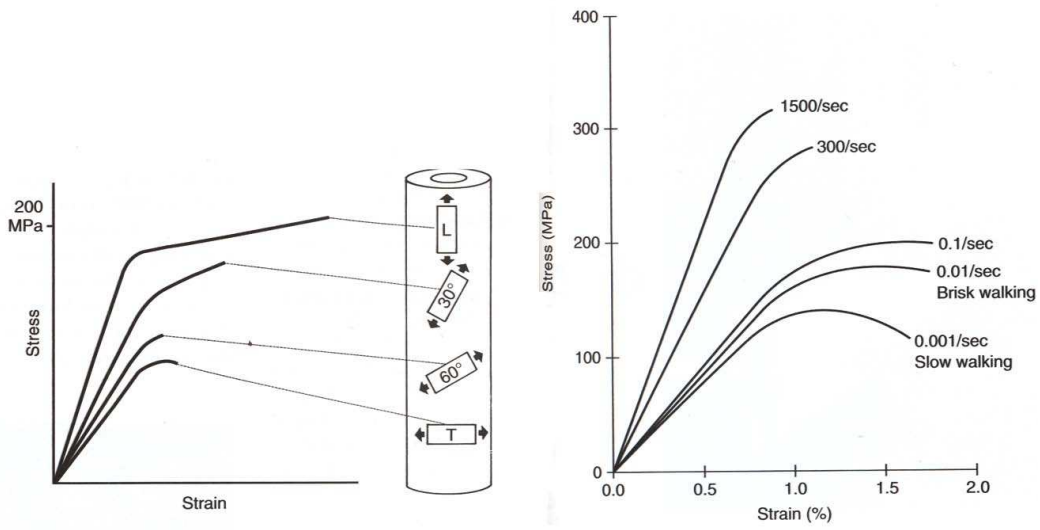

Figure 3.6: Mechanical behavior of bone showing its anisotropy (left). Mechanical behavior of bone showing its viscoelasticity (right). (From Nordin and Frankel, 2001)

In the beginning of section 3.1.1 it was stated that the composition of bone depends on a

large number of factors, such as the species, age, sex, type of bone, type of bone tissue, and the presence of a bone disease. It is obvious that these changes cause relative differences in the mechanical properties of the bone. The main difference in mechanical properties of bone tissue is observed between cortical and cancellous bone. Although the chemical composition of both types is similar, their structure is totally different. Cortical bone is the solid, dense material, whereas cancellous bone is distinguished for its porosity. Typical values for the elastic modulus E are:

- 1 GPa for cancellous (spongy) bone,
- 20 GPa for cortical (compact) bone,
- 100 GPa for metals.

3.2 Articular Cartilage

Articular cartilage is a thin layer of fibrous connective tissue on the articular surfaces of bones in synovial joints (Fig. 3.7).

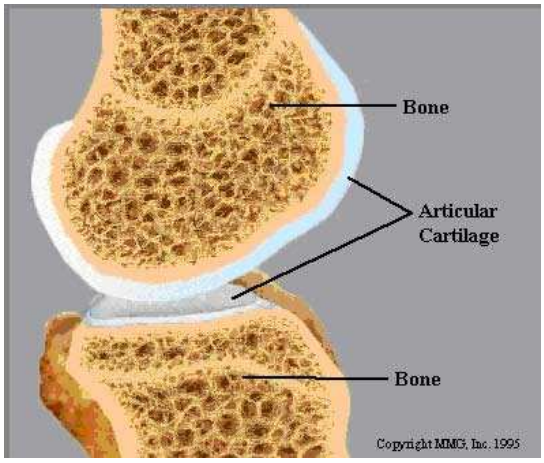

Figure 3.7: Articular cartilage on the surfaces of bone in synovial joints.

Articular cartilage consists of cells ($\sim 5\%$) and an intercellular matrix ($\sim 95\%$), which is substantially water ($\sim 65 - 80\%$). The solid-fluid composition of cartilage makes it a viscoelastic material, which provides an extremely low coefficient of friction (~ 0.0025) to joints. The major functions of articular cartilage include transferring forces between articulating bones, distributing forces in joints, and allowing relative movement between articular surfaces with minimal friction. During daily activities, the articular cartilage is subjected to tensile and shear stresses as well as compressive stresses. Shear stresses are due to the frictional forces between the relative movement of articulating surfaces. However, the coefficient of friction is so low that friction has an insignificant effect on the stress resultants acting

on the cartilage. In the following sections, emphasis is given to the anatomy, structure, and mechanical properties of articular cartilage.

3.2.1 Anatomy and structure

At the smallest unit of structure, articular cartilage consists mostly of matrix and a sparse population of cells. The cells of articular cartilage account for less than 10% of the tissue's volume and are called chondrocytes (Fig. 3.8).

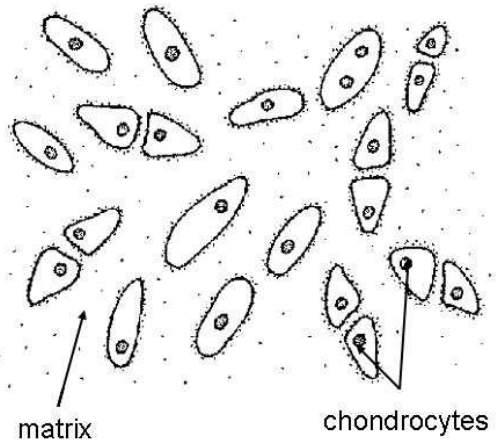

Figure 3.8: Matrix and cells (chondrocytes) compose the microstructure of articular cartilage.

Chondrocytes vary in size, shape, and density according to their location. Despite their sparse distribution, they are highly metabolically active and thus are responsible for the synthesis and degradation of the matrix. They are similar to osteocytes of bone in that they both play an active metabolic role. In articular cartilage, chondrocytes specialize in producing Type II collagen and proteoglycan. The intercellular matrix consists of structural macromolecules and tissue fluid. Tissue fluid comprises $\sim 65-80\%$ of the wet weight of cartilage, while the structural macromolecules comprise $\sim 20-35\%$. The structural macromolecules consist of collagen, proteoglycan, and other proteins. The basic biological unit of collagen is tropocollagen (Fig. 3.1). Although collagen in articular cartilage is the same fibrous protein found in bone, it appears in a slightly different form. Bone collagen is called type I and articular cartilage collagen is called type II. Differences in collagen types lie on differences in tropocollagen alpha chains in various body tissues. Articular cartilage collagen contains three identical alpha chains, where bone collagen has two identical and one different. On the other hand, proteoglycans are a group of glycoproteins formed of subunits of disaccharides linked together and joined to a protein core. Proteoglycans are found in relatively large portions in articular cartilage ($\sim 10\%$). Tissue fluid, the main constituent of articular cartilage, contains mostly water and is found in the form of a viscous gel along with the structural macromolecules. The vast majority of the tissue fluid is free to move both

inside and outside of the cartilage body. It is, therefore, closely associated with the synovial fluid of the joint and with joint lubrication. Also, it is closely associated with proteoglycans which attempt to restrain its movement. The combination of the proteoglycans and the collagen framework makes cartilage sponge-like. The pores of cartilage, from which the water can escape, are small (2.5 to 6.5 nm).

Articular cartilage is structural inhomogeneous. It changes with depth from the joint surface. The inhomogeneous composition and structural framework of articular cartilage result in a highly anisotropic material. The constitutive changes are continuous but may be divided into four zones (Fig. 3.9):

- superficial zone,
- transitional zone,
- deep zone,
- calcified zone.

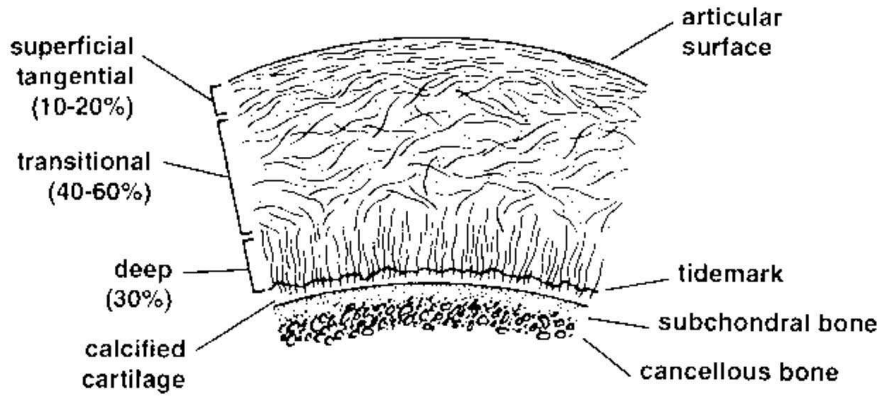

Figure 3.9: The structural changes of articular cartilage related to the depth from the joint surface. (From Nigg and Herzog, 1999)

The *superficial zone* is the thinnest, most superficial region of articular cartilage. It has a surface layer and a deeper layer. The surface layer is approximately 2 μm thick and consists of random flat bundles of collagen fibrils. The deeper layer consists of dense collagen fibers lying parallel to the plane of the joint surface. It also contains elongated chondrocytes, whose long axes lie parallel to the joint surface. Of all the zones of articular cartilage, the superficial zone has the highest concentration of water, approximately 80%. Water concentration decreases in a nearly linear manner with increasing depth until it reaches 65% in the deep zone.

The *transitional zone* consists of collagen fibrils with larger diameter than those in the superficial zone. These fibrils mostly lie parallel to the plane of joint motion, but they are

less parallel than those in the superficial zone. The chondrocytes in this region are spherical. Also it is found that the cells in the transitional zone play a great role in matrix synthesis.

The *deep zone* contains large numbers of big collagen bundles directed perpendicular to the plane of joint motion. Water content is relatively low in this zone. The chondrocytes are round and stacked on the top of each other in a column perpendicular to the joint surface. Also it is found that much protein synthesis occurs in the deep zone.

The *calcified zone* marks the transition from soft articular cartilage to stiffer subchondral bone. It is separated from the deep zone by the "tidemark", an undulating line 2-5 μm thick. The collagen fibers from the deep zone tie the cartilage to the bone by fixing themselves into the subchondral bone.

3.2.2 Physical properties

In cartilage, collagen and proteoglycan are dispersed in the fluid. These substances, which are produced by the chondrocytes, interact to produce the fluid and solid mechanical behavior associated with articular cartilage. The specific characteristics of the physical, chemical, and mechanical interactions, between collagen and proteoglycan have not yet been fully determined. Nevertheless, it is known that these structural macromolecules interact to form a porous-permeable fiber-reinforced composite matrix possessing all the essential mechanical characteristics of a solid that is swollen with water and that is able to resist the high stresses and strains of joint articulation.

Collagen accounts for much of the structural framework of cartilage and gives much of its tensile stiffness and strength. The tensile strength of individual collagen fibers is not yet known, but tendon, of which collagen comprises the 80% of the dry weight, has a tensile strength of about 70 MPa. Its tensile strength is comparable to that of nylon (80 MPa) and pure aluminium (70 MPa). However, collagen fibers, due to their large ratio of length to thickness, appear to buckle easily in compressive loads and thus offer little resistance to compression or shear. A typical tensile stress-strain curve for articular cartilage is shown in Figure 3.10. The configuration of the collagen fibers changes at various stages of loading. Initially, fibers are partially relaxed and wavy in appearance. In the toe region, collagen fibers straighten and become aligned in the direction of the tensile load. In the linear region, the aligned collagen fibers are stretched until failure occurs. At physiological strain levels (up to 15%), Young's modulus of articular cartilage ranges between 1 and 10 MPa.

On a molecular level, cross-links between collagen fibrils exist. These cross-links may further increase tensile strength, stiffness, and integrity. So, collagen fibers and fibrils in articular cartilage are not only strong individually but, being bonded with their own molecules and other structural macromolecules, also contribute to a rise of stiffness. Like bone, articular cartilage is anisotropic: its material properties differ with the direction of loading. It

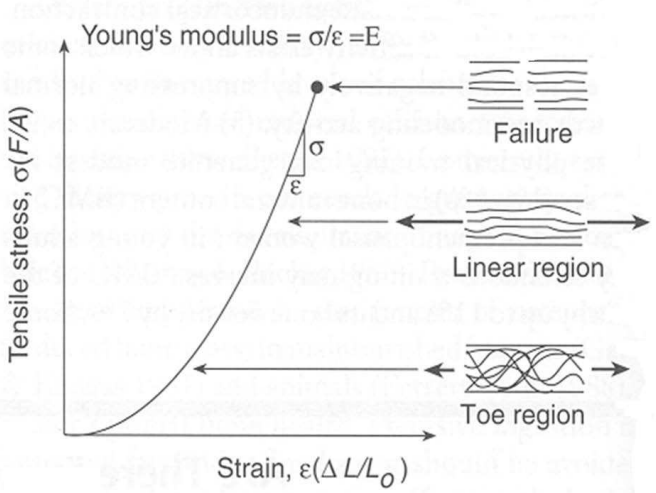

Figure 3.10: A typical stress-strain curve for articular cartilage accompanied by the configuration of the collagen fibers in each stage of loading.

is thought that this anisotropy is related to the varying collagen fiber arrangements within the planes parallel to the articular surface. It is also thought that variations in collagen fiber density, as well as variations in collagen-proteoglycan interactions within the matrix, also contribute to articular cartilage tensile anisotropy. The tensile modulus decreases with increasing depth from the cartilage surface because the orientation of the collagen fibers of the deeper layers is rather random compared to the parallel uniformity at the surface and also because the collagen density decreases with depth from the articular surface (Fig. 3.11).

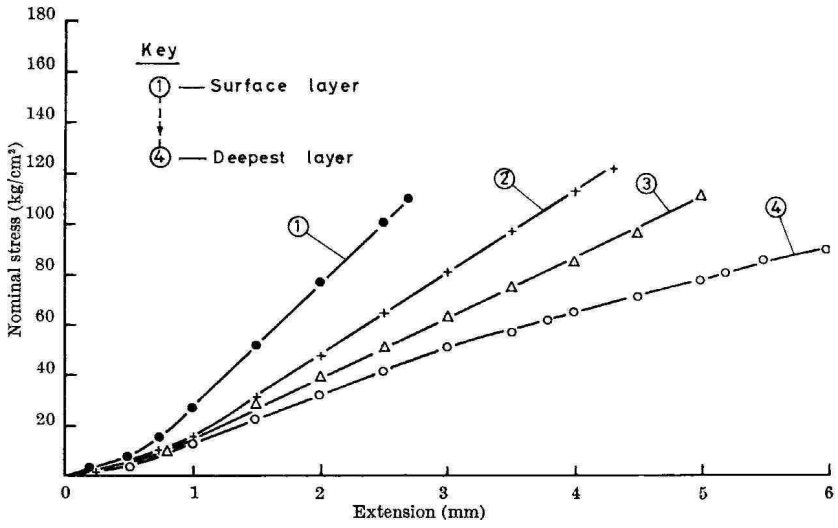

Figure 3.11: Variations in tensile stress behavior with depth in articular cartilage. (From Kempson *et al.*, 1968)

In addition, cartilage shows differences in tensile strength when tested parallel to the

collagen fiber direction and perpendicular to it (Fig. 3.12). The collagen-proteoglycan interactions within the matrix are, also, responsible for the shear properties of articular cartilage. The magnitude of frictional shear stress due to motion of one bone relative to another is usually ignored because the coefficient of friction is small. However, the shear stress is not negligible. The intersurface frictional shear is initially carried in the superficial zone as a tensile stress. This stress may be transmitted down to the subchondral bone as shear through the matrix or/and through tensing the angled collagen fibers in the middle and deeper zones of the cartilage layer.

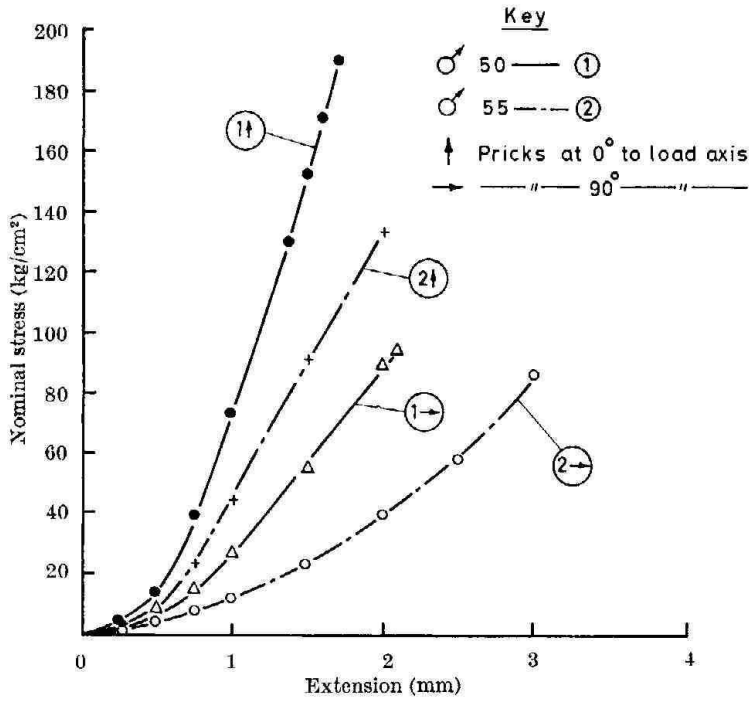

Figure 3.12: Variations in tensile strength of articular cartilage when tested in different collagen fiber directions. (From Kempson *et al.*, 1968)

On the other hand, proteoglycans, because of their molecular structure, are ideally suited to resisting compressive forces, which is why more proteoglycans are found in articular cartilage than in the other soft tissues. Compressive properties vary with the zone tested and are related to proteoglycan concentration. When proteoglycan content increases so does the tissue's compressive stiffness.

Cartilage is a microporous material with low permeability. Permeability represents the frictional resistance of a porous material to fluid flow in such a way that, the more permeable the material, the less the resistance to flow. In the case of articular cartilage, its low permeability inhibits any rapid escape of fluid when the cartilage is compressed, as it is during joint movement. The permeability of healthy articular cartilage is relatively low (very much lower than that of a sponge) and decreases as the cartilage is compressed. Thus, it is

harder to remove fluid from the matrix when compression increases. This is important for nutrition of the cartilage and for its resistance to wear. If the cartilage becomes damaged, the permeability of the cartilage becomes greater, perhaps because the collagen fibers are broken, allowing the proteoglycan molecules to be washed out of the matrix, resulting in further deterioration of the cartilage.

Cartilage is a viscoelastic material. Viscoelasticity may be revealed through creep or stress relaxation. The viscoelastic properties of articular cartilage are mainly associated with the movement of water in the tissue. Because of the low permeability of cartilage, its mechanical behavior depends on the rate at which a load is applied or removed. When the tissue is loaded slowly or a constant load is maintained (as in standing), the cartilage will continue to deform as fluid is squeezed out until equilibrium is reached. However, when the tissue is loaded very rapidly (as in jumping), there is no time for fluid to be squeezed out, and the cartilage behaves like an elastic solid.

Under normal conditions, cartilage wears at a very low rate, suggesting that lubrication is efficient, and the surfaces are normally held apart by a fluid film and do not contact one another. Once surface damage occurs, even in a localized region, the whole surface becomes less stiff and more permeable, proteoglycans are lost, and the fluid film leaks away more easily. All these factors will result in more stress on the cartilage and on the bone underneath, resulting in further damage. Once stresses at the joint become high (perhaps due to fracture) or the cartilage is damaged, further deterioration results, leading to the condition known as osteoarthritis (articulating bones in contact). *Unfortunately, cartilage, in contrast to bone, has a very limited ability to remodel itself when damaged.*

3.3 Ligament

Ligament is a short band of tough fibrous dense regular connective tissue composed of elastin and collagen fibers (Fig. 3.13).

Although ligaments are passive structures (they do not actively produce motion as the muscles do), they play an essential role in joint motion. The major functions of ligaments are: to attach articulating bones to one another across a joint, to guide joint movement, to maintain the stability of the joint, and to prevent excessive motion. Ligament injuries and derangements are common in everyday human activity. Proper management of these disorders requires an understanding of the mechanical properties and function of ligaments. In the following sections, emphasis is given to the anatomy, structure, and mechanical properties of ligaments.

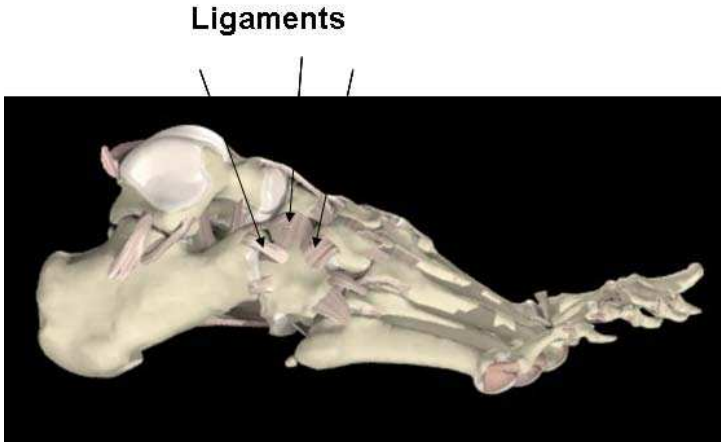

Figure 3.13: Ligaments of the human foot. (From Primal Pictures: "Interactive Foot and Ankle")

3.3.1 Anatomy and structure

Ligaments consist of relatively few cells (fibroblasts) and an abundant extracellular matrix. In general, the cellular material occupies approximately 20% of the total tissue volume, whereas the extracellular matrix accounts for the remaining 80%. Approximately 70% of the matrix consists of water and approximately 30% of solids. These solids are collagen, proteoglycans, fibronectin, elastin, actin, and a few other glycoproteins. The collagen content is generally over 75% of the dry weight of ligament.

Fibroblasts are not homogeneous in ligament tissue and vary in size, shape, orientation, and number. They are generally oriented longitudinally along the length of the ligament body. Fibroblasts are responsible for synthesizing and degrading the ligament matrix in response to various stimuli. It is believed that they prevent or repair ongoing microscopic damage. Therefore, fibroblasts are crucial to maintaining the integrity of ligaments.

On the other hand, water makes up approximately 70% of the matrix. Water can be associated with other ligament components in a variety of ways. The function of water in ligaments appears to be crucial for at least three main reasons. First, its interaction with the ground substance and particularly the proteoglycans influences the tissue's viscoelastic behavior. Second, it seems to provide lubrication and facilitate inter-fascicular sliding. Third, it carries nutrients to the fibroblasts and takes waste substances away.

Also, matrix consists of approximately 30% of solids. Collagen is the main protein present in ligaments. It is found mainly in fibrillar form, oriented between insertion points on the bones such that it will resist tensile forces. Collagen fibers within ligaments vary in size (diameter) from 10-1500 nm, a range that appears to depend on age, type of ligament, and species. Fiber size may affect the strength of the material. Ligaments with larger collagen distributions tend to be stronger and able to sustain higher stresses. Collagen is enormously strong due to a combination of biochemical bonds known as molecular cross-links.

The hierarchical structure of the collagen in the ligament includes fibers, fibrils, subfibrils, microfibrils, and tropocollagen (Fig. 3.14). Tropocollagen molecules, approximately 1.5 nm in diameter, aggregate into groups of five, becoming microfibrils of approximately 3.5 nm in diameter. The microfibrils group into subfibrils, which, in turn, aggregate to form fibrils. Fibrils are approximately 50-500 nm in diameter with a periodicity of 64 nm. Fibers are an aggregation of fibrils and are 50-300 μm in diameter. They appear with crimps.

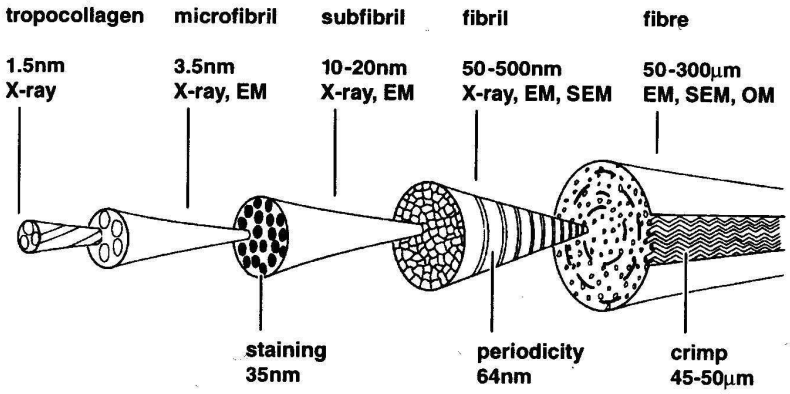

Figure 3.14: Structural hierarchy of collagen in the ligament. (From Nigg and Herzog, 1999)

In addition, elastin is an elastic substance that is found in very small amounts in most skeletal ligaments (approximately 1.5%) in fibrillar form. Its fibrillar form probably is responsible for a part of the tensile resistance in ligament tissue and some of its elastic recoverability. The role of elastin is probably related to recovering ligament length after stress is removed. Elastin probably protects collagen, at least at low strains.

3.3.2 Physical properties

Ligaments are pliant and flexible allowing natural movements of the bones to which they attach, but also they are strong and inextensible so as to offer suitable resistance to applied forces.

A typical force-deformation curve for ligaments is shown in Figure 3.15. The stiffness of ligaments varies non-linearly with force. This non-linear behavior allows ligaments to permit initial joint deformations with minimal resistance. At higher forces, ligaments become stiffer, providing more resistance to increasing deformations, and, as a result, protection to the joint.

The first region of the load-deformation curve is called the “toe” region. The deformation reflected in this region is believed to be the result of two reasons: a change in the wavy pattern of the relaxed collagen fibers and the existence of some fibers crossing between parallel fibers in the ligament substance, some running perpendicular to the long axis and some running at every angle to the long axis. In the first region, the tissue stretches easily, without much force, and the collagen fibers become straight and lose their wavy appearance as the loading

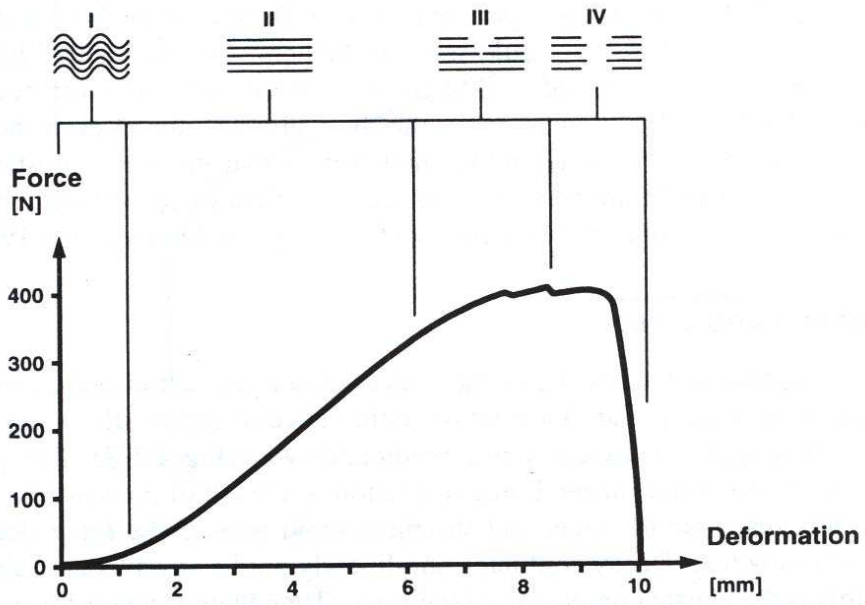

Figure 3.15: A typical force-deformation curve for ligaments accompanied by the configuration of the collagen fibers in each stage of loading. (From Nigg and Herzog, 1999)

progresses. As loading continues, the stiffness of the tissue increases and a progressively greater force is required to produce equivalent amounts of deformation. If deformation is increased (deformation values 2-6 mm) and the collagen fibers take up force, a linear region will follow the toe region. This region corresponds to the second region in the curve of Figure 3.15. Following the linear region, at large deformations the curve can end abruptly or change shape as a result of irreversible changes (failure). When the linear region is surpassed, major failure of fiber bundles occurs in an unpredictable manner till the attainment of the maximum load, where complete failure occurs rapidly.

Ligaments, also, exhibit viscoelastic behavior under loading; their mechanical properties change with different rates of loading. With higher strain rates, ligaments in isolation store more energy, require more force to rupture, and undergo greater elongation. Water is known to contribute to the nonlinear viscoelastic behavior of the ligament in a significant way. Viscoelasticity is mainly revealed through creep (Fig. 3.16) (increase in deformation over time under a constant load) or stress relaxation (Fig. 3.17) (decrease in force over time under a constant deformation).

The mechanical properties of ligaments are affected considerably by factors such as, species, type of ligament, gender, age, activity, drugs, and diet. Values in the range of 10 to 300 MPa have been reported in the literature for the Young's modulus of different ligaments.

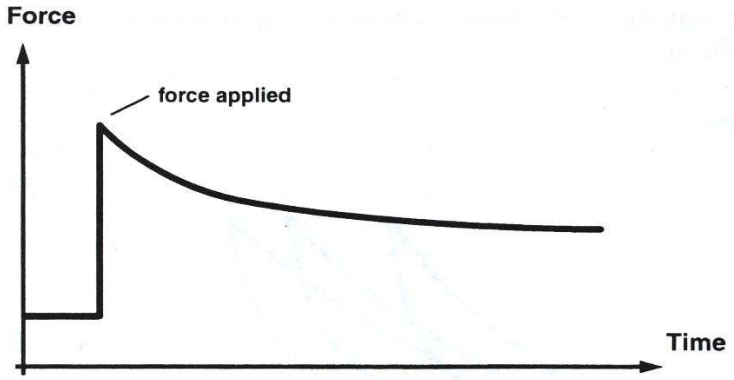

Figure 3.16: A typical creep behavior in ligaments. (From Nigg and Herzog, 1999)

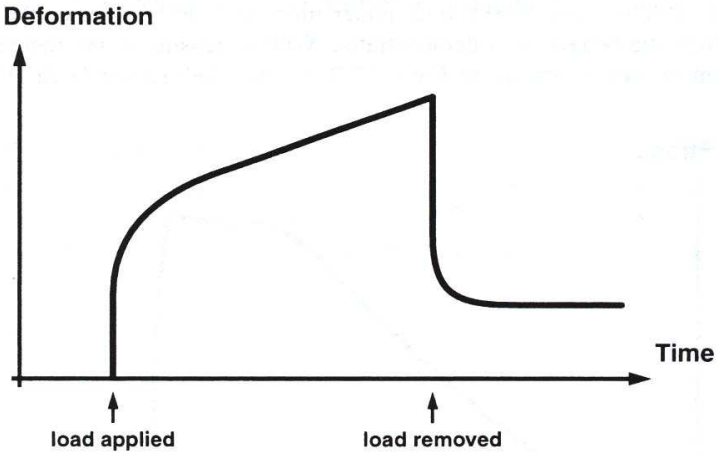

Figure 3.17: A typical stress relaxation behavior in ligaments. (From Nigg and Herzog, 1999)

3.4 Tendon

Tendon is a dense fibrous tissue that connects muscle to bone. It is present in a wide variety of shapes and sizes, depending on the morphological, physiological and mechanical characteristics of both the muscle and bone to which it is attached.

Usually, tendon consists of an external tendon which is typically referred to as **tendon**, and an internal tendon, which is typically referred to as **aponeurosis** (Fig. 3.18). The external tendon connects the muscle to bone and the aponeurosis provides the attachment area for the muscle fibers.

Like ligament, tendon injuries and derangements are common in everyday human activity. In order to deal with these situations, an understanding of the mechanical properties and function of tendons is required. In the following sections, emphasis is given to the anatomy, structure, and mechanical properties of tendons.

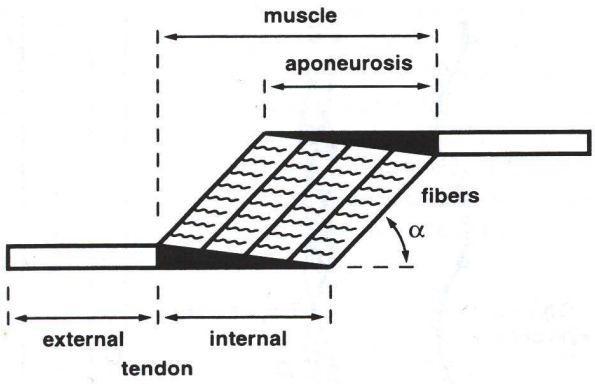

Figure 3.18: Relation among muscle fibers and tendon in a pennated muscle. (From Nigg and Herzog, 1999)

3.4.1 Anatomy and structure

The structure and chemical composition of tendons and ligaments are identical. The main difference between tendon and ligament is that the collagen content is somewhat greater in tendons than in ligaments. Collagen is the main protein present in tendons.

The hierarchical structure of the collagen in the tendon is shown in Figure 3.19.

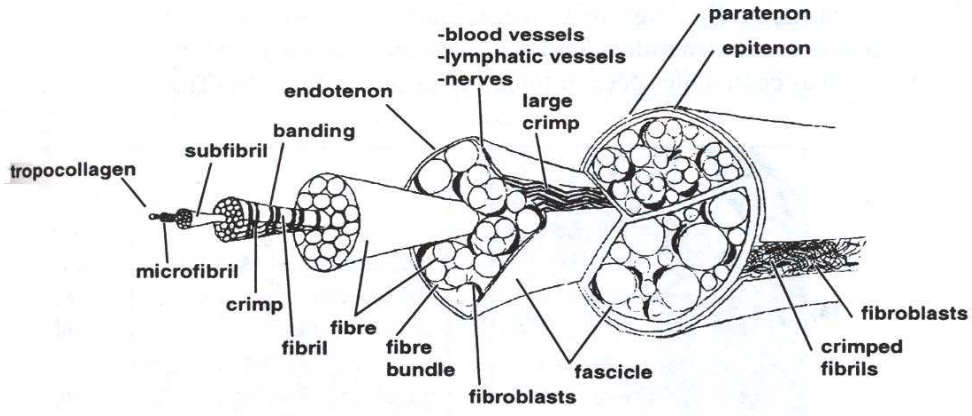

Figure 3.19: Structural hierarchy of tendon, from the tropocollagen molecule to the entire tendon. (From Nigg and Herzog, 1999)

The basic unit of collagen is tropocollagen. Tropocollagen molecules aggregate into groups of five becoming microfibrils. Microfibrils aggregate to form subfibrils, which aggregate further to form fibrils. Fibrils aggregate to form fibers and fiber bundles in which crimping or longitudinal waviness of the collagen fibers may first be apparent. Fiber bundles aggregate to form fascicles. Fascicles are surrounded by endotenon, a connective tissue sheath composed of a well-ordered criss-cross pattern of collagen fibrils, proteoglycans and elastin. The endotenon contains the blood and lymphatic vessels as well as the nerves for the tendon. Fascicles aggregate into fascicle bundles and are surrounded by epitenon. Finally,

several fascicular bundles are surrounded by paratenon, the outermost tendon sheath.

3.4.2 Physical properties

The primary role of tendon is to transmit the force of its associated muscle to bone. As such, tendon needs to be relatively stiff and strong in tension. A typical stress-strain curve for tendon is shown in Figure 3.20. The curve illustrates the response for a tendon specimen subjected to a uniaxial tension test. There are three distinct regions of the curve: toe, linear, and yield regions.

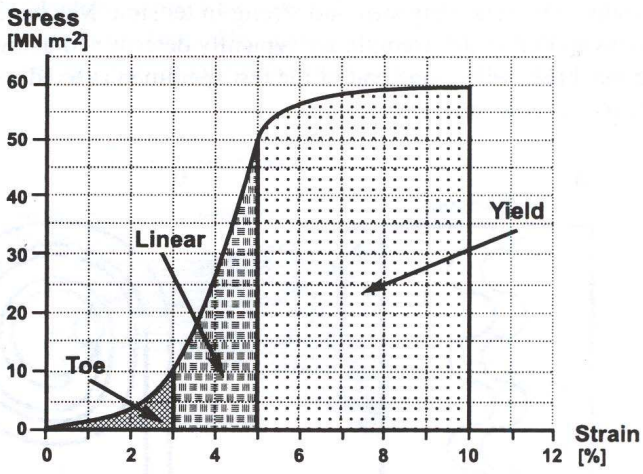

Figure 3.20: A typical stress-strain curve for a tendon specimen subjected to a uniaxial tension test. (From Nigg and Herzog, 1999)

The toe region typically lies below 3% strain. In this region, elongation is accompanied by very low stress. This low initial stiffness of tendon in the toe region is thought to be caused by the straightening of the collagen crimp or by shearing action between the collagen fibrils and the ground substance of the tendon.

The linear region is beyond approximately 2 to 3% tensile strain and it extends to about 4 to 5%. The slope of this linear portion of the curve has been used to define the Young's modulus of the tendon. It is found to take values in the range 1-1.5 GPa.

Beyond the linear region permanent deformation occurs. The ultimate or failure strain of tendon is about 8 to 10%. In the yield region the deformation of tendon is accompanied by very little increase in stress. Tendon failure eventually results from the fracture of the collagen fibers. A mean value of the ultimate stress in tendon is 100 MPa. The high tensile stiffness and strength of tendon is attributed to its relatively high collagen content and to its hierarchical organization into linear bundles.

Like ligaments, tendons also exhibit viscoelastic behavior. Viscoelasticity is mainly revealed through creep or stress relaxation. However, it is proved that about 89 to 94% of

the energy associated with longitudinal deformation or stretch of a tendon is recovered when the load on the tendon is removed. Thus, for a biological material, tendon shows marked elastic behavior, at least within the likely range of physiologically relevant frequencies of deformation.

Chapter 4

Continuum constitutive modeling of muscle and tendon

In this chapter a continuum constitutive model that describes the biomechanical behavior of muscle and tendon is presented. The model is based on an idea put forth recently by Liang *et al.* (2006) for the mechanical behavior of muscular hydrostats.

Muscle and tendon are both reinforced with fibers. The most basic characteristic of muscle is its ability to produce force; its capability of active contraction makes it distinct from other soft biological tissues. On the other hand, tendon is a passive material; its primary role is to transmit the force of its associated muscle to bone.

In the following, all materials are considered as "continuous media" and the modeling follows the general principles of "Continuum Mechanics". From the Mechanics viewpoint, the muscle is a "composite" material that consists of the fibers, the connective tissues, and the biofluids surrounding the muscle fibers. The constitutive model developed in the following is essentially a "homogenization" process that accounts for the presence of the fibers and the other material "phases".

4.1 Constitutive model

4.1.1 Basic structure of the constitutive model

As discussed in section 2.1, the structural unit of skeletal muscle is the muscle fiber. The muscle fiber is composed of parallel bundles of myofibrils. Each myofibril is in turn divided longitudinally by the Z-discs into sarcomeres, which are the basic contractile units of a muscle. Sarcomeres, also, are responsible for the passive properties of the muscle. Thus, the active and passive behavior of the muscle is produced within the muscle fiber. Additionally, in section 3.4.1 of chapter 3 is described in detail that the structural unit of tendon is the collagen fiber.

In the present model, muscle and tendon are considered as non-linear and anisotropic due to the existence of fibers in their mass. The tissue (muscle, tendon) is "homogenized"

and the anisotropy is defined locally in terms of the local fiber direction as described in the following.

At every material point in the tissue, we define the local direction of the *deformed* fiber by the corresponding unit vector $\boldsymbol{m}$ (Fig. 4.1).

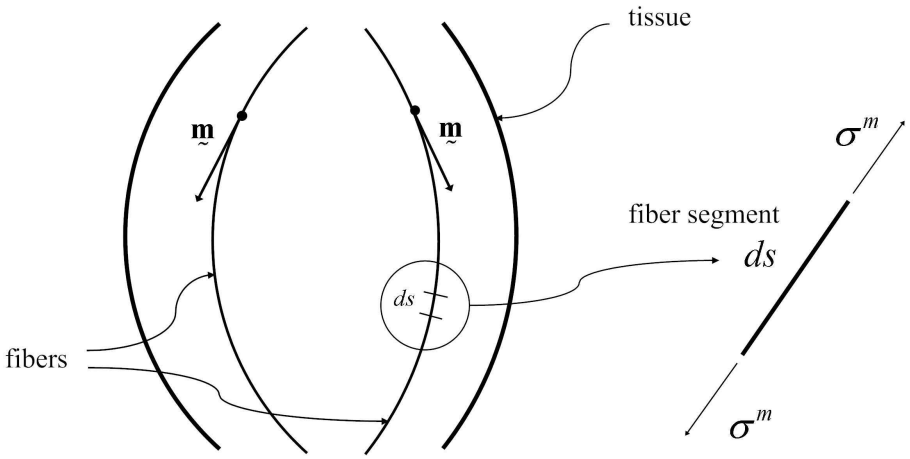

Figure 4.1: Tissue fiber in the deformed configuration with its direction defined locally by unit vector $\boldsymbol{m}$. Also shown the fiber stress σ_m acting on an infinitesimal fiber segment of length ds.

Let $\mathbf{F}$ be the value of the deformation gradient at a material point. Then $\boldsymbol{m}$ can be determined from

$$\boldsymbol{m} = \frac{1}{|\boldsymbol{F} \cdot \boldsymbol{m}_0|} \boldsymbol{F} \cdot \boldsymbol{m}_0, \tag{4.1}$$

where $\boldsymbol{m}_0$ is the unit vector that defines the orientation of the fiber in the undeformed configuration.

We consider the Eulerian logarithmic strain tensor:

$$\boldsymbol{\varepsilon} = \ln \boldsymbol{V}, \tag{4.2}$$

where $\mathbf{V} = \sqrt{\mathbf{F} \cdot \mathbf{F}^{\mathbf{T}}}$. Part of the strain is associated locally with the volume preserving axial local deformation in the direction $\boldsymbol{m}$ of the fiber $\boldsymbol{\varepsilon}^f$. The change of length of an infinitesimal fiber segment of original length ds_0 can be determined in terms of the corresponding stretch ratio λ_m:

$$\lambda_m = \frac{ds}{ds_0} = \sqrt{\boldsymbol{m}_0 \cdot \boldsymbol{F}^T \cdot \boldsymbol{F} \cdot \boldsymbol{m}_0}, \tag{4.3}$$

where ds is the length of the infinitesimal fiber segment after the deformation. The associated axial logarithmic strain in the fiber direction is ε_m:

$$\varepsilon_m = \ln \lambda_m. \tag{4.4}$$

The corresponding volume preserving logarithmic fiber strain tensor can be written as[1]

$$\boldsymbol{\varepsilon}^f = \frac{3}{2} \varepsilon_m \left(\boldsymbol{m}\,\boldsymbol{m} - \frac{1}{3}\boldsymbol{\delta} \right), \tag{4.5}$$

[1] Let $\mathbf{e}_1$ and $\mathbf{e}_2$ be unit vectors such that $(\mathbf{e}_1, \mathbf{e}_2, \boldsymbol{m})$ form a right-handed orthonormal basis. Then

where $\boldsymbol{\delta}$ the second-order identity tensor.

It can be shown that the rate of change of ε_m can be determined as

$$\dot{\varepsilon}_m = \frac{\dot{\lambda}_m}{\lambda_m} = \boldsymbol{m} \cdot \boldsymbol{D} \cdot \boldsymbol{m} = (\boldsymbol{m}\,\boldsymbol{m}) : \boldsymbol{D}, \tag{4.6}$$

where $\boldsymbol{D}$ is the deformation rate tensor defined as the symmetric part of the spatial velocity gradient in the deformed configuration[2].

The difference between the total strain $\boldsymbol{\varepsilon}$ and the fiber strain $\boldsymbol{\varepsilon}^f$ is associated with the connective tissue and the biofluids surrounding the fibers:

$$\boldsymbol{\varepsilon}^{ct} = \boldsymbol{\varepsilon} - \boldsymbol{\varepsilon}^f. \tag{4.7}$$

In particular, $\boldsymbol{\varepsilon}^{ct}$ represents the extent to which the total strain is locally not axisymmetric with respect to the fiber and is not volume preserving, i.e., it represents any area change transverse to the fiber due to a local volume change in the "composite" material and any local transverse and axial shear relative to the fiber.

If (4.5) were the only strain in the tissue, then the corresponding true stress tensor would be of the form (Fig. 4.1)

$$\boldsymbol{\sigma}^f = \sigma^m\, \boldsymbol{m}\,\boldsymbol{m}, \tag{4.8}$$

where σ^m is the true stress in the fiber direction and depends on the fiber strain and strain rate as described in the following. In the general case, additional stresses $\boldsymbol{\sigma}^{ct}$ develop due to the deformation $\boldsymbol{\varepsilon}^{ct}$ of the connective tissues and the biofluids.

As a first approximation, we assume that the total true stress $\boldsymbol{\sigma}$ in the tissue can be written as the sum of $\boldsymbol{\sigma}^f$ and $\boldsymbol{\sigma}^{ct}$:

$$\boldsymbol{\sigma} = \boldsymbol{\sigma}^f + \boldsymbol{\sigma}^{ct}, \tag{4.9}$$

where $\boldsymbol{\sigma}^f$ and $\boldsymbol{\sigma}^{ct}$ depend on the deformation of the tissue as described in the following.

4.1.2 Constitutive description of σ^m

The nominal strain in the fiber is defined as

$$\varepsilon_0^m = \frac{ds - ds_0}{ds_0} = \lambda_m - 1 = \exp(\varepsilon_m) - 1 \qquad \text{or} \qquad \varepsilon_m = \ln(1 + \varepsilon_0^m). \tag{4.10}$$

$\mathbf{e}_1\,\mathbf{e}_1 + \mathbf{e}_2\,\mathbf{e}_2 + \boldsymbol{m}\,\boldsymbol{m} = \boldsymbol{\delta}$, and the logarithmic strain tensor that describes the volume preserving axial deformation in the direction $\boldsymbol{m}$ can be written as

$$\boldsymbol{\varepsilon}^f = \varepsilon_m\, \boldsymbol{m}\,\boldsymbol{m} - \frac{\varepsilon_m}{2}(\mathbf{e}_1\,\mathbf{e}_1 + \mathbf{e}_2\,\mathbf{e}_2) = \varepsilon_m\, \boldsymbol{m}\,\boldsymbol{m} - \frac{\varepsilon_m}{2}(\boldsymbol{\delta} - \boldsymbol{m}\,\boldsymbol{m}) = \frac{3}{2}\,\varepsilon_m(\boldsymbol{m}\,\boldsymbol{m} - \frac{1}{3}\boldsymbol{\delta}).$$

[2] This leads to the more involved formula for the evaluation of ε_m, which is used sometimes incrementally in computational mechanics: $d\varepsilon_m = \boldsymbol{m} \cdot \boldsymbol{D} \cdot \boldsymbol{m}\; dt$ or $\varepsilon_m(t) = \int_0^t \boldsymbol{m}(\tau) \cdot \boldsymbol{D}(\tau) \cdot \boldsymbol{m}(\tau)\; d\tau$, where t denotes time.

The nominal axial stress σ_0^m in the fiber is defined in terms of the true fiber stress σ_m as follows:

$$\sigma_0^m = \sigma^m \frac{A}{A_0} = \sigma^m \frac{ds_0}{ds} = \frac{\sigma^m}{\lambda_m} = \frac{\sigma^m}{1+\varepsilon_0^m}, \tag{4.11}$$

where A and A_0 denote the current and reference cross-sectional area of the fiber respectively.

4.1.3 The fiber part of muscle

The total nominal longitudinal stress in a muscle fiber is, in general, a function of time t, nominal longitudinal strain, and nominal longitudinal strain rate:

$$\sigma_0^m = f\left(\varepsilon_0^m, \dot{\varepsilon}_0^m, t\right). \tag{4.12}$$

The force exerted by a muscle fiber has "active" and "passive" characteristics. The "active" part of the force depends on the activation level, fiber length, and velocity of contraction of the muscle fiber, whereas the "passive" part depends only on the length of muscle fiber. In the present approach the relation used for the nominal longitudinal stress in a muscle fiber is written as the sum of an active and a passive part:

$$\sigma_0^m = \sigma_0^{m(act)} + \sigma_0^{m(pas)}, \tag{4.13}$$

where $\sigma_0^{m(act)}$ and $\sigma_0^{m(pas)}$ denote the "active" and "passive" part of the nominal longitudinal stress respectively.

For the active stress it is known that

- the level of activation affects the magnitude of the generated force (Fig. 2.13),
- the force-length relationship is coupled to the level of activation (Fig. 2.10),
- the force-velocity relationship could also be used for lengths other than those corresponding to optimal fiber length (Fig. 2.12).

The coupling between fiber activation and nominal strain in the force-length relationship is incorporated into the model in the form of equation (4.14) below, which is due to Buchanan *et al.*, 2004, and accounts for the coupling between activation and optimal fiber length:

$$\ell_{0a}^m\left(f_a\right) = \ell_0^m\left\{k\left[1 - f_a\left(t\right)\right] + 1\right\}, \tag{4.14}$$

where ℓ_0^m is the optimal fiber length, $f_a\left(t\right)$ is the activation, and k is the percentage change in optimal fiber length. From equation (4.14) we extract the relationship between activation and stretch ratio:

$$\lambda_{0a}^m\left(f_a\right) = \lambda_0^m\left\{k\left[1 - f_a\left(t\right)\right] + 1\right\}, \tag{4.15}$$

where λ_0^m is the optimal fiber stretch ratio. Finally, from equation (4.15) we determine the relationship between activation and nominal strain used in the current muscle model:

$$\varepsilon_{0a}^m\left(f_a\right) = \left(\varepsilon_0^m + 1\right)\left\{k\left[1 - f_a\left(t\right)\right] + 1\right\} - 1. \tag{4.16}$$

Following Van Leeuwen and Kier (1997), we write

$$\sigma_0^{m(act)} = f_a(t)\, f_e(\varepsilon_{0a}^m\left(f_a\right))\, f_r(\dot{\varepsilon}_0^m) \qquad \text{and} \qquad \sigma_{pas}^m = \sigma_{pas}^m(\varepsilon_{0a}^m\left(f_a\right)), \tag{4.17}$$

where f_a is the activation state which describes the pattern of the activation signal as a function of time t, f_e describes the dependence of the active stress on the activation-dependent nominal longitudinal strain ε_{0a}^m, and f_r is the function that relates the active muscle stress to the nominal longitudinal strain rate $\dot{\varepsilon}_0^m$.

It is noted that in the original model of Van Leeuwen and Kier (1997) the active stress-strain function f_e is independent on the activation state, whereas in our approach the same function depends explicitly on activation state as well, based on experimental findings shown in Fig. 2.10.

It is convenient to normalize the above equations and write

$$\sigma_0^m = \sigma_{\max}\left[\sigma_0^{m(act)} + \sigma_0^{m(pas)}\right] \tag{4.18}$$

or

$$\sigma_0^m = \sigma_{\max}\left[f_a(t)\, f_e(\varepsilon_{0a}^m\left(f_a\right))\, f_r(\dot{\varepsilon}_0^m) + \sigma_{pas}^m(\varepsilon_{0a}^m\left(f_a\right))\right], \tag{4.19}$$

where $\sigma_{\max}$ is the maximum isometric stress at optimum fiber length and f_a, f_e, f_r, and σ_{pas}^m are now dimensionless functions. The functions f_a, f_e, f_r, and σ_{pas}^m in (4.19) are defined based on the structural characteristics of the muscle fiber under consideration, i.e., the aforementioned functions have a different form for different species and muscle types. Specific functional forms for these functions are given in chapter 6.

4.1.4 The fiber part of tendon

In section 3.4 it was mentioned that the primary role of tendon is to transmit the force of its associated muscle to bone. Therefore, tendon develops only "passive" stresses. The "passive" force depends only on the length of tendon fiber, and the total nominal longitudinal stress in a tendon fiber can be written as a function of nominal longitudinal strain:

$$\sigma_0^m = \sigma_{\max}\, \sigma_{pas}^m(\varepsilon_0^m), \tag{4.20}$$

where $\sigma_{\max}$ is the tendon stress when its force equals the peak isometric muscle force (Zajac, 1989) and σ_{pas}^m a dimensionless function. The tendon strain is defined by the amount of tendon stretch relative to its resting, or slack length, where the slack length is the length on elongation at which tendon just begins to develop force.

4.1.5 Constitutive description of $\boldsymbol{\sigma}^{ct}$

In the present model, isotropic linear hyperelasticity is assumed for the non-fiber part and the constitutive equation for the stress tensor is written as

$$\boldsymbol{\sigma}^{ct} = \frac{1}{J}\,\boldsymbol{\mathcal{L}}^{e} : \boldsymbol{\varepsilon}^{ct}, \tag{4.21}$$

where $J = \det \boldsymbol{F}$ and $\boldsymbol{\mathcal{L}}^{e}$ is the elasticity tensor, which can be written as

$$\boldsymbol{\mathcal{L}}^{e} = 2\,\mu\,\mathbf{K} + 3\,\kappa\,\mathbf{J}, \tag{4.22}$$

with μ and κ being the elastic shear and bulk moduli of the material. In the last equation $\mathbf{J}$ and $\mathbf{K}$ are the standard fourth-order deviatoric and spherical projection tensors defined by

$$\mathbf{J} = \frac{1}{3}\,\boldsymbol{\delta}\,\boldsymbol{\delta}, \qquad \mathbf{K} = \mathbf{I} - \mathbf{J}, \tag{4.23}$$

where $\mathbf{I}$ is the standard fourth-order symmetric identity tensor with Cartesian components

$$I_{ijkl} = \frac{1}{2}(\delta_{ik}\,\delta_{jl} + \delta_{il}\,\delta_{jk}). \tag{4.24}$$

4.1.6 Summary of constitutive equations

Muscle tissue

$$\boldsymbol{\varepsilon} = \ln \boldsymbol{V}, \qquad \boldsymbol{\varepsilon} = \boldsymbol{\varepsilon}^{f} + \boldsymbol{\varepsilon}^{ct}, \qquad \boldsymbol{\sigma} = \boldsymbol{\sigma}^{f} + \boldsymbol{\sigma}^{ct} \tag{4.25}$$

Fiber part:

$$\boldsymbol{\varepsilon}^{f} = \frac{3}{2}\,\varepsilon_m \left(\boldsymbol{m}\,\boldsymbol{m} - \frac{1}{3}\,\boldsymbol{\delta}\right), \quad \boldsymbol{m} = \frac{1}{|\boldsymbol{F}\cdot\boldsymbol{m}_0|}\,\boldsymbol{F}\cdot\boldsymbol{m}_0, \tag{4.26}$$

$$\lambda_m = \sqrt{\boldsymbol{m}_0\cdot\boldsymbol{F}^T\cdot\boldsymbol{F}\cdot\boldsymbol{m}_0}, \qquad \varepsilon_0^m = \lambda_m - 1, \qquad \varepsilon_m = \ln\lambda_m, \tag{4.27}$$

$$\boldsymbol{\sigma}^{f} = \sigma^{m}\,\boldsymbol{m}\,\boldsymbol{m}, \qquad \sigma^{m} = (1+\varepsilon_0^m)\,\sigma_0^m, \tag{4.28}$$

$$\varepsilon_{0a}^m\,(f_a) = (\varepsilon_0^m + 1)\,\{k\,[1 - f_a\,(t)] + 1\} - 1, \tag{4.29}$$

$$\sigma_0^m = \sigma_{\max}\left[f_a(t)\,f_e(\varepsilon_{0a}^m\,(f_a))\,f_r(\dot{\varepsilon}_0^m) + \sigma_{pas}^m(\varepsilon_{0a}^m\,(f_a))\right]. \tag{4.30}$$

Connective tissue and biofluids:

$$\boldsymbol{\sigma}^{ct} = \frac{1}{J}\,\boldsymbol{\mathcal{L}}^{e} : \boldsymbol{\varepsilon}^{ct}. \tag{4.31}$$

Tendon tissue

$$\boldsymbol{\varepsilon} = \ln \boldsymbol{V}, \qquad \boldsymbol{\varepsilon} = \boldsymbol{\varepsilon}^{f} + \boldsymbol{\varepsilon}^{ct}, \qquad \boldsymbol{\sigma} = \boldsymbol{\sigma}^{f} + \boldsymbol{\sigma}^{ct} \tag{4.32}$$

Fiber part:

$$\boldsymbol{\varepsilon}^f = \frac{3}{2}\,\varepsilon_m \left(\boldsymbol{m}\,\boldsymbol{m} - \frac{1}{3}\,\boldsymbol{\delta}\right), \quad \boldsymbol{m} = \frac{1}{|\boldsymbol{F}\cdot\boldsymbol{m}_0|}\,\boldsymbol{F}\cdot\boldsymbol{m}_0, \tag{4.33}$$

$$\lambda_m = \sqrt{\boldsymbol{m}_0\cdot\boldsymbol{F}^T\cdot\boldsymbol{F}\cdot\boldsymbol{m}_0}, \qquad \varepsilon_0^m = \lambda_m - 1, \qquad \varepsilon_m = \ln\lambda_m, \tag{4.34}$$

$$\boldsymbol{\sigma}^f = \sigma^m\,\boldsymbol{m}\,\boldsymbol{m}, \qquad \sigma^m = (1+\varepsilon_0^m)\,\sigma_0^m, \tag{4.35}$$

$$\sigma_0^m = \sigma_{\max}\,\sigma_{pas}^m\,(\varepsilon_0^m). \tag{4.36}$$

Connective tissue and biofluids:

$$\boldsymbol{\sigma}^{ct} = \frac{1}{J}\,\boldsymbol{\mathcal{L}}^e : \boldsymbol{\varepsilon}^{ct}. \tag{4.37}$$

We conclude this section by mentioning that the case of more than one group of muscle fibers with different orientation and properties is handled by superposition. In the case of N families of fibers, equations (4.26)-(4.30) are replaced by

$$\boldsymbol{\varepsilon}^f = \frac{3}{2}\sum_{i=1}^{N}\varepsilon_m^{(i)}\left(\boldsymbol{m}^{(i)}\,\boldsymbol{m}^{(i)} - \frac{1}{3}\,\boldsymbol{\delta}\right), \quad \boldsymbol{m}^{(i)} = \frac{1}{\left|\boldsymbol{F}\cdot\boldsymbol{m}_0^{(i)}\right|}\,\boldsymbol{F}\cdot\boldsymbol{m}_0^{(i)}, \tag{4.38}$$

$$\lambda_m^{(i)} = \sqrt{\boldsymbol{m}_0^{(i)}\cdot\boldsymbol{F}^T\cdot\boldsymbol{F}\cdot\boldsymbol{m}_0^{(i)}}, \qquad \varepsilon_0^{m(i)} = \lambda_m^{(i)} - 1, \qquad \varepsilon_m^{(i)} = \ln\lambda_m^{(i)}, \tag{4.39}$$

$$\boldsymbol{\sigma}^f = \sum_{i=1}^{N}\sigma^{m(i)}\,\boldsymbol{m}^{(i)}\,\boldsymbol{m}^{(i)}, \qquad \sigma^{m(i)} = \left(1+\varepsilon_0^{m(i)}\right)\sigma_0^{m(i)}, \tag{4.40}$$

$$\varepsilon_{0a}^{m(i)}\,(f_a) = \left(\varepsilon_0^{m(i)}+1\right)\{k\,[1-f_a\,(t)]+1\} - 1, \tag{4.41}$$

$$\sigma_0^{m(i)} = \sigma_{\max}^{(i)}\left[f_a^{(i)}(t)\,f_e^{(i)}(\varepsilon_{0a}^{m(i)})\,f_r^{(i)}(\dot{\varepsilon}_0^{m(i)}) + \sigma_{pas}^{m(i)}\,(\varepsilon_{0a}^{m(i)})\right]. \tag{4.42}$$

Similar modifications are introduced to equations (4.33)-(4.36) for the tendon.

Chapter 5

Implementation of the constitutive model in finite element program

In this chapter, a methodology for the numerical implementation of the developed non-linear and anisotropic constitutive equations for muscle and tendon in the context of the finite element method is presented.

5.1 Integral formulation of the problem

We consider the spatial configuration of a general deformable body of initial volume V_0 at time $t = 0$. At time t the body is deformed to a volume V surrounded by a surface S as shown in Figure 5.1. The body is loaded by body forces $\boldsymbol{b}$ per unit mass and traction forces $\boldsymbol{T}$ per unit area on the part S_σ of S, and imposed displacements $\hat{\boldsymbol{u}}$ on the remainder part S_u of S. The equations of equilibrium are

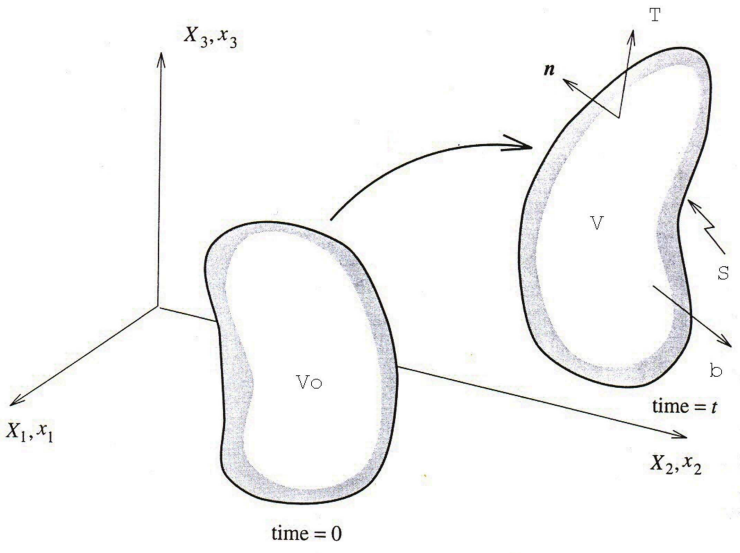

Figure 5.1: Undeformed and deformed configurations of the continuum.

$$\frac{\partial \sigma_{ij}}{\partial x_j} + \rho\, b_i = 0, \tag{5.1}$$

where σ_{ij} is the Cauchy stress tensor, and ρ is the mass density.

We consider that the displacement vector $\boldsymbol{u}$ is prescribed on part of the boundary S_u:

$$\boldsymbol{u} = \hat{\boldsymbol{u}} \equiv \text{known} \quad \text{on} \quad S_u. \tag{5.2}$$

On the remaining boundary S_σ the tractions are prescribed:

$$\boldsymbol{n} \cdot \boldsymbol{\sigma} = \boldsymbol{T} \equiv \text{known} \quad \text{on} \quad S_\sigma. \tag{5.3}$$

The problem can be formulated in an integral form as follows: Find a displacement field $\boldsymbol{u}(\boldsymbol{x})$ such that $\boldsymbol{u} = \hat{\boldsymbol{u}}$ on S_u and

$$\int_V \left[\frac{\partial \sigma_{ij}(\boldsymbol{u})}{\partial x_j} + \rho\, b_i \right] v_i^*\, dV + \int_{S_\sigma} \left[T_i - n_j\, \sigma_{ij}(\boldsymbol{u}) \right] v_i^*\, dS = 0 \tag{5.4}$$

for all continuous and differentiable fields $\boldsymbol{v}^*(\boldsymbol{x})$ that satisfy the condition $\boldsymbol{v}^* = \boldsymbol{0}$ on S_u. The stress field $\boldsymbol{\sigma}(\boldsymbol{u})$ is determined for given $\boldsymbol{u}$ via the constitutive equations.

Using Green's theorem in equation (5.4) we reach the alternative formulation: Find a displacement field $\boldsymbol{u}(\boldsymbol{x})$ such that $\boldsymbol{u} = \hat{\boldsymbol{u}}$ on S_u and

$$G(\boldsymbol{u}(\boldsymbol{x})) \equiv \int_V \boldsymbol{\sigma}(\boldsymbol{u}(\boldsymbol{x})) : \boldsymbol{D}^* dV - \int_V \rho\, \boldsymbol{b} \cdot \boldsymbol{v}^* dV - \int_S \boldsymbol{T} \cdot \boldsymbol{v}^* dS = 0 \tag{5.5}$$

for all continuous and differentiable fields $\boldsymbol{v}^*(\boldsymbol{x})$ that satisfy the condition $\boldsymbol{v}^* = \boldsymbol{0}$ on S_u. Note that $\boldsymbol{D}^*$ in equation (5.5) is given by

$$D_{ij}^* = \frac{1}{2} \left(\frac{\partial v_i^*}{\partial x_j} + \frac{\partial v_j^*}{\partial x_i} \right). \tag{5.6}$$

The vanishing of the non-linear functional $G(\boldsymbol{u})$ for all "virtual" velocity fields $\boldsymbol{v}^*(\boldsymbol{x})$ defines the "weak" solution $\boldsymbol{u}(\boldsymbol{x})$ of the problem.

The integral statement (5.5) provides the basis for the finite element formulation as described in the following section.

We conclude this section mentioning that, in view of the symmetry of $\boldsymbol{\sigma}$, equation (5.5) can be written as

$$G(\boldsymbol{u}(\boldsymbol{x})) \equiv \int_V \boldsymbol{\sigma}(\boldsymbol{u}(\boldsymbol{x})) : \boldsymbol{L}^* dV - \int_V \rho \boldsymbol{b} \cdot \boldsymbol{v}^* dV - \int_S \boldsymbol{T} \cdot \boldsymbol{v}^* dS = 0, \tag{5.7}$$

where

$$L_{ij}^* = \frac{\partial v_i^*}{\partial x_j}. \tag{5.8}$$

5.2 Finite element formulation

In a finite element setting, a non-linear problem is solved incrementally and the primary unknown is the displacement increment $\Delta \boldsymbol{u}(\boldsymbol{x})$ that defines the position of the body at the end of the increment:

$$\boldsymbol{u}_{n+1}(\boldsymbol{x}) = \boldsymbol{u}_n(\boldsymbol{x}) + \Delta \boldsymbol{u}(\boldsymbol{x}), \quad \boldsymbol{x}_{n+1}(\boldsymbol{x}) = \boldsymbol{x}_n(\boldsymbol{x}) + \Delta \boldsymbol{u}(\boldsymbol{x}) = \boldsymbol{X} + \boldsymbol{u}_{n+1}(\boldsymbol{x}). \tag{5.9}$$

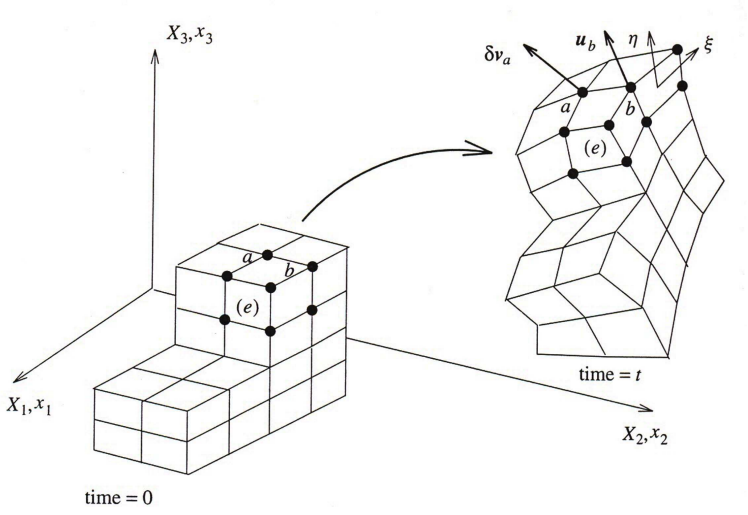

Figure 5.2: Discretization of a structure in a finite element setting.

Next, we introduce the finite element interpolation, which, at the element level, can be written as

$$\{\Delta u(\boldsymbol{x})\} = [N(\boldsymbol{x})] \left\{\Delta u_e^N\right\}, \tag{5.10}$$

where $[N(\boldsymbol{x})]$ is the interpolation matrix, and $\left\{\Delta u_e^N\right\}$ the vector of nodal unknowns of the element. In the above equation and for the rest of this chapter, the following notation is used:

$$\{\ \} \text{ denotes a column}, \quad \lfloor\ \rfloor \text{ denotes a row}, \quad [\ ] \text{ denotes a matrix.}$$

We also define $\Delta \boldsymbol{L} \equiv \partial(\Delta \boldsymbol{u})/\partial \boldsymbol{x}_{n+1}$, which is written in matrix form as

$$\{\Delta L(\boldsymbol{x})\} = [B_L(\boldsymbol{x})] \left\{\Delta u_e^N\right\}. \tag{5.11}$$

Similarly, the virtual velocity vector $\boldsymbol{v}^*$ and the corresponding velocity gradient $\boldsymbol{L}^* = \partial \boldsymbol{v}^*/\partial \boldsymbol{x}_{n+1}$ are written in matrix form as

$$\{v^*(\boldsymbol{x})\} = [N(\boldsymbol{x})] \left\{v_e^{*N}\right\}, \tag{5.12}$$

and

$$\{L^*(\boldsymbol{x})\} = [B_L(\boldsymbol{x})]\left\{v_e^{*N}\right\}. \tag{5.13}$$

Substituting the above fields in equation (5.7) we find

$$G = \left\lfloor v^{*N} \right\rfloor \mathop{\mathbf{A}}_{e} \left(\int\limits_{V_{n+1}^e} [B_L]_{n+1}^T \{\sigma\}_{n+1}\, dV - \int\limits_{V_{n+1}^e} [N]_{n+1}^T \rho\, \{b\}_{n+1}\, dV - \int\limits_{S_\sigma^e|_{n+1}} [N]_{n+1}^T \{T\}_{n+1}\, dS \right) = 0, \tag{5.14}$$

where $\left\lfloor v^{*N} \right\rfloor$ is the global row of nodal virtual velocities, and $\mathop{\mathbf{A}}_{e}$ is the "assembly operator". Since equation (5.14) must hold for arbitrary values of $\left\lfloor v^{*N} \right\rfloor$, we have that

$$\boxed{\mathop{\mathbf{A}}_{e} \int\limits_{V_{n+1}^e} [B_L]_{n+1}^T \{\sigma\}_{n+1}\, dV = \{F\}_{n+1}}, \tag{5.15}$$

where $\{F\}_{n+1}$ is the global vector of applied loads

$$\{F\}_{n+1} = \mathop{\mathbf{A}}_{e} \left(\int\limits_{V_{n+1}^e} [N]_{n+1}^T \rho\, \{b\}_{n+1}\, dV + \int\limits_{S_\sigma^e|_{n+1}} [N]_{n+1}^T \{T\}_{n+1}\, dS \right). \tag{5.16}$$

The quantity $\{\sigma\}_{n+1}$ in equation (5.15) is a non-linear function of the unknown nodal displacement increments $\left\{\Delta u^N\right\}$. Equation (5.15) provides the set of non-linear equations that determine $\left\{\Delta u^N\right\}$. In fact, (5.15) can be written as

$$\boxed{\left\{R\left(\Delta u^N\right)\right\}_{n+1} \equiv \mathop{\mathbf{A}}_{e} \int\limits_{V_{n+1}^e} [B_L]_{n+1}^T \left\{\sigma\left(\Delta u^N\right)\right\}_{n+1} dV - \{F\}_{n+1} = \{0\}}, \tag{5.17}$$

where $\left\{R\left(\Delta u^N\right)\right\}_{n+1}$ is the global "residual" force vector, i.e., the difference between the forces required to maintain $\{\sigma\}_{n+1}$ in the body and the applied forces $\{F\}_{n+1}$.

The non-linear system of equations (5.17) is solved for $\left\{\Delta u^N\right\}$ by using the Newton's method. The corresponding Jacobian matrix, which plays the role of the "stiffness matrix" now, is determined by writing equation (5.14) in the form

$$G = \left\lfloor v^{*N} \right\rfloor \{R\}_{n+1} = 0 \tag{5.18}$$

and calculating

$$dG = \left\lfloor v^{*N} \right\rfloor \frac{\partial \left\{R\left(\Delta u^N\right)\right\}_{n+1}}{\partial \left\{\Delta u^N\right\}} d\left\{\Delta u^N\right\} = \left\lfloor v^{*N} \right\rfloor [K]\, d\left\{\Delta u^N\right\}, \tag{5.19}$$

where $[K]$ is the required Jacobian matrix.

5.3 Linearization of equations — Calculation of Jacobian

The easiest way to calculate the Jacobian $[K]$ is to start with the continuum form of G, calculate the differential dG, and then introduce the finite element discretization; the resulting equation compared to equation (5.19) identifies $[K]$. The procedure is as follows.

We write $G(\Delta \boldsymbol{u})$ in the form

$$G(\Delta \boldsymbol{u}) = \int_V \operatorname{tr}\left(\boldsymbol{\sigma} \cdot \frac{\partial \boldsymbol{v}^*}{\partial \boldsymbol{x}}\right) dV - \int_{V_0} \rho_0 \, \boldsymbol{b} \cdot \boldsymbol{v}^* dV_0 - \int_{S_\sigma^0} \boldsymbol{T}^0 \cdot \boldsymbol{v}^* dS_0, \tag{5.20}$$

where $\boldsymbol{T}^0$ is the nominal traction vector and ρ_0 the initial density. In equation (5.20) and for the rest of this section all quantities are evaluated at the end of the increment, unless indicated otherwise. We also note that

$$d\boldsymbol{x} = d\boldsymbol{x}_{n+1} = d(\boldsymbol{x}_n + \Delta \boldsymbol{u}) = d(\Delta \boldsymbol{u}). \tag{5.21}$$

Next, we note that

$$\int_V \operatorname{tr}\left(\boldsymbol{\sigma} \cdot \frac{\partial \boldsymbol{v}^*}{\partial \boldsymbol{x}}\right) dV = \int_{V_0} \operatorname{tr}\left(\boldsymbol{\sigma} \cdot \frac{\partial \boldsymbol{v}^*}{\partial \boldsymbol{X}} \cdot \frac{\partial \boldsymbol{X}}{\partial \boldsymbol{x}}\right) J \, dV_0 = \int_{V_0} \operatorname{tr}\left(\boldsymbol{\sigma} \cdot \frac{\partial \boldsymbol{v}^*}{\partial \boldsymbol{X}} \cdot \boldsymbol{F}^{-1}\right) J \, dV_0, \tag{5.22}$$

so that equation (5.20) can be written as

$$G(\Delta \boldsymbol{u}) = \int_{V_0} \operatorname{tr}\left(\frac{\partial \boldsymbol{v}^*}{\partial \boldsymbol{X}} \cdot \boldsymbol{F}^{-1} \cdot \boldsymbol{\sigma}\right) J \, dV_0 - \int_{V_0} \rho_0 \, \boldsymbol{b} \cdot \boldsymbol{v}^* dV_0 - \int_{S_\sigma^0} \boldsymbol{T}^0 \cdot \boldsymbol{v}^* dS_0. \tag{5.23}$$

We assume now that the applied loads are independent of the motion of the body, i.e., we exclude "follower forces". Then

$$dG = \int_{V_0} \operatorname{tr}\left\{\frac{\partial \boldsymbol{v}^*}{\partial \boldsymbol{X}} \cdot \left[d\left(\boldsymbol{F}^{-1}\right) \cdot \boldsymbol{\sigma} + \boldsymbol{F}^{-1} \cdot d\boldsymbol{\sigma} + \boldsymbol{F}^{-1} \cdot \boldsymbol{\sigma} \, \frac{dJ}{J}\right]\right\} J \, dV_0, \tag{5.24}$$

where $J = \det(\boldsymbol{F})$. Also

$$\frac{\partial \boldsymbol{v}^*}{\partial \boldsymbol{X}} = \frac{\partial \boldsymbol{v}^*}{\partial \boldsymbol{x}} \cdot \frac{\partial \boldsymbol{x}}{\partial \boldsymbol{X}} = \boldsymbol{L}^* \cdot \boldsymbol{F}, \tag{5.25}$$

so that equation (5.24) becomes

$$dG = \int_V \operatorname{tr}\left\{\boldsymbol{L}^* \cdot \left[\boldsymbol{F} \cdot d\left(\boldsymbol{F}^{-1}\right) \cdot \boldsymbol{\sigma} + d\boldsymbol{\sigma} + \frac{dJ}{J} \, \boldsymbol{\sigma}\right]\right\} dV. \tag{5.26}$$

Next, we evaluate the quantities $\boldsymbol{F} \cdot d\left(\boldsymbol{F}^{-1}\right)$, $d\boldsymbol{\sigma}$, and dJ/J.

Evaluation of $\boldsymbol{F} \cdot d\left(\boldsymbol{F}^{-1}\right)$

$$\boldsymbol{F} \cdot \boldsymbol{F}^{-1} = \boldsymbol{\delta} \quad \Rightarrow \quad d\boldsymbol{F} \cdot \boldsymbol{F}^{-1} + \boldsymbol{F} \cdot d\left(\boldsymbol{F}^{-1}\right) = \boldsymbol{0} \quad \Rightarrow \quad \boxed{\boldsymbol{F} \cdot d\left(\boldsymbol{F}^{-1}\right) = -d\boldsymbol{F} \cdot \boldsymbol{F}^{-1}}. \tag{5.27}$$

Also,

$$\boldsymbol{F} = \frac{\partial \boldsymbol{x}}{\partial \boldsymbol{X}} \quad \Rightarrow \quad d\boldsymbol{F} = \frac{\partial \left(d\boldsymbol{x}\right)}{\partial \boldsymbol{X}} \quad \text{or} \quad \boxed{d\boldsymbol{F} = \frac{\partial \left[d\left(\Delta \boldsymbol{u}\right)\right]}{\partial \boldsymbol{X}}}. \tag{5.28}$$

Therefore,

$$\xrightarrow[(5.28)]{(5.27)} \quad \boldsymbol{F} \cdot d\left(\boldsymbol{F}^{-1}\right) = -\frac{\partial \left[d\left(\Delta \boldsymbol{u}\right)\right]}{\partial \boldsymbol{X}} \cdot \frac{\partial \boldsymbol{X}}{\partial \boldsymbol{x}} = -\frac{\partial \left[d\left(\Delta \boldsymbol{u}\right)\right]}{\partial \boldsymbol{x}} \quad \Rightarrow \quad \boxed{\boldsymbol{F} \cdot d\left(\boldsymbol{F}^{-1}\right) = -d\boldsymbol{L}}, \tag{5.29}$$

where

$$\boxed{d\boldsymbol{L} \equiv \frac{\partial [d(\Delta \boldsymbol{u})]}{\partial \boldsymbol{x}}}. \tag{5.30}$$

Evaluation of dJ/J

We recall that $\partial J/\partial F_{\kappa i} = J\left(\boldsymbol{F}^{-1}\right)_{i\kappa}$, which implies that

$$dJ = J\left(\boldsymbol{F}^{-1}\right)_{i\kappa} dF_{\kappa i} = J\left(\boldsymbol{F}^{-1} \cdot d\boldsymbol{F}\right)_{ii} = J \operatorname{tr}\left(\boldsymbol{F}^{-1} \cdot d\boldsymbol{F}\right) =$$

$$= J \operatorname{tr}\left[\frac{\partial \boldsymbol{X}}{\partial \boldsymbol{x}} \cdot \frac{\partial \left(d\Delta \boldsymbol{u}\right)}{\partial \boldsymbol{X}}\right] = J \operatorname{tr}\left[\frac{\partial \left(d\Delta \boldsymbol{u}\right)}{\partial \boldsymbol{x}}\right] = J \operatorname{tr}\left(d\boldsymbol{L}\right), \tag{5.31}$$

or

$$\boxed{\frac{dJ}{J} = dL_{\kappa\kappa}}. \tag{5.32}$$

Evaluation of $d\boldsymbol{\sigma}$

We note that $d\boldsymbol{\sigma}$ denotes the variation of $\boldsymbol{\sigma}$ with respect to the displacement increment $\Delta \boldsymbol{u}$. In general, $d\boldsymbol{\sigma}$ depends on the constitutive model *and* the algorithm used for the numerical implementation of the constitutive equations. The exact evaluation of $d\boldsymbol{\sigma}$ in finite strain problems is always very involved. In order to simplify the calculation, we use the following approximate technique.

We assume that the numerical implementation of the constitutive model defines somehow a relationship of the form

$$\overset{\triangledown}{\boldsymbol{\sigma}} = \mathbf{C} : \boldsymbol{D} = \mathbf{C} : \boldsymbol{L}, \tag{5.33}$$

where $\overset{\triangledown}{\boldsymbol{\sigma}}$ is a fourth-order tensor, $\mathbf{C}$ is a fourth order tensor, $\boldsymbol{L} = \partial \boldsymbol{v}/\partial \boldsymbol{x}$, and $\boldsymbol{D} = (1/2)(\boldsymbol{L} + \boldsymbol{L}^T)$. Then

$$\dot{\boldsymbol{\sigma}} = \overset{\triangledown}{\boldsymbol{\sigma}} - \boldsymbol{\sigma} \cdot \boldsymbol{W} + \boldsymbol{W} \cdot \boldsymbol{\sigma} = \mathbf{C} : \boldsymbol{L} - \frac{1}{2}\boldsymbol{\sigma} \cdot \left(\boldsymbol{L} - \boldsymbol{L}^T\right) + \frac{1}{2}\left(\boldsymbol{L} - \boldsymbol{L}^T\right) \cdot \boldsymbol{\sigma}. \tag{5.34}$$

Based on equation (5.34), we introduce the *approximation* that

$$\boxed{d\boldsymbol{\sigma} \cong \mathbf{C} : d\boldsymbol{L} - \frac{1}{2}\boldsymbol{\sigma} \cdot \left(d\boldsymbol{L} - d\boldsymbol{L}^T\right) + \frac{1}{2}\left(d\boldsymbol{L} - d\boldsymbol{L}^T\right) \cdot \boldsymbol{\sigma}} \tag{5.35}$$

Now, we return to equation (5.26) where we substitute the quantities $\boldsymbol{F} \cdot d\left(\boldsymbol{F}^{-1}\right)$, $d\boldsymbol{\sigma}$, and

dJ/J from equations (5.30), (5.32), and (5.35) respectively. So we find that

$$dG = \int_V \boldsymbol{L}^* : \left[\mathbf{C} : d\boldsymbol{L} - \frac{1}{2}\,\boldsymbol{\sigma} \cdot \left(d\boldsymbol{L} + d\boldsymbol{L}^T \right) + \frac{1}{2}\left(d\boldsymbol{L} - d\boldsymbol{L}^T \right) \cdot \boldsymbol{\sigma} + dL_{kk}\,\boldsymbol{\sigma} \right] dV, \tag{5.36}$$

where we took into account that $\mathrm{tr}\,(\boldsymbol{A} \cdot \boldsymbol{B}) = A_{ik}\,B_{ki} = \boldsymbol{A} : \boldsymbol{B}^T$.

Note that, in view of (5.33) and (5.35), $\mathbf{C}$ essentially relates the variation of the true stress $\boldsymbol{\sigma}$, as seen by an observer spinning with the continuum, to the symmetric part of $d\boldsymbol{L}$, which, in turn, is determined in terms of the variation of the nodal displacement increments $\boldsymbol{\Delta u}$ by equation 5.30.

Alternatively, we can write equation (5.36) as

$$\boxed{dG = \int_V \boldsymbol{L}^* : (\mathbf{C} + \boldsymbol{\Sigma} + \boldsymbol{\sigma}\,\boldsymbol{\delta}) : d\boldsymbol{L}\, dV}\,, \tag{5.37}$$

where

$$\Sigma_{ijkl} = \frac{1}{2}\,\left(\delta_{ik}\,\sigma_{jl} - \delta_{il}\,\sigma_{jk} - \sigma_{ik}\,\delta_{jl} + \sigma_{il}\,\delta_{jk} \right). \tag{5.38}$$

Next, we introduce the finite element discretization

$$\{L^*\} = [B_L]\{v_e^{*N}\} \quad \text{and} \quad \{dL\} = [B_L]\, d\{u_e^N\} \tag{5.39}$$

in equation (5.37) to find

$$dG = \lfloor v^{*N} \rfloor \left(\mathop{\mathbf{A}}_{e} \int_{V^e} [B_L]^T ([C] + [\Sigma] + \{\sigma\}\lfloor\delta\rfloor)[B_L]\, dV \right) d\{\Delta u^N\}, \tag{5.40}$$

where $\{\sigma\}$ and $\{\delta\}$ are the vector representation of the stress tensor and the second order identity tensor, and $[C]$ and $[\Sigma]$ are the matrix form of the fourth-order tensors $\mathbf{C}$ and $\boldsymbol{\Sigma}$ (e.g., see Papatriantafyllou, 2005). Referring now to equation (5.19), we conclude that

$$[K] = \mathop{\mathbf{A}}_{e} [k^e], \tag{5.41}$$

where $[k^e]$ is the "element stiffness matrix" defined as

$$\boxed{[k^e] = \int_{V^e} [B_L]^T \left([C] + [\Sigma] + \{\sigma\}\lfloor\delta\rfloor \right) [B_L]\, dV.} \tag{5.42}$$

It should be noted that, because of the approximation involved in equation (5.35), the expression for the Jacobian given in equation (5.42) is approximate as well. However, this approximation influences only the rate of convergence of the overall equilibrium iterations for the solution of equation (5.17) and not the accuracy of the solution, which depends on the "tolerance" used in (5.17). The exact Jacobian is more involved and is discussed in detail in Ramaswamy and Aravas (1998).

It should be noted also that $[\Sigma]$ is a symmetric matrix, whereas the product $\{\sigma\}\lfloor\delta\rfloor$ results in a non-symmetric matrix (Papatriantafyllou, 2005). In our model $[C]$ is non-symmetric as well. Therefore, the corresponding $[k^e]$ is non-symmetric. ABAQUS is based on the formulation outlined above and uses equation (5.42) for the calculation of the Jacobian; the $[\Sigma]$ matrix is included automatically in finite-strain analysis and the user has to provide the sum $[C] + \{\sigma\}\lfloor\delta\rfloor$ via the subroutine UMAT. Our experience indicates that, when $[k^e]$ in equation (5.42) is replaced by its symmetric part, the required solution time decreases whereas the overall rate of convergence is not affected substantially.

5.4 Implementation in ABAQUS

From a numerical viewpoint, the implementation of a constitutive model in a finite element code involves the evaluation of the constitutive equations at the Gauss integration points of the elements and the calculation of the corresponding "linearization moduli" that are needed for the global equilibrium "Newton loop". The constitutive model is implemented in the ABAQUS general purpose finite element code; this program provides a general interface so that a particular constitutive model can be introduced as a "user subroutine" (UMAT). The subroutine UMAT passes in all the information at the start of the increment, i.e., $(\boldsymbol{F}_n, \boldsymbol{\sigma}_n, \varepsilon_m|_n, \boldsymbol{m}_n, \boldsymbol{\sigma}^{ct}|_n)$, as well as $\boldsymbol{F}_{n+1}$ at time $t_{n+1} = t_n + \Delta t$, and the user has to calculate the values of the corresponding quantities at the end of the increment, i.e., $(\boldsymbol{\sigma}_{n+1}, \varepsilon_m|_{n+1}, \boldsymbol{m}_{n+1}, \boldsymbol{\sigma}^{ct}|_{n+1})$. The model is then used for the analysis of static and dynamic problems using the "standard-implicit" version of the code.

The finite element formulation is based on the "weak" form of the momentum balance, the solution is developed incrementally, and the discretized non-linear equations are solved by using the Newton's method, which requires the aforementioned linearization moduli $\partial\boldsymbol{\sigma}/\partial\boldsymbol{\varepsilon}$, where $\boldsymbol{\sigma}$ and $\boldsymbol{\varepsilon}$ are the stress and strain tensors respectively.

5.5 Numerical implementation of the model

The constitutive calculations are carried out in UMAT in the following order:

$$\boldsymbol{V}_{n+1} = \sqrt{\boldsymbol{F}_{n+1} \cdot \boldsymbol{F}_{n+1}^T} = \sum_{i=1}^{3} \lambda_i \, \boldsymbol{n}_i \, \boldsymbol{n}_i, \tag{5.43}$$

$$\boldsymbol{\varepsilon}_{n+1} = \ln \boldsymbol{V}_{n+1} = \sum_{i=1}^{3} \ln \lambda_i \, \boldsymbol{n}_i \, \boldsymbol{n}_i, \tag{5.44}$$

$$\lambda_m|_{n+1} = \sqrt{\boldsymbol{m}_0 \cdot \boldsymbol{F}_{n+1}^T \cdot \boldsymbol{F}_{n+1} \cdot \boldsymbol{m}_0}, \tag{5.45}$$

$$\varepsilon_0^m|_{n+1} = \lambda_m|_{n+1} - 1, \qquad \varepsilon_m|_{n+1} = \ln \lambda_m|_{n+1}, \tag{5.46}$$

$$\boldsymbol{m}_{n+1} = \frac{1}{|\boldsymbol{F}_{n+1} \cdot \boldsymbol{m}_0|} \boldsymbol{F}_{n+1} \cdot \boldsymbol{m}_0, \tag{5.47}$$

$$\boldsymbol{\varepsilon}^f|_{n+1} = \frac{3}{2} \varepsilon_m|_{n+1} (\boldsymbol{m}_{n+1} \, \boldsymbol{m}_{n+1} - \frac{1}{3} \boldsymbol{\delta}), \tag{5.48}$$

$$\boldsymbol{\varepsilon}_{n+1}^{ct} = \boldsymbol{\varepsilon}_{n+1} - \boldsymbol{\varepsilon}_{n+1}^{f}, \tag{5.49}$$

$$\dot{\varepsilon}_0^m = \frac{\varepsilon_0^m|_{n+1} - \varepsilon_0^m|_n}{\Delta t}, \tag{5.50}$$

$$\varepsilon_{0a}^m|_{n+1} = (\varepsilon_0^m|_{n+1} + 1) \left\{ k \left[1 - f_a \left(t_{n+1} \right) \right] + 1 \right\} - 1, \tag{5.51}$$

$$\sigma_0^m|_{n+1} = \sigma_{\max} \left[f_a(t_{n+1}) \, f_e(\varepsilon_{0a}^m|_{n+1}) \, f_r(\dot{\varepsilon}_0^m) + \sigma_{pas}^m(\varepsilon_{0a}^m|_{n+1}) \right], \tag{5.52}$$

$$\sigma_{n+1}^m = (1 + \varepsilon_0^m|_{n+1}) \, \sigma_0^m|_{n+1}, \tag{5.53}$$

$$\boldsymbol{\sigma}_{n+1}^f = \sigma_{n+1}^m \, \boldsymbol{m}_{n+1} \, \boldsymbol{m}_{n+1}, \tag{5.54}$$

$$\boldsymbol{\sigma}_{n+1}^{ct} = \frac{1}{\det \boldsymbol{F}_{n+1}} \boldsymbol{\mathcal{L}}^e : \boldsymbol{\varepsilon}_{n+1}^{ct}, \tag{5.55}$$

and

$$\boldsymbol{\sigma}_{n+1} = \boldsymbol{\sigma}_{n+1}^f + \boldsymbol{\sigma}_{n+1}^{ct}, \tag{5.56}$$

where λ_i^2 and $\boldsymbol{n}_i$ are the eigenvalues and eigenvectors respectively of the left Cauchy-Green tensor $\boldsymbol{B}_{n+1} = \boldsymbol{F}_{n+1} \cdot \boldsymbol{F}_{n+1}^T$.

5.5.1 The linearization moduli

As discussed in section 5.3, we use the numerical implementation of the constitutive model to derive an equation of the form

$$\overset{\triangledown}{\boldsymbol{\sigma}} = \mathbf{C} : \boldsymbol{D}. \tag{5.57}$$

The fourth order tensor $\mathbf{C}$ in the above equation is used to evaluate approximately the "linearization moduli" (see equation (5.36) and the comment that follows it). In the following, we derive equation (5.57) for the constitutive model under consideration, based on the numerical implementation scheme described in the previous section 5.5.

The total stress tensor is written in the form $\boldsymbol{\sigma}_{n+1} = \boldsymbol{\sigma}_{n+1}^f + \boldsymbol{\sigma}_{n+1}^{ct}$, which implies that

$$\overset{\triangledown}{\boldsymbol{\sigma}} = \overset{\triangledown}{\boldsymbol{\sigma}}^f + \overset{\triangledown}{\boldsymbol{\sigma}}^{ct}, \tag{5.58}$$

where for simplicity we drop the subscripts $n+1$.

Calculation of $\overset{\triangledown}{\boldsymbol{\sigma}}^f$

The fiber part of the stress tensor is written in the form

$$\boldsymbol{\sigma}^f = \sigma^m \, \boldsymbol{m}\,\boldsymbol{m}. \tag{5.59}$$

By taking the derivative of equation (5.59) we find

$$\overset{\triangledown}{\boldsymbol{\sigma}}^f = \dot{\sigma}^m \, \boldsymbol{m}\,\boldsymbol{m} + \sigma^m \left(\overset{\triangledown}{\boldsymbol{m}}\,\boldsymbol{m} + \boldsymbol{m}\,\overset{\triangledown}{\boldsymbol{m}} \right). \tag{5.60}$$

Calculation of $\dot{\sigma}^m$

The true (Cauchy) stress in a fiber is determined from

$$\sigma^m = (1+\varepsilon_0^m)\,\sigma_0^m = \exp(\varepsilon_m)\,\sigma_0^m. \tag{5.61}$$

We calculate $\dot{\sigma}^m$ by taking the derivative of equation (5.61), where the quantities $\dot{\sigma}_0^m$ and $\dot{\varepsilon}^m$ are to be calculated.

To calculate $\dot{\varepsilon}^m$ we use the following relation for the true longitudinal strain in a fiber:

$$\dot{\varepsilon}_m = \boldsymbol{m}\cdot\boldsymbol{D}\cdot\boldsymbol{m} = (\boldsymbol{m}\,\boldsymbol{m}) : \boldsymbol{D}. \tag{5.62}$$

Also, for later use, we calculate the quantity $\dot{\varepsilon}_0^m$:

$$\varepsilon_0^m = \exp(\varepsilon_m) - 1 \quad \Rightarrow \quad \dot{\varepsilon}_0^m = \exp(\varepsilon_m)\,\dot{\varepsilon}_m \quad \xrightarrow{(5.62)}$$

$$\dot{\varepsilon}_0^m = (1+\varepsilon_0^m)(\boldsymbol{m}\,\boldsymbol{m}) : \boldsymbol{D}. \tag{5.63}$$

To calculate $\dot{\sigma}_0^m$ we use the following relation for the nominal stress in a fiber:

$$\sigma_0^m|_{n+1} = f\left(\varepsilon_0^m|_{n+1}, \frac{\varepsilon_0^m|_{n+1} - \varepsilon_0^m|_n}{\Delta t}, t_{n+1} \right). \tag{5.64}$$

By derivation of equation (5.64) we have

$$\dot{\sigma}_0^m = \frac{\partial f}{\partial \varepsilon_0^m}\dot{\varepsilon}_0^m + \frac{1}{\Delta t}\frac{\partial f}{\partial \dot{\varepsilon}_0^m}\dot{\varepsilon}_0^m = \left(\frac{\partial f}{\partial \varepsilon_0^m} + \frac{1}{\Delta t}\frac{\partial f}{\partial \dot{\varepsilon}_0^m} \right)\dot{\varepsilon}_0^m \quad \xrightarrow{(5.63)}$$

$$\dot{\sigma}_0^m = G(\boldsymbol{m}\,\boldsymbol{m}) : \boldsymbol{D}, \tag{5.65}$$

where

$$G = (1+\varepsilon_0^m)\left(\frac{\partial f}{\partial \varepsilon_0^m} + \frac{1}{\Delta t}\frac{\partial f}{\partial \dot{\varepsilon}_0^m} \right). \tag{5.66}$$

Now we return to equation (5.61) and by derivation we have

$$\dot{\sigma}^m = \exp(\varepsilon_m)\,(\dot{\varepsilon}^m\,\sigma_0^m + \dot{\sigma}_0^m) \quad \xrightarrow{(5.62),\ (5.65)}$$

$$\dot{\sigma}^m = \exp(\varepsilon_m)\,[\sigma_0^m(\boldsymbol{m}\,\boldsymbol{m}) : \boldsymbol{D} + G(\boldsymbol{m}\,\boldsymbol{m}) : \boldsymbol{D}] \quad \Rightarrow$$

$$\dot{\sigma}^m = (1+\varepsilon_0^m)(\sigma_0^m + G)(\boldsymbol{m}\,\boldsymbol{m}) : \boldsymbol{D}. \tag{5.67}$$

Calculation of $\overset{\triangledown}{\boldsymbol{m}}\,\boldsymbol{m} + \boldsymbol{m}\,\overset{\triangledown}{\boldsymbol{m}}$

To calculate $\overset{\triangledown}{\boldsymbol{m}}$ we use the following relation

$$\dot{\boldsymbol{m}} = (\boldsymbol{W} + \boldsymbol{D}\cdot\boldsymbol{m}\,\boldsymbol{m} - \boldsymbol{m}\,\boldsymbol{m}\cdot\boldsymbol{D})\cdot\boldsymbol{m} \quad \Rightarrow \quad \overset{\triangledown}{\boldsymbol{m}} = (\boldsymbol{D}\cdot\boldsymbol{m}\,\boldsymbol{m} - \boldsymbol{m}\,\boldsymbol{m}\cdot\boldsymbol{D})\cdot\boldsymbol{m} \tag{5.68}$$

or

$$\overset{\triangledown}{\boldsymbol{m}} = \boldsymbol{D}\cdot\boldsymbol{m} - \boldsymbol{m}(\boldsymbol{m}\,\boldsymbol{m}) : \boldsymbol{D}. \tag{5.69}$$

Therefore

$$\begin{aligned} \overset{\triangledown}{\boldsymbol{m}}\,\boldsymbol{m} + \boldsymbol{m}\,\overset{\triangledown}{\boldsymbol{m}} &= [\boldsymbol{D}\cdot\boldsymbol{m} - \boldsymbol{m}\,(\boldsymbol{m}\,\boldsymbol{m}) : \boldsymbol{D}]\;\boldsymbol{m} + \boldsymbol{m}\;[\boldsymbol{D}\cdot\boldsymbol{m} - \boldsymbol{m}\,(\boldsymbol{m}\,\boldsymbol{m}) : \boldsymbol{D}] = \\ &= \overset{\triangledown}{\boldsymbol{m}}\,\boldsymbol{m} + \boldsymbol{m}\,\overset{\triangledown}{\boldsymbol{m}} = \boldsymbol{D}\cdot\boldsymbol{m}\,\boldsymbol{m} + \boldsymbol{m}\,\boldsymbol{D}\cdot\boldsymbol{m} - 2\,\boldsymbol{m}\,\boldsymbol{m}(\boldsymbol{m}\,\boldsymbol{m}) : \boldsymbol{D}, \end{aligned} \tag{5.70}$$

which implies that

$$\overset{\triangledown}{\boldsymbol{m}}\,\boldsymbol{m} + \boldsymbol{m}\,\overset{\triangledown}{\boldsymbol{m}} = \mathbf{B} : \boldsymbol{D}, \tag{5.71}$$

where

$$B_{ijkl} = \frac{1}{2}\left[(\delta_{ik}\,m_j + \delta_{jk}\,m_i)\;m_l + (\delta_{il}\,m_j + \delta_{jl}\,m_i)\;m_k\right] - 2m_i\,m_j\,m_k\,m_l. \tag{5.72}$$

Substituting $\dot{\sigma}^m$ and $\overset{\triangledown}{\boldsymbol{m}}\,\boldsymbol{m} + \boldsymbol{m}\,\overset{\triangledown}{\boldsymbol{m}}$ from (5.67) and (5.71) into (5.60), we find

$$\overset{\triangledown}{\boldsymbol{\sigma}}^f = (1+\varepsilon_0^m)(\sigma_0^m + G)(\boldsymbol{m}\,\boldsymbol{m}) : \boldsymbol{D}\,\boldsymbol{m}\,\boldsymbol{m} + \sigma^m\,\mathbf{B} : \boldsymbol{D}, \tag{5.73}$$

or

$$\boxed{\overset{\triangledown}{\boldsymbol{\sigma}}^f = \mathbf{C}^f : \boldsymbol{D}}, \qquad \boxed{\mathbf{C}^f = (1+\varepsilon_0^m)(\sigma_0^m + G)\,\boldsymbol{m}\,\boldsymbol{m}\,\boldsymbol{m}\,\boldsymbol{m} + \sigma^m\,\mathbf{B}}. \tag{5.74}$$

Note that the fourth-order tensor $\mathbf{C}^f$ has both the "minor" and "major" symmetries, i.e.,

$$C^f_{ijkl} = C^f_{jikl} = C^f_{ijlk} = C^f_{klij}. \tag{5.75}$$

Calculation of $\overset{\triangledown}{\boldsymbol{\sigma}}{}^{ct}$

The non-fiber part of the stress tensor is written in the form

$$\boldsymbol{\sigma}^{ct} = \frac{1}{J}\,\boldsymbol{\mathcal{L}}^{e} : \boldsymbol{\varepsilon}^{ct}, \tag{5.76}$$

so that

$$\overset{\triangledown}{\boldsymbol{\sigma}}{}^{ct} = \frac{1}{J}\,\boldsymbol{\mathcal{L}}^{e} : \overset{\triangledown}{\boldsymbol{\varepsilon}}{}^{ct} - \frac{\dot{J}}{J^2}\,\boldsymbol{\mathcal{L}}^{e} : \boldsymbol{\varepsilon}^{ct} \cong \frac{1}{J}\,\boldsymbol{\mathcal{L}}^{e} : \boldsymbol{D}^{ct} - \boldsymbol{\sigma}^{ct}\,\boldsymbol{\delta} : \boldsymbol{D}, \tag{5.77}$$

where we took into account that $\overset{\triangledown}{\boldsymbol{\varepsilon}} \cong \boldsymbol{D}$ (Hill, 1978; Mehrabadi and Nemat-Nasser, 1987) and $\dot{J} = J\,D_{kk} = J\,\boldsymbol{\delta} : \boldsymbol{D}$.

Calculation of $\boldsymbol{D}^{ct}$

By taking the derivative of equation $\boldsymbol{\varepsilon}^{f} = \frac{3}{2}\,\varepsilon_m\left(\boldsymbol{m}\,\boldsymbol{m} - \frac{1}{3}\,\boldsymbol{\delta}\right)$ we find

$$\boldsymbol{D}^{f} \cong \overset{\triangledown}{\boldsymbol{\varepsilon}}{}^{f} = \frac{3}{2}\,\dot{\varepsilon}_m\left(\boldsymbol{m}\,\boldsymbol{m} - \frac{1}{3}\boldsymbol{\delta}\right) + \frac{3}{2}\,\varepsilon_m(\overset{\triangledown}{\boldsymbol{m}}\,\boldsymbol{m} + \boldsymbol{m}\,\overset{\triangledown}{\boldsymbol{m}}) \quad \xrightarrow{(5.62),\ (5.71)}$$

$$\boldsymbol{D}^{f} = \frac{3}{2}(\boldsymbol{m}\,\boldsymbol{m}) : \boldsymbol{D}\left(\boldsymbol{m}\,\boldsymbol{m} - \frac{1}{3}\boldsymbol{\delta}\right) + \frac{3}{2}\varepsilon_m\,\mathbf{B} : \boldsymbol{D} \quad \Rightarrow$$

$$\boldsymbol{D}^{f} = \frac{3}{2}\left[\left(\boldsymbol{m}\,\boldsymbol{m} - \frac{1}{3}\boldsymbol{\delta}\right)\boldsymbol{m}\,\boldsymbol{m} + \varepsilon_m\,\mathbf{B}\right] : \boldsymbol{D}. \tag{5.78}$$

Then, by taking the Jaumann derivative of equation $\boldsymbol{\varepsilon}^{ct} = \boldsymbol{\varepsilon} - \boldsymbol{\varepsilon}^{f}$ we find

$$\overset{\triangledown}{\boldsymbol{\varepsilon}}{}^{ct} = \overset{\triangledown}{\boldsymbol{\varepsilon}} - \overset{\triangledown}{\boldsymbol{\varepsilon}}{}^{f} \quad \Rightarrow \quad \boldsymbol{D}^{ct} \cong \boldsymbol{D} - \boldsymbol{D}^{f} \quad \xrightarrow{(5.78)}$$

$$\boldsymbol{D}^{ct} = \left\{\mathbf{I} - \frac{3}{2}\left[\left(\boldsymbol{m}\,\boldsymbol{m} - \frac{1}{3}\,\boldsymbol{\delta}\right)\boldsymbol{m}\,\boldsymbol{m} + \varepsilon_m\,\mathbf{B}\right]\right\} : \boldsymbol{D}, \tag{5.79}$$

where $\mathbf{I}$ is the fourth-order symmetric identity tensor with Cartesian components

$$I_{ijkl} = \frac{1}{2}\,(\delta_{ik}\,\delta_{jl} + \delta_{il}\,\delta_{jk})\,. \tag{5.80}$$

Substituting (5.79) into (5.77), we conclude that $\overset{\triangledown}{\boldsymbol{\sigma}}{}^{ct}$ can be written in the form

$$\boxed{\overset{\triangledown}{\boldsymbol{\sigma}}{}^{ct} = \mathbf{C}^{ct} : \boldsymbol{D}}, \quad \boxed{\mathbf{C}^{ct} = \frac{1}{J}\,\boldsymbol{\mathcal{L}}^{e} : \left\{\mathbf{I} - \frac{3}{2}\left[\left(\boldsymbol{m}\,\boldsymbol{m} - \frac{1}{3}\boldsymbol{\delta}\right)\boldsymbol{m}\,\boldsymbol{m} + \varepsilon_m\,\mathbf{B}\right]\right\} - \boldsymbol{\sigma}^{ct}\,\boldsymbol{\delta}}. \tag{5.81}$$

Note that $\mathbf{C}^{ct}$ has only the minor but not the major symmetries, i.e.,

$$C^{ct}_{ijkl} = C^{ct}_{jikl} = C^{ct}_{ijlk} \neq C^{ct}_{klij}. \tag{5.82}$$

Finally, substituting eqauations (5.74) and (5.81) for $\overset{\triangledown}{\boldsymbol{\sigma}}^{f}$ and $\overset{\triangledown}{\boldsymbol{\sigma}}^{ct}$ respectively into (5.58), we find an approximation $\mathbf{C}$ for the "linearization moduli", i.e.,

$$\boxed{\overset{\triangledown}{\boldsymbol{\sigma}} \cong \mathbf{C} : \boldsymbol{D}} \qquad \text{with} \qquad \boxed{\mathbf{C} = \mathbf{C}^{f} + \mathbf{C}^{ct}}. \tag{5.83}$$

We mention once again that the approximations used for the evaluation of the Jacobian matrix influence only the rate of convergence of the overall equilibrium iteration and they **do not affect the accuracy of the solution**, which depends on the "equilibrium tolerance" used to terminate the iterations. Our experience shows that the approximation of the Jacobian matrix $\mathbf{C}$ defined by equation (5.83) maintains the asymptotic quadratic convergence rate of the Newton scheme.

Chapter 6

Applications

In this chapter, we use the constitutive model developed for the muscle and tendon to study computationally the behavior of several muscle-tendon complex cases. Firstly, the extension of a squid tentacle during the strike to catch prey is simulated. Although the tentacle of a squid is a non-skeletal muscle, the problem of its extension during the strike to catch prey is studied in order to validate the developed code. Then, applications that involve skeletal muscles are considered. The behavior of a parallel fibered and a pennated muscle is studied. The model is used also to study the behavior of the human semitendinosus muscle. Finally, the constitutive model of muscle and tendon tissues is applied to the muscles and tendons of the human leg.

6.1 Extension of a squid tentacle

An attempt is made to reproduce the extension of a squid tentacle during the strike to catch prey. This problem has been studied experimentally and described in detail by Van Leeuwen and Kier, 1997. A computational solution to this problem has been given recently by Liang *et al.*, 2006. In order to validate our constitutive model and the computer code we use a formulation similar to that used by Liang *et al.* A schematic representation of the squid and its structure is given in Fig. 6.1.

The stalk is modeled as deformable with the properties described in chapter 4. The exact constitutive relation used for the fibers of the stalk is

$$\sigma_0^m = \sigma_{\max} f_a(t)\, f_e(\varepsilon_0^m)\, f_r(\dot{\varepsilon}_0^m) + \sigma_{pas}^m(\varepsilon_0^m), \tag{6.1}$$

as described in section 4.1.2. The shear modulus G for the connective tissues is assumed to be 5 kPa, while the bulk modulus K is taken as $50 \cdot 10^3$ kPa, or, equivalently $E = \frac{9GK}{G+3K} \cong 15$ kPa and $\nu = \frac{3K-2G}{2(G+3K)} \cong 0.49995$, where E and ν are the elastic Young's modulus and Poisson's ratio respectively.

The club is modeled as passive, homogeneous and elastic, with high shear and bulk moduli. The outermost thin layer of the stalk represents an annulus of longitudinal muscle

(LM) with fibers in the axial direction. It occupies about 15% of the cross-sectional area of the stalk. The inner elements in the stalk contain two orthogonal transverse muscle (TM) groups. The mechanical properties of other muscle groups, such as helical HM and circumferential CM, are neglected due to their low volume fraction and inactivity during the strike (Fig. 6.2).

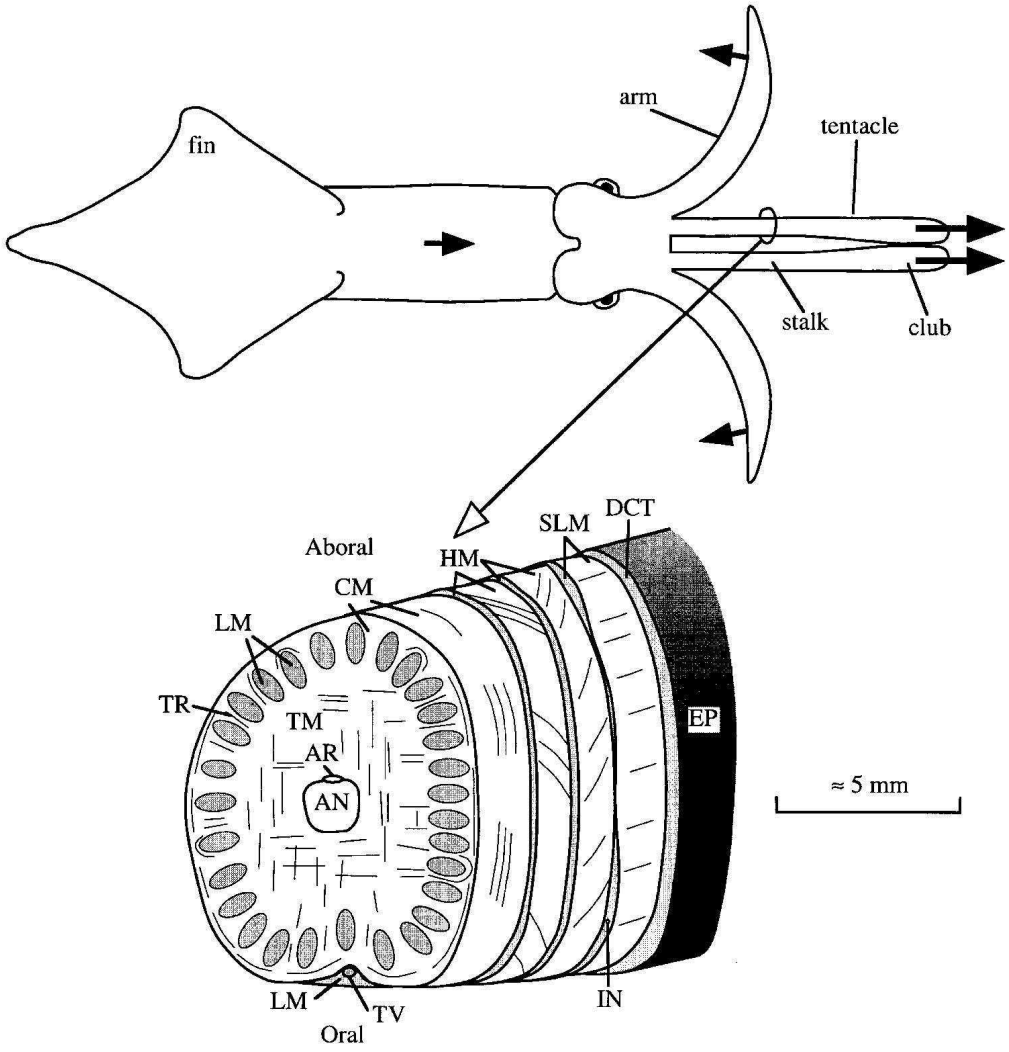

Figure 6.1: (Upper picture) Diagram of a squid. (Bottom picture) Diagram of the morphology of the tentacular stalk, pointing out its muscle groups (Van Leeuwen and Kier, 1997).

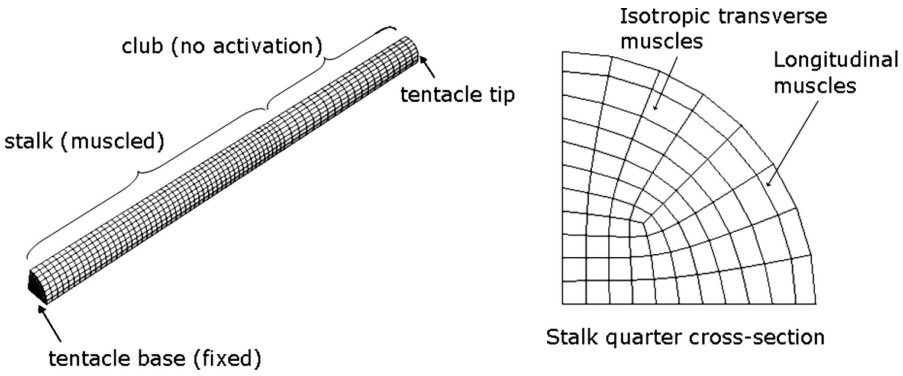

Figure 6.2: Left: Finite element mesh of the squid tentacle with distinct parts of stalk and club. Due to symmetry only a quarter is shown. The tentacle base remains fixed throughout the analysis, while all other parts are free to deform with no additional constraints imposed. Right: Cross-section of the stalk showing the muscle groups used to perform the strike (Liang *et al.*, 2006).

The functions involved in equation (6.1) are defined below. The activation function f_a takes the following form:

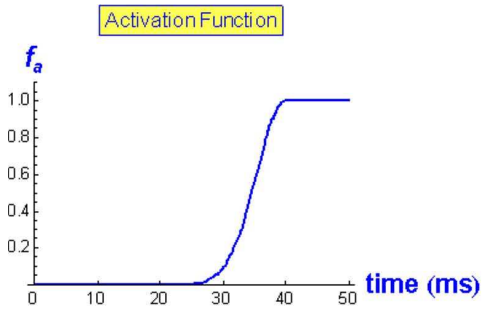

$$f_a = \begin{cases} 0 & \text{for } t \le t_d \\ \left[0.5\left(1-\cos\left(\dfrac{\pi(t-t_d)}{t_a-t_d}\right)\right)\right]^q & \text{for } t_d < t < t_d + t_a \\ 1 & \text{for } t \ge t_d + t_a \end{cases}$$

Figure 6.3: Profile of the activation function and its mathematical form for the tentacle muscle.

where t_d is the delay of a signal, t_a is the time between the start and the full activation, and the exponent q is a parameter that regulates the time profile.

The length function f_e is written as:

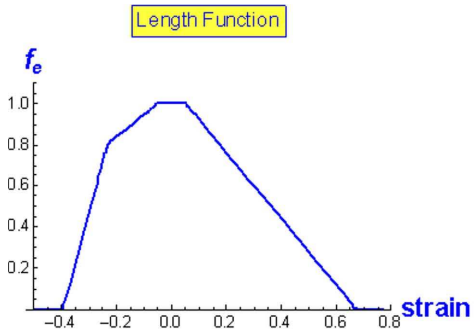

$$f_e = \begin{cases} f_5 + (f_4 - f_5)(\varepsilon_m^0 - \varepsilon_5)/(\varepsilon_4 - \varepsilon_5) & \text{for } \varepsilon_5 \le \varepsilon_m^0 < \varepsilon_4 \\ f_4 + (1 - f_4)(\varepsilon_m^0 - \varepsilon_4)/(\varepsilon_3 - \varepsilon_4) & \text{for } \varepsilon_4 \le \varepsilon_m^0 < \varepsilon_3 \\ 1 & \text{for } \varepsilon_3 \le \varepsilon_m^0 < \varepsilon_2 \\ 1 - (\varepsilon_m^0 - \varepsilon_2)/(\varepsilon_1 - \varepsilon_2) & \text{for } \varepsilon_2 \le \varepsilon_m^0 < \varepsilon_1 \end{cases}$$

Figure 6.4: Profile of the length function and its mathematical form for the tentacle muscle.

All parameters in f_e are related to the characteristics of the muscle fibers, depending on the sarcomere microstructure. The exact form of these parameters is:

$$\varepsilon_1 = \frac{\ell_{myo} - 0.5\,\ell_{bz}}{\ell_{0sarc}}, \quad \varepsilon_2 = \frac{0.5\,\ell_{bz}}{\ell_{0sarc}}, \quad \varepsilon_3 = \frac{-0.5\,\ell_{bz}}{\ell_{0sarc}},$$

$$\varepsilon_4 = \frac{\ell_{myo} - \ell_{act} - 0.5\,\ell_{bz}}{\ell_{0sarc}}, \quad \varepsilon_5 = \frac{\ell_{\min} - \ell_{0sarc}}{\ell_{0sarc}},$$

and

$$f_4 = 1 - D_{act}\frac{\ell_{act} - \ell_{myo}}{\ell_{myo} - \ell_{bz}}, \quad f_5 = 1 - D_{act}\frac{\ell_{act} + \ell_z - \ell_{\min}}{\ell_{myo} - \ell_{bz}} - (D_{myo} + C_{myo})\frac{\ell_{myo} + \ell_z - \ell_{\min}}{\ell_{myo} - \ell_{bz}},$$

where ℓ_{act} is the summed length of two opposing actin filaments in one sarcomere, ℓ_{myo} is the length of myosin filament, ℓ_{bz} is the length of the bare zone on the myosin filament, ℓ_z

is the width of the Z-disc, $\ell_{0sarc} = \ell_{act} + \ell_z + 0.5\,\ell_{bz}$ is the initial length of the sarcomere. Furthermore, D_{act} and D_{myo} are parameters to account for cross-bridge losses owing to actin overlap and interaction between myosin filament and the Z-disc. C_{myo} is introduced to account for resistive forces as a result of the collision of the myosin filaments with the Z-disc of the sarcomere. The amounts ℓ_{act}, ℓ_{myo}, $\sigma_{\max}$ and $\dot{\varepsilon}_{\min}$ vary linearly along the stalk (Table 6.1), whereas all other parameters are kept constant everywhere (Table 6.2).

The velocity function f_r is written as:

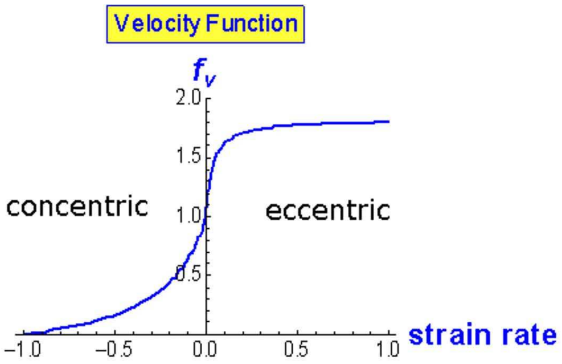

$$f_v = \begin{cases} 1.8 - 0.8\dfrac{1+\dot{\varepsilon}_m^*}{1-7.56\dot{\varepsilon}_m^*/k} & \text{for } \dot{\varepsilon}_m^* < 0 \\ \dfrac{1-\dot{\varepsilon}_m^*}{1+\dot{\varepsilon}_m^*/k} & \text{for } \dot{\varepsilon}_m^* > 0 \end{cases}$$

Figure 6.5: Profile of the velocity function and its mathematical form for the tentacle muscle.

where k is a constant and $\dot{\varepsilon}_m^* = \dot{\varepsilon}_m^0/\dot{\varepsilon}_{\min}$, with $\dot{\varepsilon}_{\min}$ the minimum (unloaded) strain rate. The first equation, which causes extension to muscle fibers, is based on stretch experiments of vertebrate muscles (Van Leeuwen and Kier, 1997) and the second equation, which causes contraction to muscle fibers, represents the well known Hill-equation (Hill, 1938).

The passive part of stress (no activation) is dependent on the strain in the material and is formulated as:

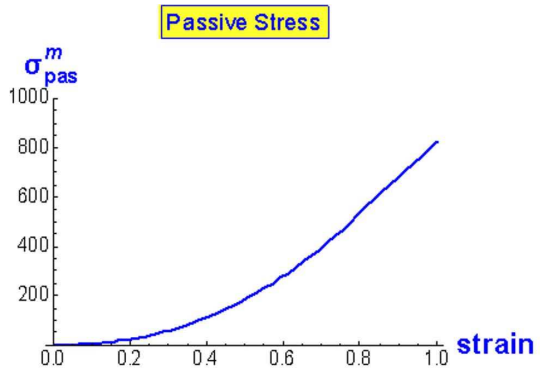

$$\sigma_{pas}^m = \begin{cases} 0 & \text{for } \varepsilon_m^0 \le 0 \\ c_1\left(\varepsilon_m^0\right)^{c_2} & \text{for } 0 < \varepsilon_m^0 < \varepsilon_c \\ c_3\varepsilon_m^0 + c_4 & \text{for } \varepsilon_m^0 \ge \varepsilon_c \end{cases}$$

Figure 6.6: Profile of the passive stress and its mathematical form for the tentacle muscle.

where $c_1 - c_4$ are constants and ε_c is a critical strain above which the relationship is linear.

Table 6.1: Values of parameters

Parameter	stalk base	stalk end
ℓ_{act} (μm)	1.21	0.73
ℓ_{myo} (μm)	0.97	0.5
$\sigma_{\max}$ (kPa)	-30	-55
$\dot{\varepsilon}_{\min}$ (s^{-1})	161	70

Table 6.2: Values of parameters

Parameter	value	Parameter	value
ε_5	-0.4	c_1 (kPa)	0.887
ℓ_{bz} (μm)	0.14	c_2	2.26
ℓ_z (μm)	0.06	c_3 (kPa)	-55
D_{act}	0.68	c_4 (kPa)	-625
D_{myo}	1.90	ε_c	0.773
C_{myo}	0.44	q	15
t_a (ms)	40	t_d (ms)	0
k	0.25	ρ (Kg/m^3)	1050

6.1.1 Results

The results show a realistic behavior of the squid tentacle during the strike to catch prey. As the two orthogonal transverse muscle groups (TM) of the stalk contract, the incompressibility of the connective tissue in the finite elements causes the extension of the tentacle in the axial direction (Fig. 6.7).

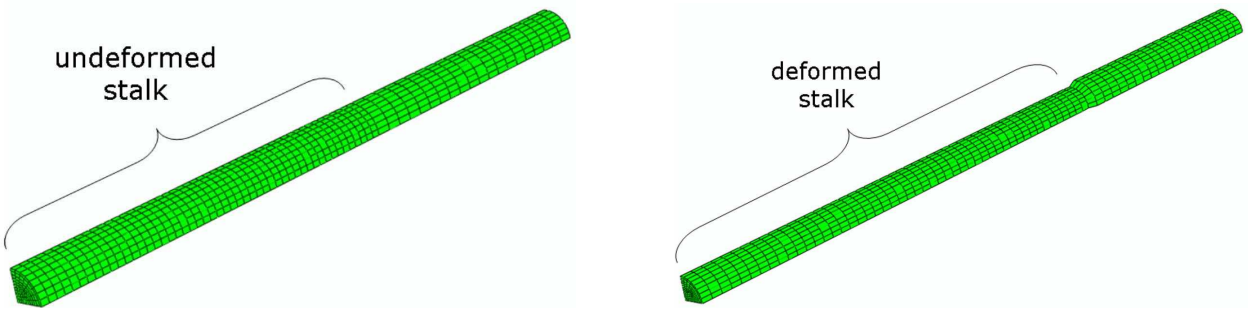

(a) (b)

Figure 6.7: (a) Undeformed configuration of the squid's finite element mesh. (b) Deformed configuration of the squid's finite element mesh.

Figures 6.8 and 6.9 show the evolution of the tentacle length and the history of the velocity at the tentacle tip during a strike. As the activation signal f_a increases, the transverse muscles

contract causing the movement of the tentacle to the axial direction. After some time, the tentacle length is so great that the passive behavior exhibited by the longitudinal muscles (LM) causes a deceleration of the strike and finally its termination.

The problem of the extension of the squid tentacle during the strike to catch prey was first studied experimentally and computationally by Van Leeuwen and Kier, 1997. Johansson *et al.*, 2000 and Liang *et al.*, 2006 developed their own models and studied the same problem. The curve profiles presented in Figs 6.8 and 6.9 agree qualitatively and quantitatively with those of previous works.

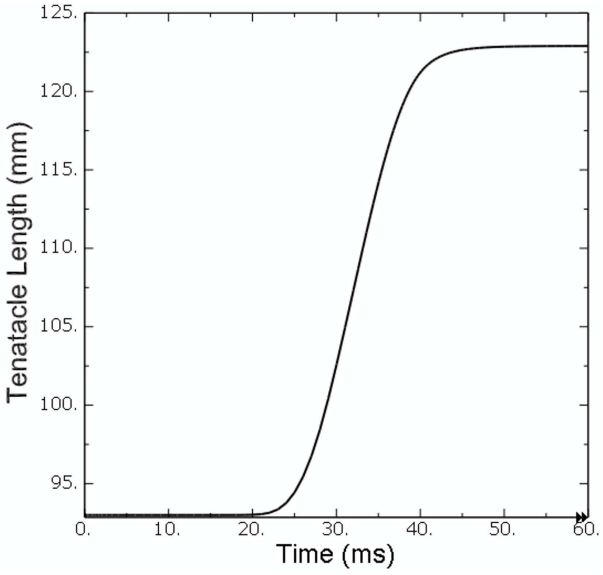

Figure 6.8: Evolution of the tentacle length.

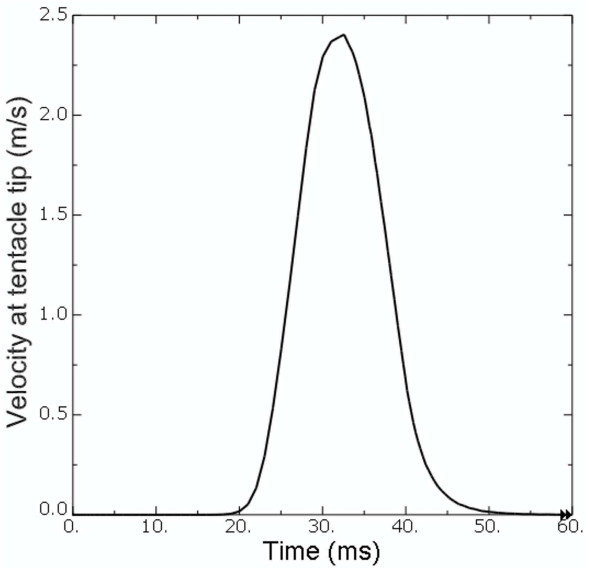

Figure 6.9: History of the velocity at the tentacle tip.

6.2 Parallel-fibered and pennated muscle

A muscle is called **parallel-fibered** when its fibers are oriented in the direction of the tendon. Examples of parallel fibered muscles in human body are the *soleus* located in the back part of the lower leg and the *biceps brachii* located on the upper arm (Fig. 6.10).

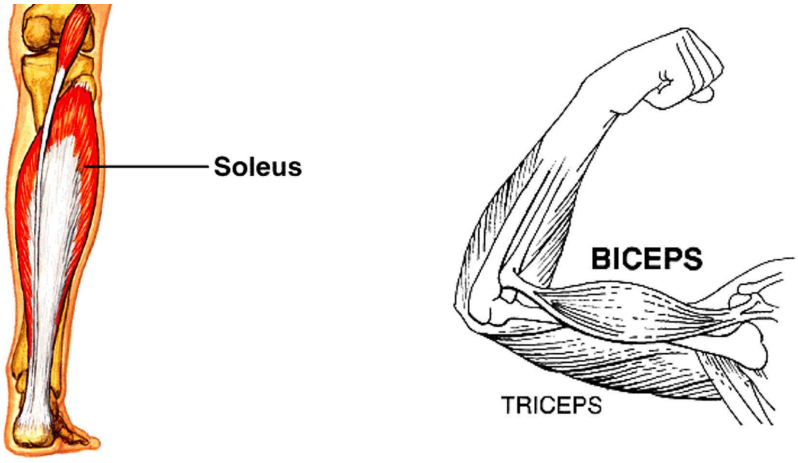

(a) (b)

Figure 6.10: Parallel fibered muscles: (a) Soleus muscle. (b) Biceps brachii muscle.

A muscle is called **pennated** when its fibers are oriented at a positive angle relative to the tendon. Examples of pennated muscles in human body are the *rectus femoris* which is one of the four quadriceps muscles on the top of the leg and the *deltoid* which is the muscle forming the rounded contour of the shoulder (Fig. 6.11).

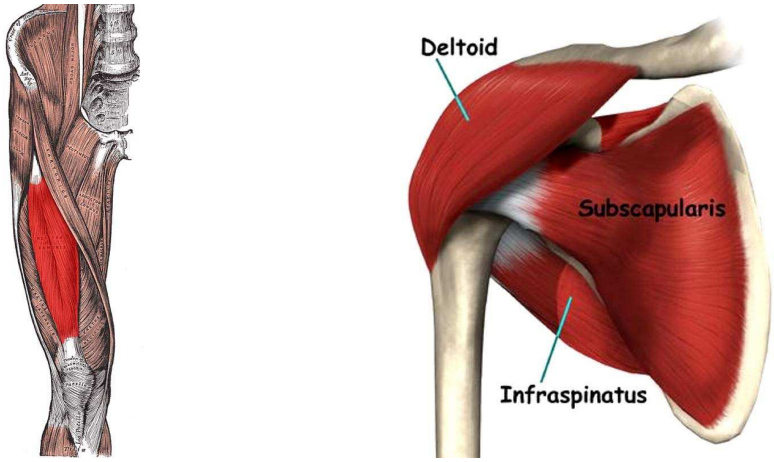

(a) (b)

Figure 6.11: Pennated muscles: (a) Rectus femoris muscle. (b) Deltoid muscle.

An attempt is made to simulate the behavior of a parallel-fibered and a pennated muscle. A simplified geometry of a muscle-tendon complex is used for both cases. The corresponding finite element meshes used in the calculations are showed in Figs 6.12 and 6.13.

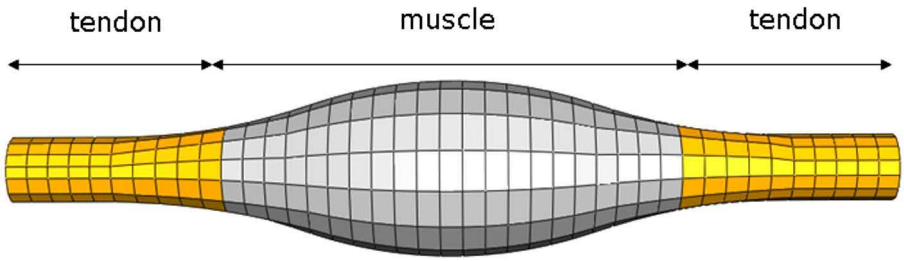

Figure 6.12: Finite element discretization of parallel-fibered muscle.

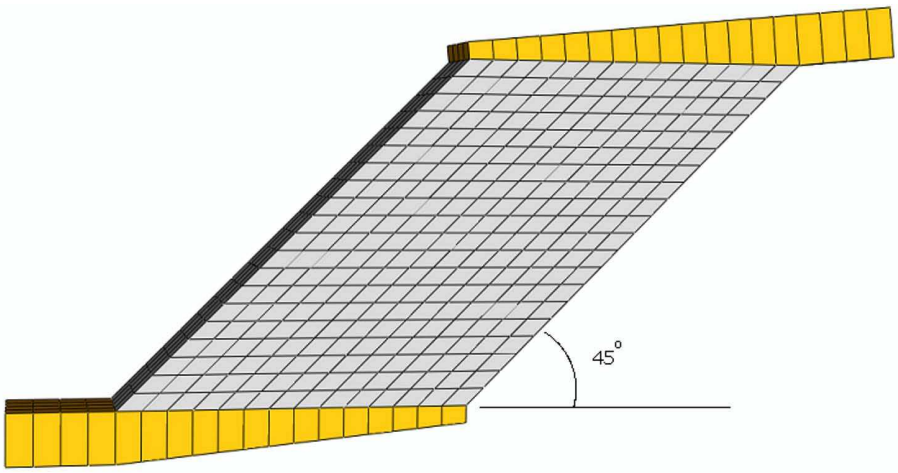

Figure 6.13: Finite element discretization of pennated muscle.

In the case of the pennated muscle the fibers are oriented at an angle 45° relative to the tendon. The fiber orientation of the parallel-fibered muscle is interpolated between the two ends of the muscle tissue as described in Appendix 6.5.

The muscle tissue is modeled as deformable with the properties described in chapter 4. The constitutive relation used for the fibers of the muscle is

$$\sigma_0^m = \sigma_{\max} \left[f_a(t)\, f_e(\varepsilon_{0a}^m\,(f_a))\, f_r(\dot{\varepsilon}_0^m) + \sigma_{pas}^m(\varepsilon_{0a}^m\,(f_a)) \right], \tag{6.2}$$

as described in section 4.1.2. A value of $\sigma_{\max} = 300$ kPa is assumed for the maximum isometric stress at optimum fiber length. The value of $\sigma_{\max}$ is a mean value of lower-extremity muscles maximum isometric stress. The maximum contraction strain rate is assumed 10 s^{-1} (Delp *et al.*, 1990). The Young's modulus E for the connective tissues is assumed to be 15 kPa (Yucesoy *et al.*, 2002) and the Poisson ratio ν is taken as 0.4999 (nearly incompressible material).

The tendons are assumed homogeneous, isotropic, and linearly elastic with Young's modulus $E = 1200$ MPa and Poisson's ratio $\nu = 0.4999$ (nearly incompressible material).

In equation (6.2), a dependence on strain, strain rate and activation state of the muscle force is described. In the following applications experimental data from Delp *et al.*, 1990,

are used.

The dependence of the active muscle force on activation-dependent strain f_e, based on experimental data for human lower-extremity muscles, has the form shown in Fig. 6.14.

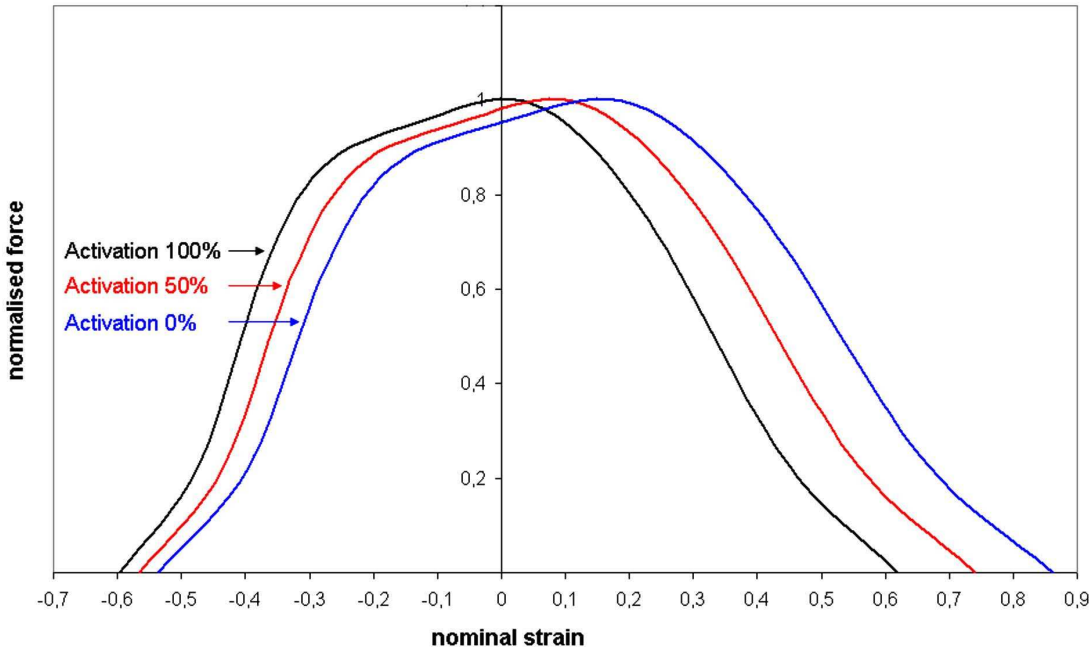

Figure 6.14: Active muscle fiber force-strain relationship. Black curve stands for 100% activation, red curve for 50% activation, and blue curve for 0% activation. It is assumed that at zero activation level the maximum muscle force is achieved at nominal strain of 0.15.

The dependence of the muscle force on strain rate, i.e., the function $f_r(\dot{\varepsilon}_0^m)$, is based on experimental data for human lower-extremity muscles and has the form shown in Fig. 6.15 below.

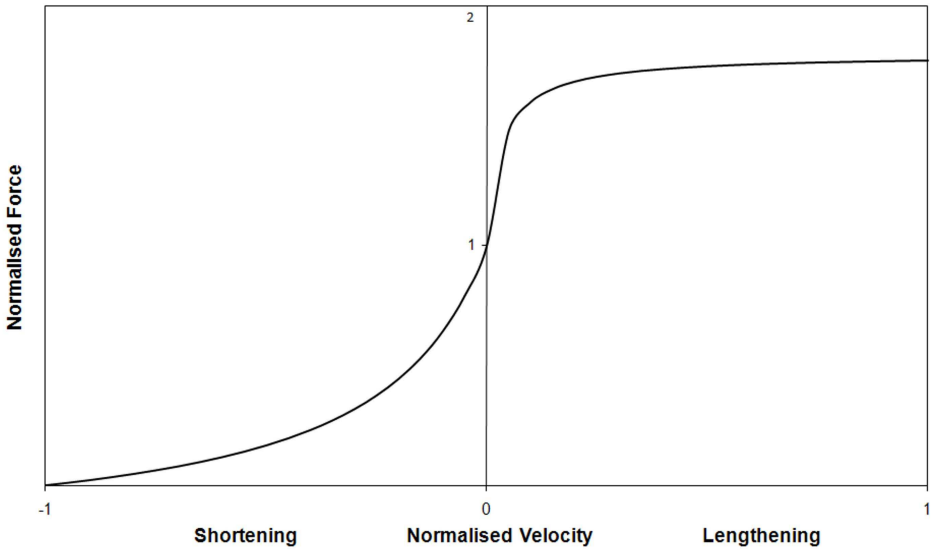

Figure 6.15: Normalised force-velocity relationship.

The activation function f_a is assumed to increase linearly up to each maximum value through the first 20 ms and then remains constant as shown in Fig. 6.16 below.

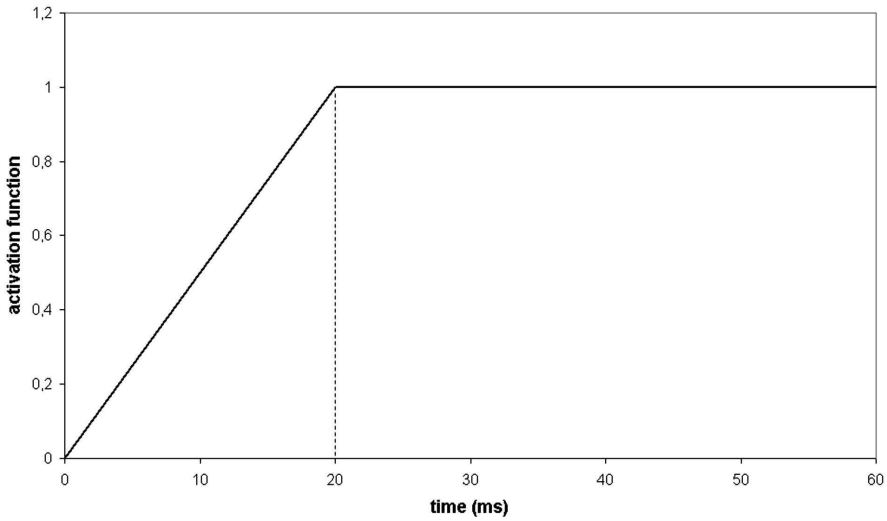

Figure 6.16: Activation function.

The dependence of the passive muscle stress on activation-dependent strain σ_{pas}^m has the form shown in Fig. 6.17 below.

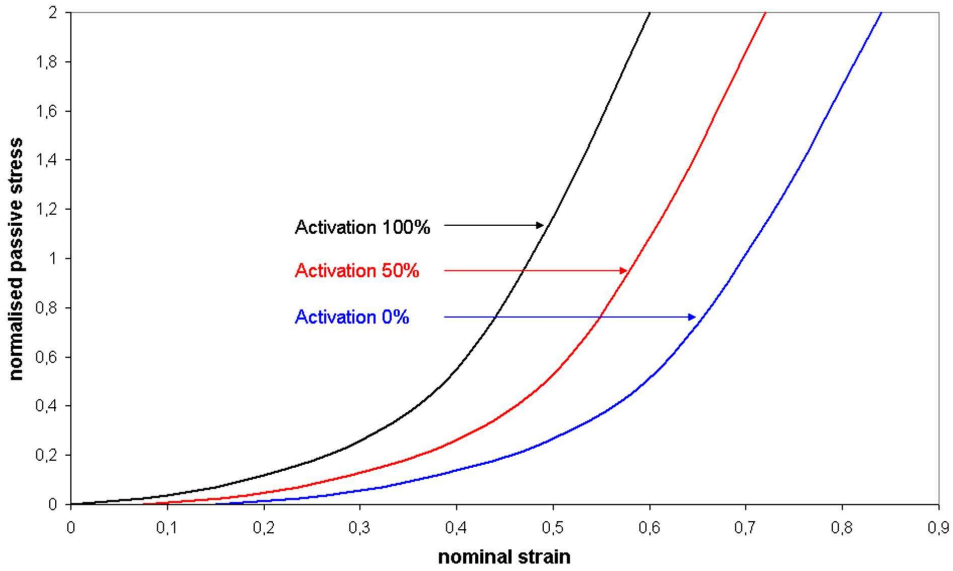

Figure 6.17: Passive muscle fiber stress-strain relationship.

6.2.1 Results

In both cases (parallel-fibered and pennated muscle) the activation shown in Fig. 6.16 is applied for 60 ms and contraction of the muscle tissue is observed. In both cases, one tendon end is kept fixed throughout the analysis (Fig. 6.18).

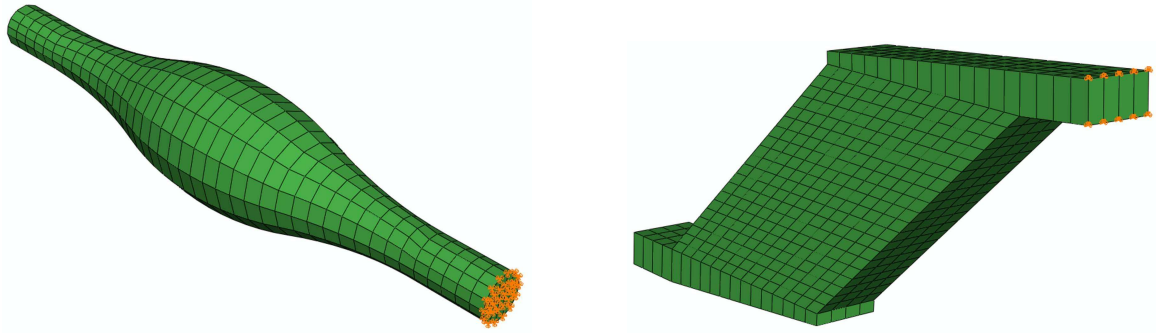

(a) (b)

Figure 6.18: Boundary conditions (fixed ends) shown in orange: (a) Parallel-fibered muscle (b) Pennated muscle.

Figure 6.19 shows the evolution of the parallel-fibered muscle.

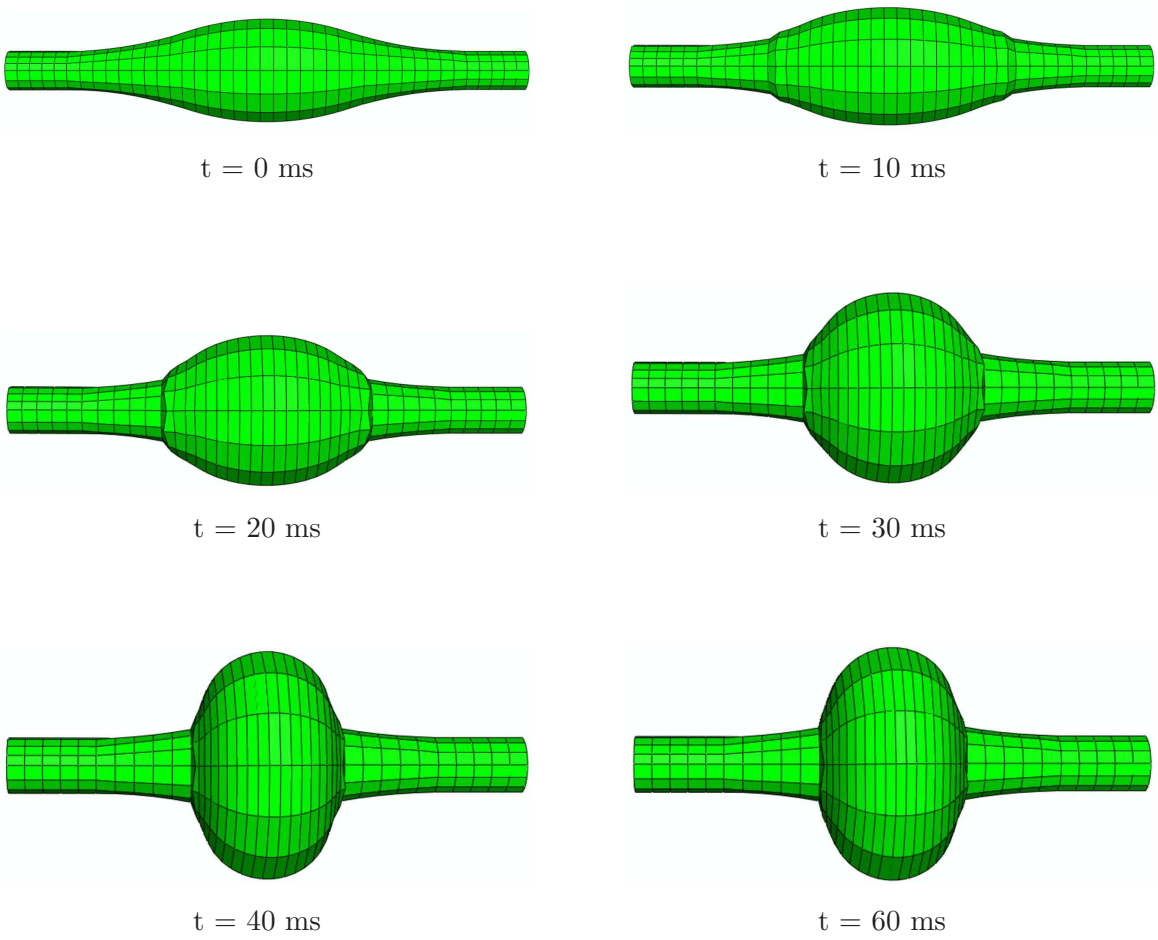

Figure 6.19: Deformed mesh of the parallel-fibered muscle.

Figure 6.20 shows the evolution of the pennated muscle.

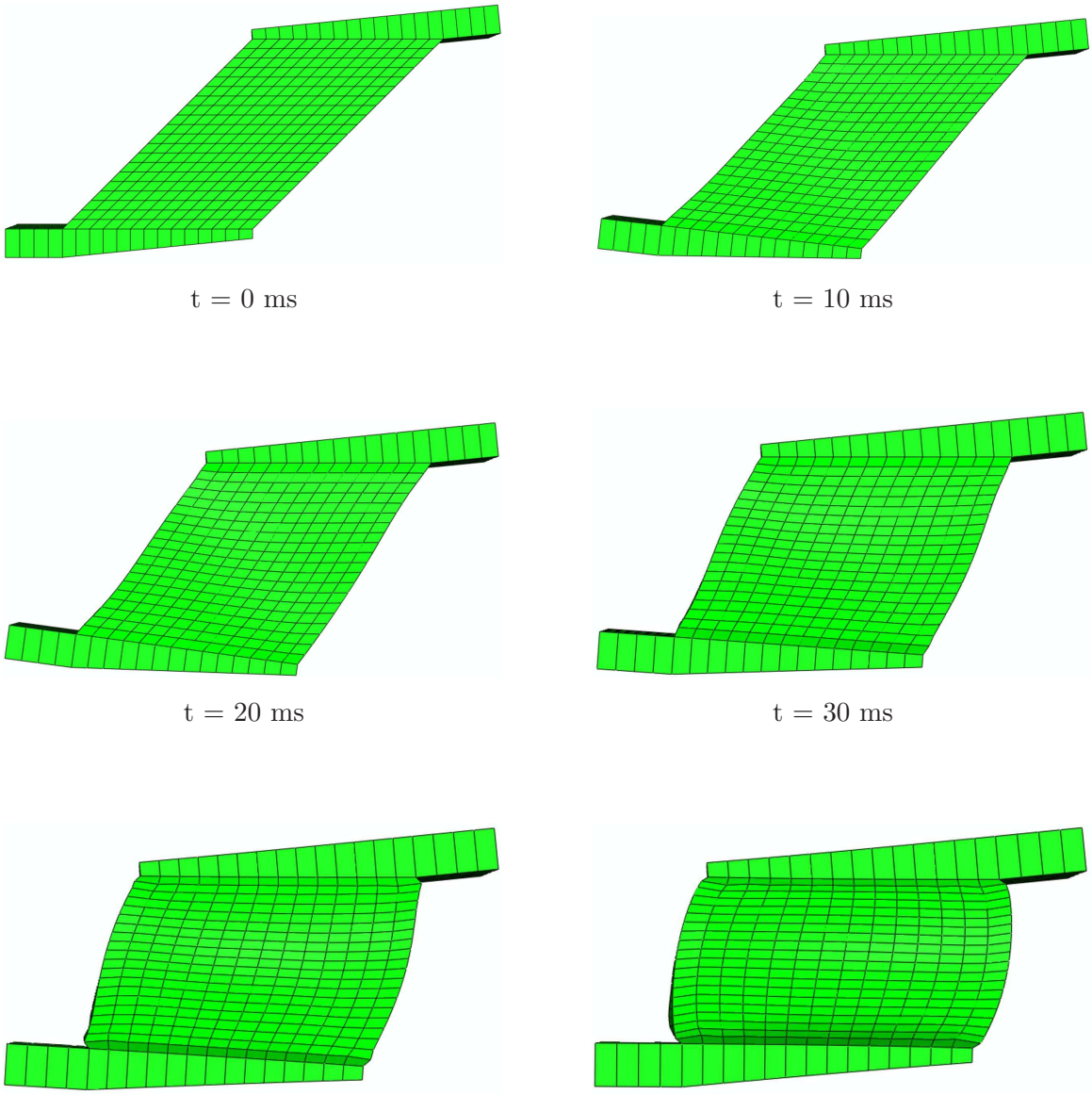

Figure 6.20: Deformed mesh of the pennated muscle.

6.3 Semitendinosus muscle

In humans, the thigh is the area between the pelvis and the knee. The semitendinosus muscle is situated at the posterior and medial aspect of the thigh. It arises from the lower and medial impression on the tuberosity of the ischium and ends a little below the middle of the thigh in a long round tendon which lies along the medial side of the popliteal fossa; it then curves around the medial condyle of the tibia and passes over the tibial collateral ligament of the knee-joint, from which it is separated by a bursa, and is inserted into the upper part of the medial surface of the body of the tibia, nearly as far forward as its anterior crest. The semitendinosus muscle helps to extend (straighten) the hip joint and flex (bend) the knee joint. It also helps to medially rotate the knee.

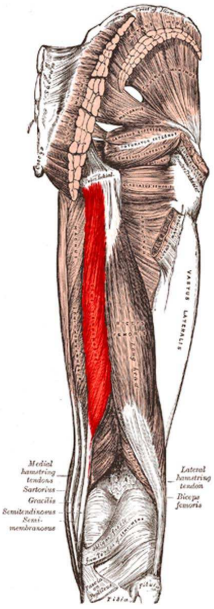

Figure 6.21: Semitendinosus muscle.

An attempt is made to simulate the behavior of the semitendinosus muscle during a contraction. Data from MRI scans are used to describe accurately the geometry of the muscle. The finite element mesh created from the MRI data is shown in Fig. 6.22. The material properties of the semitendinosus muscle tissue are the same as those used in the previous analysis of parallel-fibered and pennated muscle. The orientation of the fibers in the interior of the semitendinosus muscle is interpolated based on the surface data as described in Appendix 6.6.

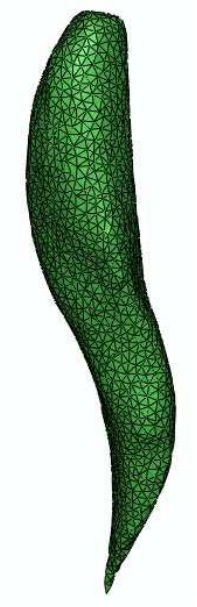

Figure 6.22: Finite element mesh of the semitendinosus muscle.

6.3.1 Results

The activation function shown in Fig. 6.16 is applied for 50 ms and contraction of the semitendinosus muscle is observed. The upper part of the muscle is kept fixed throughout the analysis as shown in Fig. 6.23.

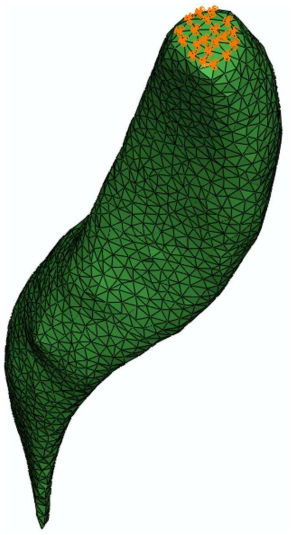

Figure 6.23: Boundary conditions in the semitendinosus muscle (fixed end) shown in orange.

Fig. 6.24 shows the various stages of the deformed semitendinosus muscle.

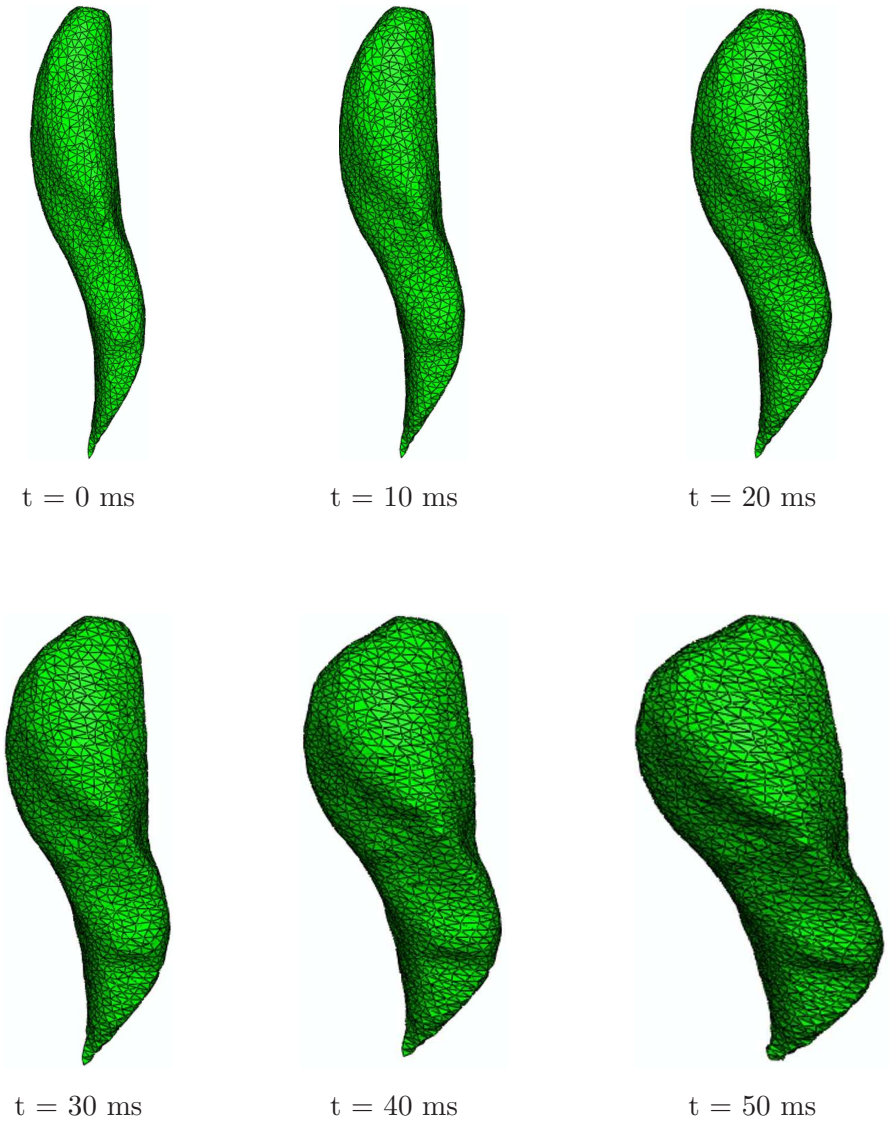

Figure 6.24: Evolution of the semitendinosus muscle.

6.4 Human leg and foot

The process of developing biomechanical finite element models (Fig. 6.25) begins with the acquisition of data that will be used to define the three-dimensional geometry of the biological tissues. These data can come from several imaging techniques, including CT (Computed Tomography) and MRI (Magnetic Resonance Imaging). Three-dimensional data sets are acquired and segmented, i.e., each tissue type of interest is labeled within the data set. The segmented data are reconstructed and three-dimensional surfaces are calculated. From the surfaces, fully volumetric meshes are generated. In the finite element analysis, the tissue types described by the finite element models are assigned specific material characteristics. The formulation is completed by prescribing the boundary conditions of the problem. Each of these steps is described in more detail below.

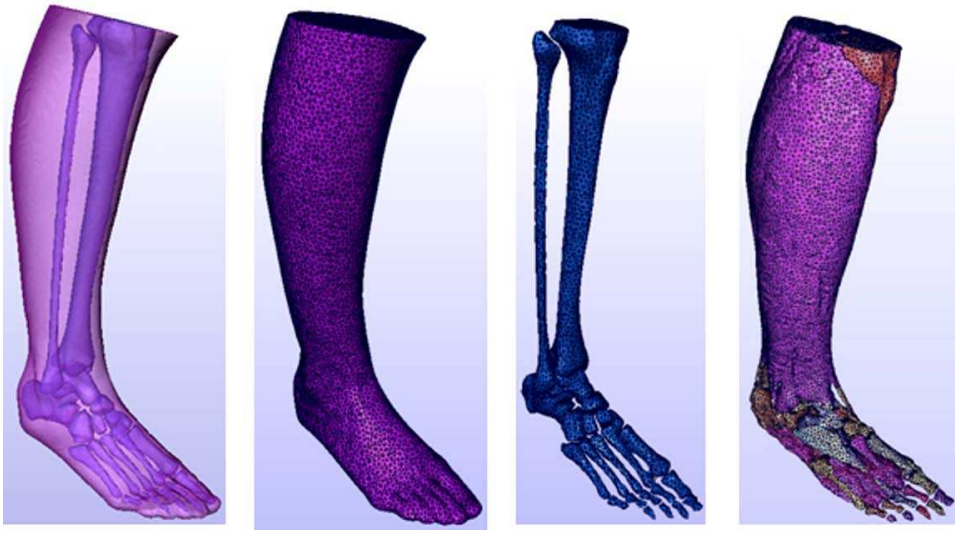

(a) (b) (c) (d)

Figure 6.25: (a) Visualization of the foot and leg structure. Finite element meshes: (b) whole structure, (c) skeleton, (d) skeleton and muscles.

6.4.1 Mesh preparation

Data scans

A basic issue for successful modeling of biological tissues is the accurate representation of their geometrical characteristics. Tissues, especially near the articular surfaces, should be defined with a high degree of spatial resolution.

In the present study, CT images with intervals of 1 mm were chosen to represent the geometry of the right foot and leg of a normal female individual of age 28 in the neutral foot position. Two characteristic CT scans of the foot and the leg are shown in Fig. 6.26

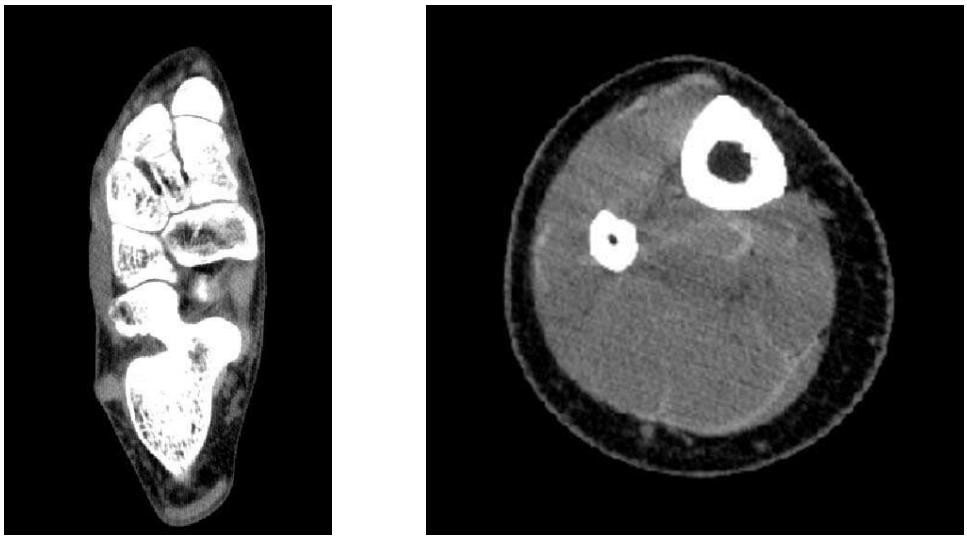

(a) (b)

Figure 6.26: (a) CT scan of the foot structure. (b) CT scan of the leg.

Segmentation

Segmentation of the images is the process of identifying tissues and their boundaries. When large data sets are used, this process is quite time consuming. However, in most cases, an automatic segmentation techniques can be used in conjunction with manual segmentation in order to minimize the time required. In the segmentation process, regardless of the technique used, it is always important to maintain a high level of accuracy of the represented geometry.

In the present study, the CT images were segmented using the AMIRA v4.1 software in order to describe the boundaries of skeleton, muscles, tendons and skin surface. Two characteristic segmented CT scans of the foot and the leg are showed in Fig. 6.27.

Surface generation and volumetric meshing

Three-dimensional surfaces are generated directly from reconstruction of the segmented images. Each surface is described by a set of triangles in a three-dimensional space. The desirable volumetric mesh results from converting the triangular to a tetrahedral mesh. A hexahedral mesh can be obtained as well from the resulted tetrahedral mesh. The volumetric mesh is created by using AMIRA v4.1. The finite element mesh used in the computations is shown in Fig. 6.25.

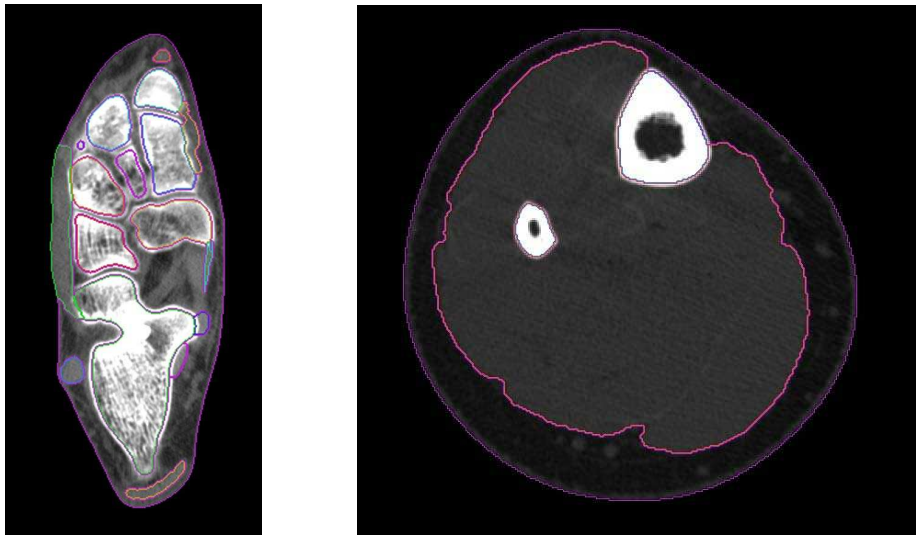

(a) (b)

Figure 6.27: (a) Segmented CT scan of the foot structure. (b) Segmented CT scan of the leg.

6.4.2 Material assignment

The next step for the development of a finite element model is to assign the appropriate material properties to the various biological tissues. The present model contains bones, ligaments, muscles, tendons, articular cartilage, and the rest soft tissues (mainly fat).

The bony structures (Fig. 6.28) are modeled as homogeneous, isotropic and linearly elastic, with Young's modulus $E = 7300$ MPa and Poisson's ratio $\nu = 0.3$ (Cheung *et al.*, 2005).

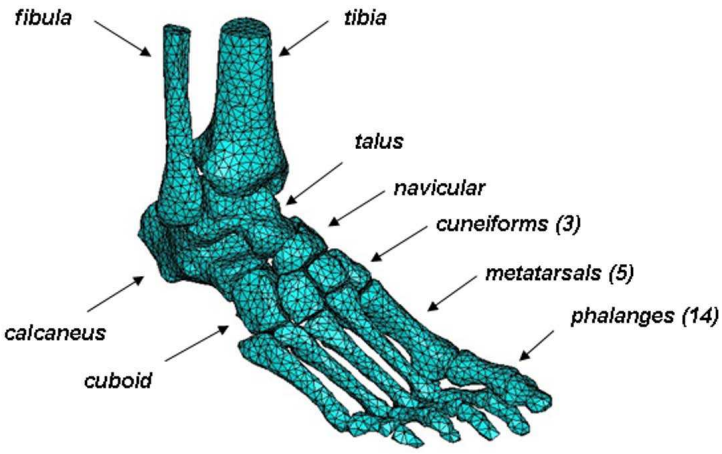

Figure 6.28: Foot bones.

The articular cartilage is taken into account by assigning appropriate material properties to the finite elements positioned at the joints. In the present model the articular cartilage (Fig. 6.29) is modeled by using the same material properties as the rest soft tissue (Fig. 6.32).

Figure 6.29: Foot cartilage between articulating surfaces shown in red.

The ligaments and plantar fascia are taken into account in the finite element model by using "tension-only" truss elements. In the present model ligaments and plantar fascia

(Fig. 6.30) are modeled as elastic truss members with Young's modulus $E = 260$ MPa and cross-sectional area $A = 18.4$ mm^2, and $E = 350$ MPa with $A = 58.6$ mm^2 respectively (Cheung *et al.*, 2005).

Figure 6.30: Foot ligaments and plantar fascia shown in red.

Muscle tissues and tendons are modeled as active and passive materials respectively. The material properties of the muscles are the same as those used in the previous applications, whereas for tendons data from Zajac, 1989 are used. In particular, the passive tendon fiber stress-strain relationship has the form shown in Fig. 6.31.

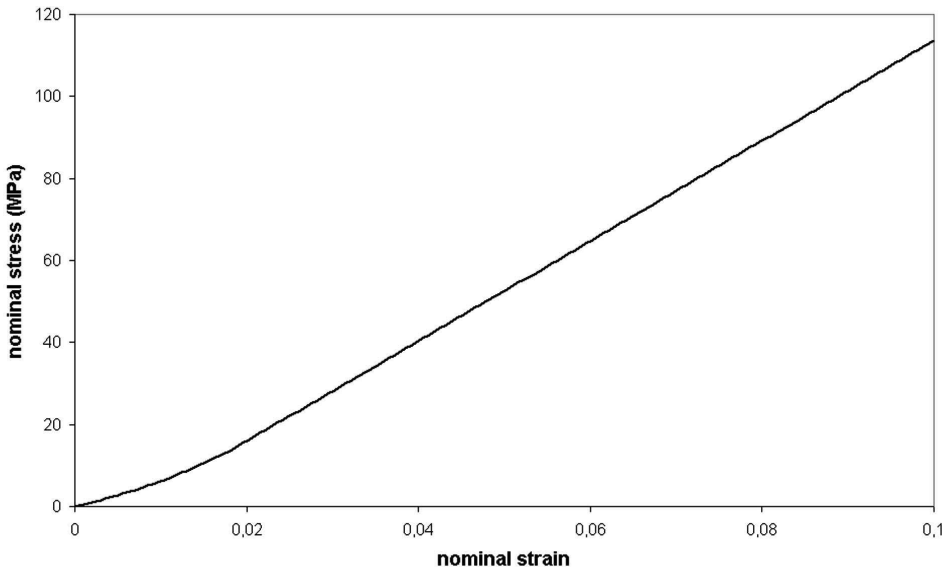

Figure 6.31: Tendon fiber stress-strain relationship.

The material data for the heel pad provided by Lemmon *et al.*, 1997 and shown in Fig. 6.32

are used to represent the rest soft tissue stiffness in the finite element model. The non-linear

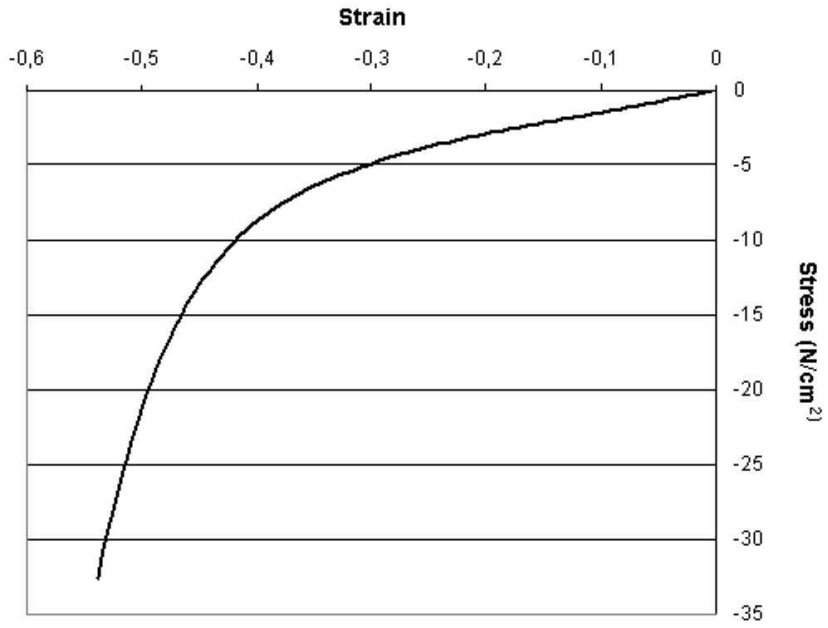

Figure 6.32: Material data for the rest soft tissues in the human leg-model.

and nearly incompressible nature of the soft tissue is represented by using a hyperelastic material model with a second-order polynomial strain energy function of the form

$$\bar{U} = \sum_{i+j=1}^{2} C_{ij} \, (\bar{I}_1 - 3)^i \, (\bar{I}_2 - 3)^j + \sum_{i=1}^{2} \frac{1}{D_i} \, (J-1)^{2\,i}, \tag{6.3}$$

where $\bar{U}$ is the elastic strain energy per unit undeformed volume, C_{ij} and D_i are material parameters, $J = \det \mathbf{F}$,

$$\bar{I}_1 = \bar{\lambda}_1^2 + \bar{\lambda}_2^2 + \bar{\lambda}_3^2, \qquad \bar{I}_2 = \frac{1}{\bar{\lambda}_1^2} + \frac{1}{\bar{\lambda}_2^2} + \frac{1}{\bar{\lambda}_3^2}, \tag{6.4}$$

λ_i are the principal stretches, and $\bar{\lambda}_i = \lambda_i / J^{1/3}$. The coefficients of the hyperelastic material model C_{ij} and D_i (Table 6.3) are calculated by ABAQUS based on the uniaxial stress-strain data of Fig. 6.32.

Table 6.3: Values of parameters C_{ij} $\left(\mathrm{N/mm^2}\right)$ and D_i $\left(\mathrm{mm^2/N}\right)$

Parameter	C_{10}	C_{01}	C_{20}	C_{11}	C_{02}	D_1	D_2
Value	0.08556	− 0.05841	0.039	− 0.02319	0.00851	3.68324	0.0

6.4.3 Finite element analysis

The purpose of the current analysis is to produce plantar flexion of the ankle by implementing and activating the muscle material model presented in Chapter 4 in the corresponding plantar flexor muscles of the developed finite element model of the foot and leg (Fig. 6.25). Plantar flexion is the motion the ankle joint makes when the toes point downward and dorsi flexion is the motion the ankle joint makes when the foot points upward. (Fig. 6.33).

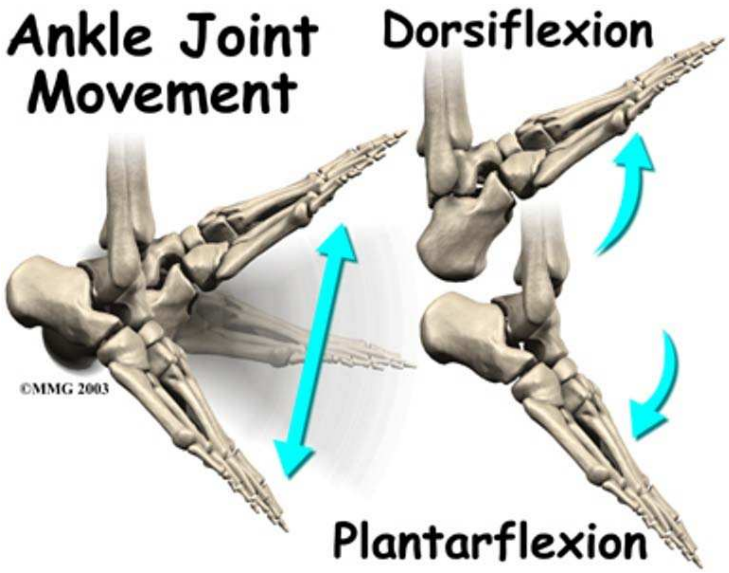

Figure 6.33: Ankle joint movement. Plantar flexion and dorsi flexion.

In the current analysis the activation function shown in Fig. 6.16 is applied to the plantar flexor muscles for 90 ms. Initially, the fiber directions of the leg muscles and Achilles tendon are assumed to be parallel with the long-axis of the tibia bone (vertical with regard to the plantar surface of the foot). The upper bound of the leg is kept fixed throughout the analysis, as shown in Fig. 6.34.

Figure 6.35 shows the deformation of the leg and foot area as predicted by the finite element solution.

Figure 6.34: Boundary conditions applied in the present case shown in orange (fixed upper bound of the leg).

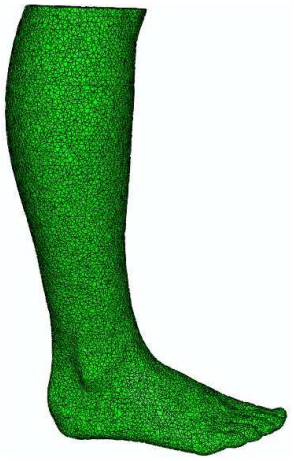

t = 0 ms

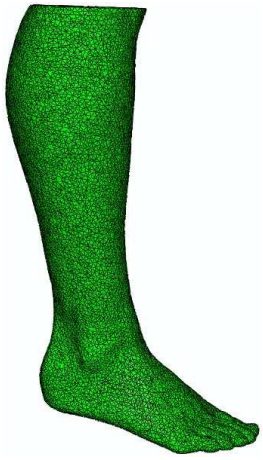

t = 20 ms

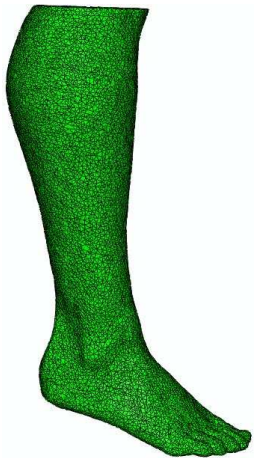

t = 40 ms

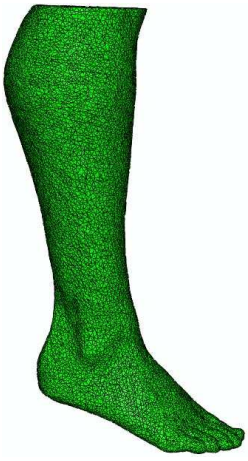

t = 60 ms

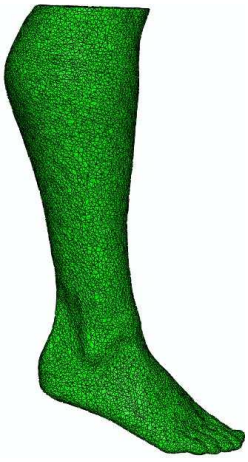

t = 90 ms

Figure 6.35: Deformation of the leg and foot area as predicted by the finite element solution.

The finite element solution provides a realistic representation of the foot movement during the plantar flexion of the ankle. The contraction of the plantar flexor muscles causes the motion of the ankle joint and the toes to point downward. To our knowledge, it is the first time in bibliography to simulate a movement of the foot based entirely on the idea of considering the muscles as "active" materials and not by applying external forces on tissues.

We examine next in some detail the stress and deformation state at the muscle region where the maximum contraction is observed (see Fig. 6.36). We define the hydrostatic stress

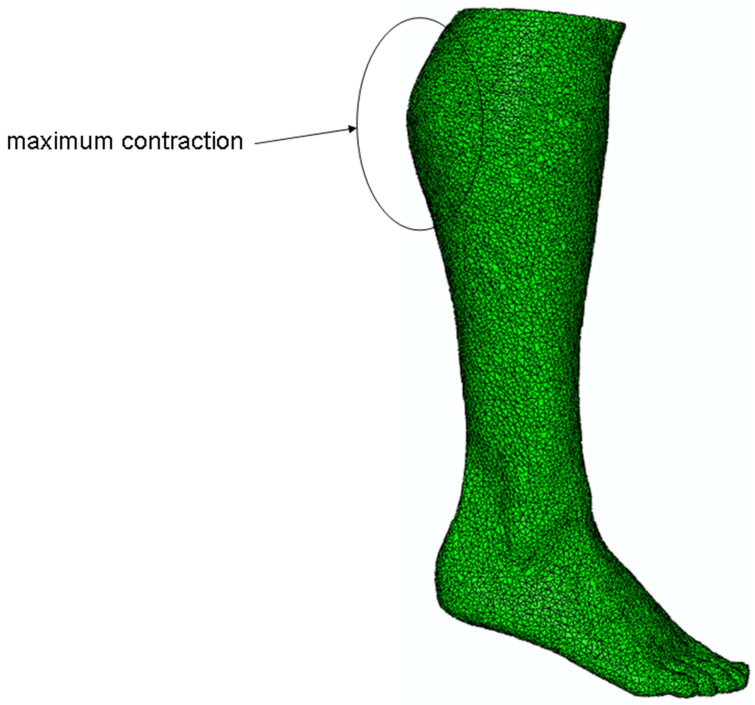

Figure 6.36: The region of the maximum muscle contraction.

p, the stress deviator $\mathbf{s}$, and the von Mises equivalent stress:

$$p = \frac{1}{3}\,\sigma_{kk}, \qquad \mathbf{s} = \boldsymbol{\sigma} - p\,\boldsymbol{\delta}, \qquad \sigma_{eq} = \sqrt{\frac{3}{2}\,\mathbf{s} : \mathbf{s}}. \tag{6.5}$$

The corresponding quantities are defined also for the stress tensor in the connective tissue $\boldsymbol{\sigma}^{ct}$. A summary of the stress state in the region of maximum contraction is shown in Table 6.4. We also determine the volumetric strain ε_v, the strain deviator $\mathbf{e}$, and the von Mises equivalent strain:

$$\varepsilon_v = \varepsilon_{kk}, \qquad \mathbf{e} = \boldsymbol{\varepsilon} - \frac{1}{3}\,\varepsilon_v\,\boldsymbol{\delta}, \qquad \varepsilon_{eq} = \sqrt{\frac{2}{3}\,\mathbf{e} : \mathbf{e}}. \tag{6.6}$$

The corresponding quantities are defined also for the strain tensor in the connective tissue $\boldsymbol{\varepsilon}^{ct}$. A summary of the strain state in the region of maximum contraction is shown in Table 6.5.

As regards to tendons, the stress placed on tendons as a result of voluntary muscle contraction has been estimated to be 30% of the maximum tensile strength (Stone and

Table 6.4: Stresses in the region of maximum contraction

Quantity	Value
p	46 kPa
σ_{eq}	40 kPa
σ^m	38 kPa
p^{ct}	34 kPa
σ_{eq}^{ct}	4.7 kPa

Table 6.5: Strains in the region of maximum contraction

Quantity	Value
ε_v	0.00135
ε_{eq}	0.677
ε_m	-0.56
ε_v^{ct}	0.00135
ε_{eq}^{ct}	0.51

Karatzaferi, 2003). A mean value of the ultimate stress in tendon is 100 MPa (Zajac, 1989). The model prediction of the maximum principal stress in achilles tendon as a result of muscle contraction is 32 MPa (Fig. 6.37) and agrees very well with the findings in the literature.

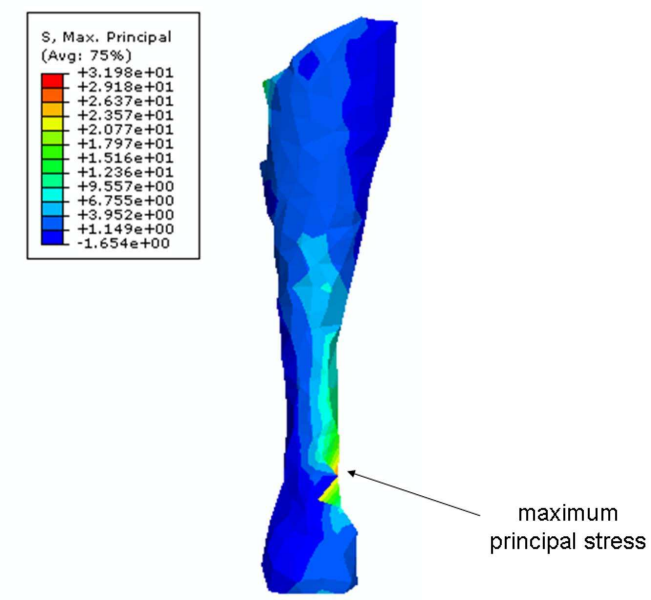

Figure 6.37: The maximum principal stress in achilles tendon as a result of muscle contraction.

6.5 Appendix I: Fiber orientation of the parallel-fibered muscle

We consider the axisymmetric model shown in Fig. 6.38 for the muscle tissue. Let x be the axis of symmetry. The muscle occupies the region $x_1 \le x \le x_2$. The distance r from the axis of symmetry is defined as $r = \sqrt{y^2 + z^2}$, (y, z) being the other two spatial coordinates.

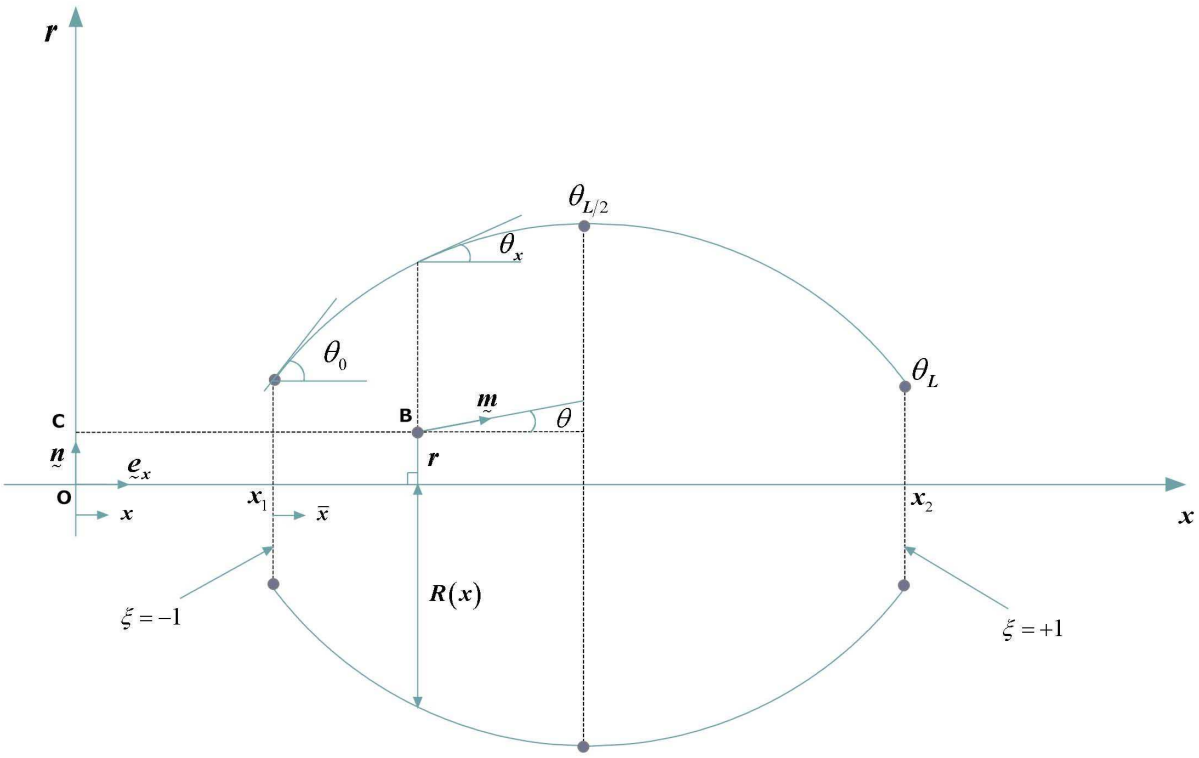

Figure 6.38: Simplified geometry of the parallel-fibered muscle.

We define the dimensionless variable

$$\xi(x) = \frac{2(x - x_1)}{x_2 - x_1} - 1, \tag{6.7}$$

and note that $\xi = -1$ at $x = x_1$, and $\xi = +1$ at $x = x_2$.

The radius R of the muscle is then defined as

$$R(x) = \sum_{i=1}^{3} N_i(\xi(x))\, R_i, \tag{6.8}$$

where

$$N_1(\xi) = \frac{1}{2}\xi(\xi - 1), \qquad N_2(\xi) = \frac{1}{2}\xi(\xi + 1), \qquad N_3(\xi) = 1 - \xi^2, \tag{6.9}$$

and (R_1, R_2, R_3) are know values of R at $x = x_1$, $x = x_2$ and $x = (x_1 + x_2)/2$ respectively.

The slope $\theta_x(x) = dR/dx$ is computed from

$$\theta_x(x) = \frac{dR}{dx} = \sum_{i=1}^{3} \frac{\partial N_i}{\partial \xi}\frac{\partial \xi}{\partial x} R_i = \frac{2}{L}\sum_{i=1}^{3} \frac{\partial N_i}{\partial \xi} R_i. \tag{6.10}$$

We consider a generic material point located at (x, y, z) as shown in Fig. 6.38. We assume that the muscle fiber at that point makes an angle θ with the $x-$axes defined by

$$\theta(x, r) = \frac{r}{R(x)}\,\theta_x(x) \qquad \text{or} \qquad \theta(x, y, z) = \frac{\sqrt{y^2 + z^2}}{R(x)}\,\theta_x(x), \tag{6.11}$$

so that $\theta = 0$ for $r = 0$, and $\theta = \theta_x$ for $r = R$.

Let $(\mathbf{e}_x, \mathbf{e}_y, \mathbf{e}_z)$ be unit vectors along the coordinate axis. Then, the unit vector $\mathbf{n}$ in the $r-$direction is given by

$$\mathbf{n} = \frac{y}{r}\,\mathbf{e}_y + \frac{z}{r}\,\mathbf{e}_z. \tag{6.12}$$

Finally, the fiber direction $\mathbf{m}$ is determined from

$$\mathbf{m} = \cos\theta\,\mathbf{e}_x + \sin\theta\,\mathbf{n} \qquad \text{or} \qquad \mathbf{m} = \cos\theta\,\mathbf{e}_x + \sin\theta\,\frac{y}{r}\,\mathbf{e}_y + \sin\theta\,\frac{z}{r}\,\mathbf{e}_z. \tag{6.13}$$

6.6 Appendix II: Fiber orientation of the semitendinosus muscle

We consider a plane that includes the vertical $z-$axis and cuts through the semitendinosus muscle. Of all such vertical planes, we choose the one on which the muscle has the maximum "width", i.e., the one on which the functions $f_1(z)$ and $f_2(z)$ that define the boundaries of the muscle on that plane are the farthest apart (see Fig. 6.39). On that plane, we define the fiber orientation at every material point as described in the following, and assume that the picture repeats itself in the direction perpendicular to the plane.

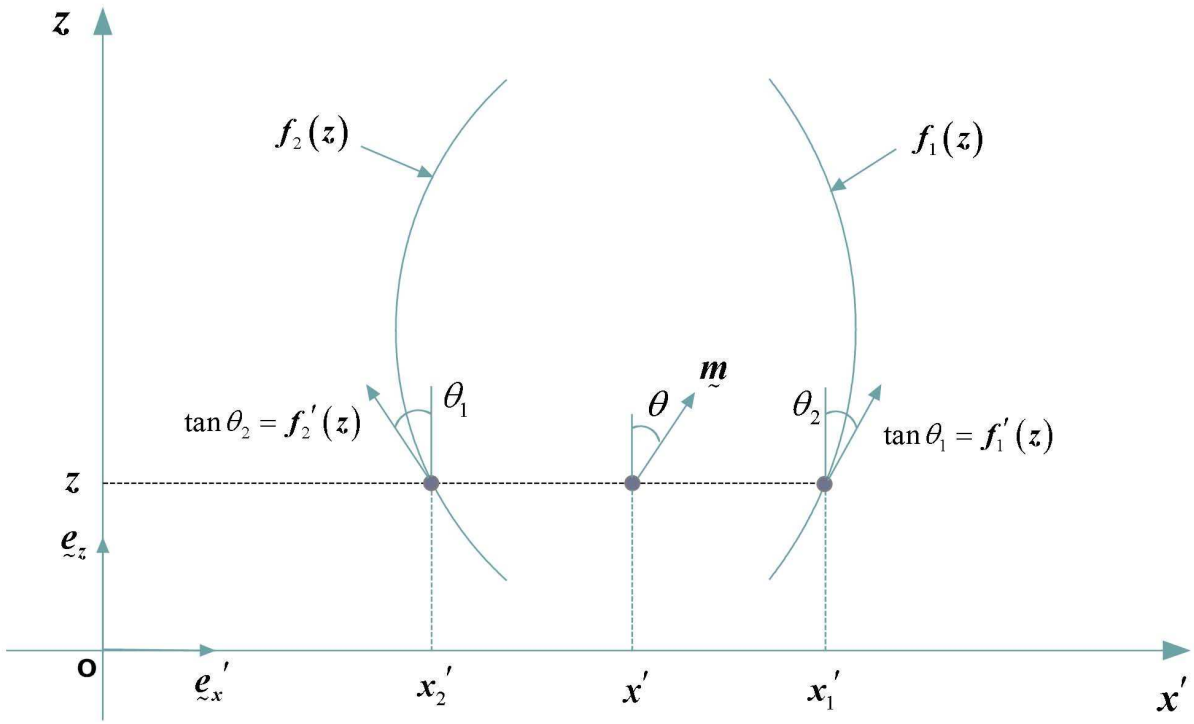

Figure 6.39: Simplified geometry of a vertical section of the semitendinosus muscle.

Let $(\mathbf{e}_x, \mathbf{e}_y, \mathbf{e}_z)$ be unit vectors along the global coordinate axis (x, y, z). On the aforementioned vertical plane, we consider an axis x' perpendicular to the $z-$axis, as shown in Fig. 6.39. Let ϕ be the angle the $x'-$ axis makes with global $x-$axis. Then the unit vector $\mathbf{e}'_x$ along the $x'-$axis is given by

$$\mathbf{e}'_x = \cos\phi\, \mathbf{e}_x + \sin\phi\, \mathbf{e}_y. \tag{6.14}$$

Let (x, y, z) be the coordinates of a material point relative to the global coordinate system. For that point, we calculate the corresponding x' coordinate:

$$x'(x, y) = x\, \cos\phi + y\, \sin\phi, \tag{6.15}$$

and, using its $z-$coordinate, identify the two "extreme" points on the muscle boundary at

$$x_1'(z) = f_1(z) \qquad \text{and} \qquad x_2'(z) = f_2(z), \tag{6.16}$$

as shown in Fig. 6.39. The slope of the muscle boundary at these points is determined from

$$\tan\theta_1(z) = \frac{df_1(z)}{dz} \qquad \text{and} \qquad \tan\theta_2(z) = \frac{df_2(z)}{dz}. \tag{6.17}$$

We introduce next the dimensionless variable

$$\xi(x', z) = \frac{x' - x_2'(z)}{x_1'(z) - x_2'(z)}, \tag{6.18}$$

and note that $\xi = 0$ at $x' = x_2'$, and $\xi = 1$ at $x' = x_1'$.

Then, we assume that the slope $\tan\theta$ of the unit vector $\boldsymbol{m}$ that defines the fiber direction at the point under consideration is defined by means of a linear interpolation between the corresponding values $\tan\theta_1$ and $\tan\theta_2$:

$$\tan\theta(x', z) = \xi(x', z)\ \tan\theta_1(z) + \big[1 - \xi(x', z)\big]\ \tan\theta_2(z). \tag{6.19}$$

Finally, the fiber direction $\boldsymbol{m}$ is

$$\boldsymbol{m} = \sin\theta\, \mathbf{e}_x' + \cos\theta\, \mathbf{e}_z \qquad \text{or} \qquad \boldsymbol{m}(x', z) = \sin\theta\ \cos\phi\, \mathbf{e}_x + \sin\theta\ \sin\phi\, \mathbf{e}_y + \cos\theta\, \mathbf{e}_z, \tag{6.20}$$

where

$$\sin\theta = \frac{\tan\theta}{\sqrt{1 + \tan^2\theta}} \qquad \text{and} \qquad \cos\theta = \frac{1}{\sqrt{1 + \tan^2\theta}}. \tag{6.21}$$

Chapter 7

Closure

In this thesis, a three dimensional constitutive model based on continuum mechanics has been developed for muscle and tendon tissues in the context of finite strains. The model accounts for all the essential information needed to describe accurately the microstructure of the biological materials. In addition, the constitutive model has been implemented in a finite element code (ABAQUS). Incorporating this kind of models in a finite element code allows us to account for the exact three dimensional geometrical characteristics of muscle and tendon structures, predict the deformed shape and the internal loadings of the tissues, as well as simulate complex biological systems in a realistic and more sophisticated manner.

The proposed constitutive model was based on the idea of a "composite" material that consists of fibers, connective tissues, and biofluids surrounding the fibers. Considering all materials as "continuous media", the constitutive model developed is a "homogenization" process that accounts for the presence of the fibers and the other material "phases". The muscle fibers, apart from their "passive" behavior, are responsible for the force production in the muscle whereas the connective tissues support the fibers and reinforce the elastic nature of the muscle tissue. The dependence of force production in the muscle on fiber's length, velocity, and activation state as well as the fiber orientation was taken into account in the developed model. On the other hand, connective tissue "follows" the fiber's contraction and thus is subjected to large deformations during a human movement. A hyperelastic material was used for the connective tissues in the current model. As regards to tendon, the behavior of the tendon fibers is only passive, so the "active" term in the constitutive model was omitted. The proposed constitutive model was described in detail in Chapter 4.

A methodology for the numerical implementation of the developed non-linear and anisotropic constitutive equations for muscle and tendon in the context of the finite element method was also developed. The implementation of a constitutive model in a finite element code involves the evaluation of the constitutive equations at the Gauss integration points of the elements and the calculation of the corresponding "linearization moduli" that are needed for the global equilibrium "Newton loop". The constitutive model was implemented in the ABAQUS general purpose finite element code; this program provides a general interface so

that a particular constitutive model can be introduced as a "user subroutine" (UMAT). The model was then used for the analysis of static and dynamic problems using the "standard-implicit" version of the code. The numerical implementation of the proposed constitutive model was described in detail in Chapter 5.

In Chapter 6 the constitutive model for muscle and tendon was applied to various cases of biological structures. Firstly, a problem that was studied experimentally and computationally in the past was chosen in order to validate our constitutive model and the computer code. That problem was the extension of a squid tentacle during the strike to catch prey. The results of our model agree qualitatively with those of previous works.

In addition, an attempt was made to simulate the behavior of a parallel-fibered and a pennated muscle. In both cases, simplified geometry of a muscle-tendon complex was used. We then proceeded to the simulation of a more realistic case, as that of the human semitendinosus muscle. In all of the above cases, the results of the finite element analysis showed a realistic representation of the muscle movement during its activity.

Finally, in Chapter 6, a methodology for obtaining geometrical accurate finite element models of biological structures was described in detail. That methodology was used to develop a finite element model of the human leg and foot including bone, cartilage, ligament, muscle, and tendon tissues. The lower-extremity model in conjunction with the constitutive model for muscle and tendon was used to simulate the plantar flexion of the ankle. The finite element solution provides a realistic representation of the foot movement during the plantar flexion of the ankle. To our knowledge, it is the first time in bibliography to simulate a movement of the foot based entirely on the idea of considering the muscles as "active" materials and not by applying external forces on tissues. The lower-extremity model developed in this thesis can be used for many studies including surgical applications, gait analysis, normal and abnormal behavior of certain biological structures, tendon and ligament ruptures, internal loadings of foot structures in various conditions, and many others.

At this point, it is important to address some directions for improvement of the proposed constitutive model. First of all, the dependence of muscle force production on fiber length and fiber velocity is based on experimental data for lower-extremity muscles published in the literature. An experimental method could be developed to obtain subject-specific measurements of these microstructural properties at cases where the prediction of a muscle or tendon internal loadings for a specific subject is to be accomplished. Also, a simplified activation function was used in our applications. Electromyography (EMG) could be used to evaluate and record the exact activation signal of each muscle during a specific movement.

Finally, a hyperelastic material was used to model the connective tissues. By using that material model we assume that the material properties are not affected by the time or the rate of loading. A viscoelastic material model can be used instead for the connective tissues.

As regards to the lower-extremity model we assumed all the fibers of the leg muscles

to be in the same direction. A more detailed modeling approach would expect to account for the exact fiber map of its muscle tissue. Also, it is assumed that all the fibers are of the same type e.g fast or slow, resulting in the same material properties for each fiber. An experimental method could be developed to evaluate the proportions of fast and slow fibers to the whole population of fibers in each muscle and in each subject.

Bibliography

[1] ABAQUS, Analysis User's Manual, Version 6.7, ABAQUS Inc., 2007.

[2] X. Aubert, Le couplage énergétique de la contraction musculaire. Thesis, Editions Arscia, Brussels, 1956.

[3] S.S. Blemker, P.M. Pinsky, S.L. Delp, A 3D model of muscle reveals the causes of nonuniform strains in the biceps brachii, *Journal of Biomechanics* **38** (2005) 657–665.

[4] M. Blix, Die lange und die spannung des muskels, *Skand. Arch. Physiol.* **5** (1894) 149–206.

[5] T.S. Buchanan, D.G. Lloyd, K. Manal, T.F. Besier, Neuromusculoskeletal Modeling: Estimation of Muscle Forces and Joint Moments and Movements From Measurements of Neural Command, *Journal of Applied Biomechanics* **20(4)** (2004) 367–395.

[6] D.L.A Camacho, W.R. Ledoux, E.S. Rohr, B.J. Sangeorzan, R.P. Ching, A three-dimensional, anatomically detailed foot model: A foundation for a finite element simulation and means of quantifying foot-bone position, *Journal of Rehabilitation Research and Development* **39(3)** (2002) 401–410.

[7] W.P. Chen, F.T. Tang, C.W. Ju, Stress distribution of the foot during mid-stance to push-off in barefoot gait: a 3-D finite element analysis, *Clinical Biomechanics* **16** (2001) 614–620.

[8] J.T.M. Cheung, M. Zhang, A.K.L. Leung, Y.B. Fan, Three-dimensional finite element analysis of the foot during standing - a material sensitivity study, *Journal of Biomechanics* **38** (2005) 1045–1054.

[9] R. Close, Dynamic properties of fast and slow skeletal muscles of the rat during development, *The Journal of Physiology* **173** (1964) 74–95.

[10] J.C. Criscione, A.S. Douglas, W.C. Hunter, Physically based strain invariant set for materials exhibiting transversely isotropic behavior, *Journal of the Mechanics and Physics of Solids* **49** (2001) 871–897.

[11] S.L. Delp, J. Peter Loan, M.G. Hoy, F.E. Zajac, E.L. Topp, J.M. Rosen, An interactive graphics-based model of the lower extremity to study orthopaedic surgical procedures, *IEEE Transactions on Biomedical Engineering* **37** (1990) 757–767.

[12] K.A. Edman, The velocity of unloaded shortening and its relation to sarcomere length and isometric force in vertebrate muscle fibres, *Journal of Physiology* **291** (1979) 143-159.

[13] E. Eisenberg, T.L. Hill, Y. Chen, A cross-bridge model of muscle contraction. Quantitative analysis. *Biophysical Journal* **29** (1980) 195–227.

[14] E. Eisenberg, T.L. Hill, Muscle contraction and free energy transduction in biological systems, *Science* **227** (1985) 999–1006.

[15] M. Epstein and W. Herzog, Theoretical models of skeletal muscle, New York, 1998.

[16] W.O. Fenn and B.S. Marsh, Muscular force at different speeds of shortening, *Journal of Physiology* **85** (1935) 277-297.

[17] A. Gefen, M. Megido-Ravid, Y. Itzchak, M. Arcan, Biomechanical analysis of the three-dimensional foot structure during gait: A basic tool for clinical applications, *Journal of Biomechanical Engineering* **122** (2000) 630–639.

[18] A.W. Gielen, C.W. Oomens, P.H. Bovendeerd, T. Arts, J.D. Janssen, A finite element approach for skeletal muscle using a distributed moment model of contraction, *Computer Methods in Biomechanics and Biomedical Engineering* **3** (2000) 231–244.

[19] A.M. Gordon, A.F. Huxley, F.J. Julian, The variation in isometric tension with sarcomere length in vertebrate muscle fibres, *Journal of Physiology* **184** (1966) 170–192.

[20] H. Granzier, M. Helmes, O. Cazorla, M. McNabb, D. Labeit, Y. Wu, R. Yamasaki, A. Redkar, M. Kellermayer, S. Labeit, K. Trombitas, Mechanical properties of titin isoforms, *Advances in Experimental Medicine and Biology* **481** (2000) 283–300.

[21] A.C. Guimaraes, W. Herzog, M. Hulliger, Y.T. Zhang, S. Day, Effects of muscle length on the EMG-force relationship of the cat soleus muscle studied using non-periodic stimulation of ventral root filaments, *Journal of Experimental Biology* **193** (1994) 49-64.

[22] H. Hatze, Myocybernetic control models of skeletal muscle: Characteristics and applications, University of South Africa, Pretoria, 1981.

[23] A.V. Hill, The heat of shortening and the dynamic constants of muscle, *Proceedings of the Royal Society of London B* **126** (1938) 136–195.

[24] R. Hill, Aspects of invariance in solid mechanics, in: C.S. Yih, Ed., *Advances in Solid Mechanics*, Vol. 18, Academic Press, New York (1978) 1–75.

[25] R. Horowits, Passive force generation and titin isoforms in mammalian skeletal muscle, *Biophysical Journal* **61** (1992) 392–398.

[26] P.A. Huijing, Important experimental factors for skeletal muscle modelling: non-linear changes of muscle length force characteristics as a function of degree of activity, *European Journal of Morphology* **34** (1996) 47–54.

[27] J.D. Humphrey, F.C.P. Yin, On constitutive relations and finite deformations of passive cardiac tissue: I. A pseudostrain-energy function, *Journal of Biomechanical Engineering* **109** (1987) 298–304.

[28] A.F. Huxley, R. Niedergerke, Structural changes in muscle during contraction. Interference microscopy of living muscle fibres, *Nature* **173** (1954) 971–973.

[29] A.F. Huxley, Muscle structure and theories of contraction, *Progress in biophysics and biophysical chemistry* **7** (1957) 255–318.

[30] A.F. Huxley, R.M. Simmons, Proposed mechanism of force generation in striated muscle, *Nature* **233** (1971) 533–538.

[31] A.F. Huxley, A note suggesting that the cross-bridge attachment during muscle contraction may take place in two stages, *Proceedings of the Royal Society of London B* **183** (1973) 83–86.

[32] A.F. Huxley, Muscular contraction, *Journal of Physiology-London* **243** (1974) 1–43.

[33] H.E. Huxley, J. Hanson, Changes in the cross-striations of muscle during contraction and stretch and their structural interpretation, *Nature* **173** (1954) 973–976.

[34] J.M. Huyghe, D.H. Van Campen, T. Arts, R.M. Heethaar, The constitutive behavior of passive heart muscle tissue: A quasi-linear viscoelastic formulation, *Journal of Biomechanics* **24** (1991) 841–848.

[35] T. Iwazumi, Molecular mechanism of muscle contraction: Another view, Cardiovascular System Dynamics (eds. J. Baan, A. Noordergraaf, J. Raines), MIT Press, Cambridge, 1978, pp. 11–21.

[36] T.R. Jenkyn, B. Koopman, P. Huijing, R.L. Lieber, K.R. Kaufman, Finite element model of intramuscular pressure during isometric contraction of skeletal muscle, *Physics Medicine and Biology* **47** (2002) 4043–4061.

[37] T. Johansson, P. Meier, R. Blickhan, A finite-element model for the mechanical analysis of skeletal muscles, *Journal of Theoretical Biology* **206** (2000) 131–149.

[38] G.E. Kempson, M.A.R Freeman, S.A.V. Swanson, Tensile properties of articular cartilage, *Nature* **220** (1968) 1127-1128.

[39] J.W. Kimball, Online Biology Textbook, http://users.rcn.com/jkimball.ma.ultranet/BiologyPages/

[40] D. Lemmon, T.Y. Shiang, A. Hashmi, J.S. Ulbrecht, P.R. Cavanagh, The effect of insoles in therapeutic footwear-a finite element approach, *Journal of Biomechanics* **30** (1997) 615–620.

[41] R. R. Lemos, M. Epstein, W. Herzog, B. Wyvill, A framework for structured modeling of skeletal muscle, *Computer Methods in Biomechanics and Biomedical Engineering* **7** (2004) 305–317.

[42] J. Li, X.J. Luo, Z.B. Kuang, A nonlinear anisotropic model for porcine aortic heart valves, *Journal of Biomechanics* **34** (2001) 1279–1289.

[43] Y. Liang, R.M. McMeeking, A.G. Evans, A finite element simulation scheme for biological muscular hydrostats, *Journal of Theoretical Biology* **242** (2006) 142–150.

[44] W. A. Linke, M. Ivemeyer, N. Olivieri, B. Kolmerer, J. C. Ruegg, S. Labeit, Towards a molecular understanding of the elasticity of titin, *Journal of Molecular Biology* **261** (1996) 62–71.

[45] R.W. Lymn, E.W. Taylor, Mechanism of adenosine triphosphate hydrolysis by actomyosin, *Biochemistry* **10** (1971) 4617–4624.

[46] E.N. Marieb, K. Hoehn, Human Anatomy & Physiology, 2007.

[47] J.A.C. Martins, E.B. Pires, R. Salvado, P.B. Dinis, A numerical model of passive and active behavior of skeletal muscles, *Computer Methods in Applied Mechanics and Engineering* **151** (1998) 419–433.

[48] M.M. Mehrabadi and S. Nemat-Nasser, Some basic kinematical relations for finite deformations of continua, *Mechanics of Materials* **6** (1987) 127–138.

[49] B.M. Nigg, W. Herzog, Biomechanics of the musculo-skeletal system, 1999.

[50] M. Nordin, V.H. Frankel, Basic biomechanics of the musculoskeletal system, 2001.

[51] C.W.J. Oomens, M. Maenhout, C.H. Van Oijen, M.R. Drost, F.P. Baaijens, Finite element modeling of contracting skeletal muscle, *Philosophical Transactions of the Royal Society B* **358** (2003) 1453–1460.

[52] E. Otten, A myocybernetic model of the jaw system of the rat, *Journal of Neuroscience Methods* **21** (1987) 287–302.

[53] E. Otten, M. Hulliger, A finite-elements approach to the study of functional architecture in skeletal muscle, *Zoology* **98** (1995) 233–242.

[54] Y. Papatriantafyllou, TRIP steels: constitutive modeling and computational issues, Ph.D. Thesis, University of Thessaly, 2005.

[55] G.H. Pollack, Muscles and molecules: Uncovering the principles of biological motion, Ebner & Sons, Seattle, WA, 1990

[56] S. Ramaswamy and N. Aravas, Finite element implementation of gradient plasticity models – Part I: Gradient-dependent yield functions, *Computer Methods in Applied Mechanics and Engineering* **163** (1998) 11–32.

[57] A.J.M. Spencer, Continuum Theory of the Mechanics of Fiber Reinforced Composites, Springer-Verlag, New York, 1984

[58] L.A. Spyrou, Stress analysis of the human foot during gait, MSc Thesis, University of Thessaly, Department of Mechanical Engineering, 2006

[59] M. H. Stone and C. Karatzaferi, Connective tissue and bone response to strength training, In Strength and Power in Sport (Encyclopaedia of Sports Medicine vol. 3), P. V. Komi (ed), Blackwell Science Inc, Ch **18**, pp 343–360, 2003.

[60] H.E.D.J. ter Keurs, T. Iwazumi, G.H. Pollack, The sarcomere length-tension relation in skeletal muscle, *Journal of General Physiology* **72** (1978) 565–592.

[61] C.P. Tsui, C.Y. Tang, C.P. Leung, K.W. Cheng, Y.F. Ng, D.H.K. Chow, C.K. Li, Active finite element analysis of skeletal muscle-tendon complex during isometric, shortening and lengthening contraction, *Bio-Medical Materials and Engineering* **14** (2004) 271–279.

[62] B.J.J.J. Van der Linden, Mechanical modeling of muscle functioning, Faculty of Mechanical Engineering, Enschede, University of Twente, 1998.

[63] J.L. Van Leeuwen, Optimum power output and structural design of sarcomeres, *Journal of theoretical biology* **149** (1991) 229–256.

[64] J.L. Van Leeuwen, W.M. Kier, Functional design of tentacles in squid: linking sarcomere ultrastructure to gross morphological dynamics, *Philosophical Transactions of the Royal Society B* **352** (1997) 551–571.

[65] W.J. Vankan, J.M. Huyghe, C.C. Van Donkelaar, M.R. Drost, J.D. Janssen, A. Huson, Mechanical blood-tissue interaction in contracting muscles: a model study, *Journal of Biomechanics* **31** (1998) 401–409.

[66] J.T. Viitasalo and P.V. Komi, Force-Time Characteristics and Fiber Composition in Human Leg Extensor Muscles, *European Journal of Applied Physiology* **40** (1978) 7–15.

[67] J.A. Weiss, B.N. Maker, S. Govindjee, Finite element implementation of incompressible, transversely isotropic hyperelasticity, *Computer Methods in Applied Mechanics and Engineering* **135** (1996) 107–128.

[68] Lijun Wu, Nonlinear finite element analysis for muskuloskeletal biomechanics of medial and lateral plantar longitudinal arch of Virtual Chinese Human after plantar ligamentous structure failures, *Clinical Biomechanics* **22** (2007) 221–229.

[69] Y. Yekutieli, R. Sagin-Zohar, R. Aharanov, Y. Engel, B. Hochner, T. Flash, Dynamic model of the octopus arm. I. Biomechanics of the octopus reaching movement, *Journal of Neurophysiology* **94** (2005) 1443–1458.

[70] C.A. Yucesoy, B.H.F.J.M. Koopman, P.A. Huijing, H.J. Grootenboer, Three-dimensional finite element modeling of skeletal muscle using a two-domain approach: linked fiber-matrix mesh model, *Journal of Biomechanics* **35** (2002) 1253–1262.

[71] F.E. Zajac, Muscle and tendon: Properties, models, scaling and application to biomechanics and motor control, *Critical Reviews in Biomedical Engineering* **17** (1989) 359–411.